

**MICROSCALE OBSERVABLES FOR HEAT AND MASS TRANSPORT
IN SUB-MICRON SCALE EVAPORATING THIN FILM**

A Dissertation

by

SANG-KWON WEE

Submitted to the Office of Graduate Studies of
Texas A&M University
in partial fulfillment of the requirements for the degree of

DOCTOR OF PHILOSOPHY

May 2004

Major Subject: Mechanical Engineering

**MICROSCALE OBSERVABLES FOR HEAT AND MASS TRANSPORT
IN SUB-MICRON SCALE EVAPORATING THIN FILM**

A Dissertation

by

SANG-KWON WEE

Submitted to Texas A&M University
in partial fulfillment of the requirements
for the degree of

DOCTOR OF PHILOSOPHY

Approved as to style and content by:

Kenneth D. Kihm
(Chair of Committee)

Sai Lau
(Member)

Ali Beskok
(Member)

James Boyd
(Member)

Dennis L. O'Neal
(Interim Head of Department)

May 2004

Major Subject: Mechanical Engineering

ABSTRACT

Microscale Observables for Heat and Mass Transport
in Sub-Micron Scale Evaporating Thin Film.

(May 2004)

Sang-Kwon Wee, B.S., Pusan National University, Korea;
M.S., Korea Advanced Institute of Science and Technology, Korea

Chair of Advisory Committee: Dr. Kenneth D. Kihm

A mathematical model is developed to describe the micro/nano-scale fluid flow and heat/mass transfer phenomena in an evaporating extended meniscus, focusing on the transition film region under nonisothermal interfacial conditions. The model incorporates thermocapillary stresses at the liquid-vapor interface, a slip boundary condition on the solid wall, polarity contributions to the working fluid field, and binary mixture evaporation. The analytical results show that the adsorbed film thickness and the thin film length decrease with increasing superheat by the thermocapillary stresses, which influences detrimentally the evaporation process by degrading the wettability of the evaporating liquid film. In contrast, the slip effect and the binary mixture enhance the stability of thin film evaporation. The slip effect at the wall makes the liquid in the transition region flow with smaller flow resistance and thus the length of the transition region increases. In addition, the total evaporative heat flow rate increases due to the slip boundary condition. The mixture of pentane and decane increases the length of the thin film by counteracting the thermocapillary stress, which enhances the stability of the thin film evaporation. The polarity effect of water significantly elongates the thin film length

due to the strong adhesion force of intermolecular interaction. The strong interaction force restrains the liquid from evaporation for a polar liquid compared to a non-polar liquid.

In the experimental part, laser induced fluorescence (LIF) thermometry has been used to measure the microscale temperature field of a heated capillary tube with a 1 mm by 1 mm square cross section. For the temperature measurement, the calibration curve between the temperature and the fluorescent intensity ratio of Rhodamine-B and Rhodamine-110 has been successfully obtained. The fluorescent intensity ratio provides microscale spatial resolution and good temperature dependency without any possible bias error caused by illuminating light and background noise usually encountered in conventional LIF techniques. For the validation of the calibration curve obtained, thermally stratified fields established inside a glass cuvette of 10 mm width were measured. The measurement result showed a good agreement with the linear prediction. The temperature measurement in a 1 mm capillary tube could provide the feasible method of temperature measurement for the thin film region in the future.

DEDICATION

To Kumsook, Wooju and Younju

ACKNOWLEDGMENTS

I would like to express my special appreciation to Dr. Kenneth D. Kihm for his support, guidance and encouragement to complete my research successfully. Special thanks also go to Dr. Sai Lau, Dr. Ali Beskok and Dr. James Boyd for their time and efforts assisting me in the completion of my research. I would like to acknowledge the financial support of the Microgravity Research Center of NASA Glenn.

My sincere gratitude is extended to Dr. Peter Wayner at the Rensselaer Polytechnic Institute for his kind comment and valuable material for my research and to Dr. Kevin Hallinan at the University of Dayton for the discussion about slip and polarity effect.

I also wish to thank all my colleagues in the Microscale Fluidics and Heat Transport Laboratory for their friendship during my graduate study.

Finally, I would like to give my deepest thanks to my wife, son and daughter for their love and encouragement during this endeavor. I could not have done this research without the sacrifice and support of my wife. I hope to dedicate this small accomplishment to my parents.

TABLE OF CONTENTS

	Page
ABSTRACT	iii
DEDICATION	v
ACKNOWLEDGMENTS.....	vi
TABLE OF CONTENTS	vii
LIST OF FIGURES.....	x
LIST OF TABLES	xiv
NOMENCLATURE.....	xv
 CHAPTER	
I INTRODUCTION.....	1
1.1 Problem Statement	1
1.2 Engineering Applications of Phase Change Heat Transport.....	3
1.3 Literature Review.....	10
1.3.1 Evaporating Extended Meniscus.....	10
1.3.2 Laser Induced Fluorescence Thermometry.....	16
1.4 Summary of Research Objectives	18
1.4.1 Numerical Analysis.....	18
1.4.2 Experimental Investigation	19
II BACKGROUND.....	21
2.1 Evaporating Extended Meniscus.....	21
2.2 Physics of Interfacial Phenomena	24
2.2.1 Surface Tension	24
2.2.2 Wettability.....	25
2.2.3 Disjoining Pressure	29
2.2.4 Vapor Recoil	30
2.3 Thermocapillary Effects.....	31
III NUMERICAL ANALYSIS	34
3.1 Mathematical Formulation	34

CHAPTER	Page
3.1.1 Interfacial Normal Stress Balance	35
3.1.2 Fluid Mechanics: Momentum Equation.....	40
3.1.3 Evaporative Mass Transfer	41
3.1.4 Thermal Field and Heat Transfer: Energy Equation.....	43
3.1.5 Mass Conservation in the Transition Film Region	44
3.1.6 Nondimensionalization	46
3.2 Effect of Thermocapillary Stress	50
3.2.1 Background	50
3.2.2 Review of Previous Studies	51
3.2.3 Results and Discussion	53
3.3 Effect of Slip Boundary Condition at Wall.....	69
3.3.1 Background	69
3.3.2 Mathematical Model of Slip Boundary Condition.....	72
3.3.3 Results and Discussion	73
3.4 Binary Mixture Evaporation	82
3.4.1 Background	82
3.4.2 Review of Previous Studies	84
3.4.3 Mathematical Model of Binary Mixture Evaporation.....	88
3.4.4 Results and Discussion	93
3.5 Polarity Effect of Working Fluid	101
3.5.1 Background	101
3.5.2 Mathematical Model of Polarity Effect	103
3.5.3 Results and Discussion	110
IV EXPERIMENTS	115
4.1 Introduction	115
4.2 Principle of LIF Technique	117
4.2.1 Fundamentals of Fluorescence.....	117
4.2.2 Spectral Characteristics of Rh-B and Rh-110	121
4.3 Calibration Experiment	122
4.3.1 Experimental Setup	122
4.3.2 Calibration Results	129
4.3.3 Temperature Measurement of Thermally Stratified Fields.....	135
4.4 Temperature Measurement of a Heated Glass Channel.....	138
4.4.1 Test Cell	138
4.4.2 Results and Discussion	140
V SUMMARY AND CONCLUSIONS	147
5.1 Summary	147
5.2 Conclusions	148

	Page
5.3 Recommendations	150
REFERENCES	153
VITA	160

LIST OF FIGURES

FIGURE	Page
1.1 Schematic of conventional heat pipe	4
1.2 Schematic of capillary pumped loop	5
1.3 Idealized porous wick structure with a bundle of microscopic capillary pores and an idealized capillary pore with heating.....	7
1.4 Nucleate boiling heat transport: single bubble model	9
2.1 Idealized model of extended meniscus within a capillary pore: adsorbed film, thin film (transition film), bulk meniscus region	23
2.2 Balance of interfacial tensions on a contact line.....	26
2.3 Schematic for explanation of thermocapillary stress.....	32
3.1 Two-dimensional channel geometry and transition region.....	36
3.2 Schematic for describing mass conservation within evaporating thin film	45
3.3 Film thickness profiles for different superheat conditions	57
3.4 Magnified view of film thickness profile at near adsorbed region for different superheat conditions.....	58
3.5 Distribution of curvature for different superheat conditions	59
3.6 Distribution of liquid pressure gradient for different superheat conditions	60
3.7 Distribution of evaporative mass flux for different superheat conditions	61
3.8 Distribution of interfacial temperature for different superheat conditions.....	62
3.9 Distribution of disjoining pressure and capillary pressure for different superheat conditions	63
3.10 Distribution of liquid pressure for different superheat conditions.....	64
3.11 Comparison of thin film profiles with thermocapillary effect and without thermocapillary effect for ammonia at vapor temperature of 300 K	66

FIGURE	Page
3.12 Comparison of evaporative mass flux with thermocapillary effect and without thermocapillary effect for ammonia at vapor temperature of 300 K..	67
3.13 Total evaporative heat flow rate per unit depth for both with thermocapillary effect and without thermocapillary effect at different superheat levels for ammonia	68
3.14 Comparison of meniscus profiles for thermocapillary effect and slip condition for pentane at vapor temperature of 300 K ($\Delta T=0.01K$)	75
3.15 Comparison of evaporative mass fluxes for both slip and no-slip wall conditions at different superheat levels for pentane at vapor temperature of 300K ($\Delta T=0.006K$ and $\Delta T=0.01K$).....	76
3.16 Total evaporative heat flow rate per unit depth for both slip and no-slip wall conditions at different superheat levels for pentane and ammonia.....	77
3.17 Liquid pressure gradient distribution along axial position at different superheat levels for pentane at vapor temperature 300 K ($\Delta T=0.006K$ and $\Delta T=0.01K$).....	79
3.18 Liquid pressure distribution along axial position at different superheat levels for pentane at vapor temperature of 300 K ($\Delta T=0.006K$ and $\Delta T=0.01K$).....	80
3.19 Distribution of concentration rate of pentane under different superheat conditions.....	95
3.20 Distribution of interfacial surface tension under different superheat conditions.....	96
3.21 Comparison of meniscus profiles between pure pentane (100%), mixture of pentane (98%) and decane (2%), and mixture of pentane (90%) and decane (10%) under the superheat of 0.3 K.....	97
3.22 Comparison of interfacial temperature distribution between pure pentane (100%), mixture of pentane (98%) and decane (2%), and mixture of pentane (90%) and decane (10%) under the superheat of 0.3 K.....	98
3.23 Comparison of surface tensions between pure pentane (100%), mixture of pentane (98%) and decane (2%), and mixture of pentane (90%) and decane (10%) under the superheat of 0.3 K.....	99

FIGURE	Page
3.24 Schematic of liquid-vapor interface forming within a cylindrical capillary pore with uniform wall temperature	104
3.25 Comparison of the thin film profiles of non-polar water and polar water for the same superheat condition of $\Delta T = 0.1$ K	112
3.26 Comparison of the disjoining pressure of non-polar water and polar water for the same superheat condition of $\Delta T = 0.1$ K.....	113
3.27 Comparison of the evaporative mass flux of non-polar water and polar water for the same superheat condition of $\Delta T = 0.1$ K.....	114
4.1 Jablonski diagram describing excitation and emission of a photon	119
4.2 Absorption and emission spectra of Rhodamine-110 and Rhodamine-B.....	123
4.3 Schematic layout of the experimental set up of calibration for ratiometric LIF technique.....	125
4.4 Incident laser light (488 nm) and optical filtering using bandpass filter for emission light of Rh-110 and longpass filter for emission light of Rh-B.....	127
4.5 Schematic of the test channel of a glass cuvette hold between copper blocks connected to copper pipes.....	128
4.6 Temperature dependency of fluorescence images of Rh-B (column a), Rh-110 (column b) and the ratiometric images (column c).....	130
4.7 Variation of the fluorescence intensities for Rh-B and Rh-110 against temperature ranging from 14 °C to 40 °C	132
4.8 Variation of the fluorescence intensity ratios for Rh-B and Rh-110 against temperature ranging from 14 °C to 40 °C	133
4.9 Temperature contours of thermally stratified fields for 10 mm channel	136
4.10 Comparison of measured results and linear predictions of thermally stratified fields for 10 mm channel.....	137
4.11 Schematic of test section of capillary tube and the cross sectional view of the glass channel	139

FIGURE	Page
4.12 Raw images of (a) Rh-B and (b) Rh-110 for thermal condition case 1	141
4.13 Temperature profiles for different thermal conditions: (a) $Ra = 277.2$, (b) $Ra = 352.8$, (c) $Ra = 403.2$	142
4.14 Temperature distribution along centerline of the glass channel	145

LIST OF TABLES

TABLE	Page
3.1 Physical properties of water, pentane, decane and ammonia (NIST, 2003)	54
4.1 Spectral characteristics of Rh-B and Rh-110 (Solvent: de-ionized water, T=20°C) (Sakakibara and Adrian, 1999).....	122
4.2 Spatial resolution dependency of calibration curve uncertainty	134
4.3 Three thermal conditions for the experiment of heated capillary tube.....	140

NOMENCLATURE

A	dispersion constant, J
$6\pi A$	Hamaker constant, J
A_1, B_1, C_1	constants defined in Eq. (3.36)
A_i, B_i, C_i	coefficients for Antoine Equation (3.67)
a, b	coefficient for evaporative mass flux defined in Eq. (3.100)
C	evaporation coefficient in Eq. (3.14)
$C_1 - C_7$	constants defined in Eq. (3.90)-(3.98)
$[c]$	concentration of fluorescence
c_o	speed of light, m/s
c_1	concentration of pentane in binary mixture
Ca	Capillary number
E_{EX}	energy of a photon of excitation light, J
E_{EM}	energy of a photon of emission light, J
F	fluorescent intensity
F_1, F_2, F_3, F_4	coefficients in Eqs. (3.75) - (3.78)
G	ground energy level in Fig. 4.1
g	gravitational acceleration
h	thin film thickness, m
\bar{h}	Planck's constant, J·sec

h_{fg}	latent heat of vaporization, J/kg
I_0	illuminating light intensity
k	thermal conductivity, W/(m·K)
K	curvature of liquid-vapor interface, 1/m
L_s	slip length, m
L_{s0}	asymptotic limiting value of slip length, m
\dot{m}_{evp}	evaporative mass flux, kg/(m·sec)
M	molecular weight, kg/kmol
P	pressure, Pa
q''_{evp}	evaporative heat flux, W/m ²
Q	total heat transfer rate, W
\bar{Q}	quantum efficiency
r	radial coordinate normal to substrate, m
R_o	pore radius, m
R	universal gas constant, J/(kg·K)
Ra	Rayleigh number
R_g	gas constant, J/(kg·K)
S_1, S_2	energy level in Fig. 4.1
T	temperature, K
u	velocity component in x-direction, m/s
u^*	characteristic axial velocity, m/s

V_l	molar volume, m^3/mol
x	axial coordinate parallel to substrate, m
y	vertical coordinate normal to substrate, m

Greek Symbols

α, β	coefficients for disjoining pressure in Eq. (3.84)
α_1, β_1	coefficients for slip velocity in Eq. (3.42)
α_t	thermal diffusivity
β_t	thermal expansion coefficient
Γ	mass flow rate, kg/s
γ	slope of surface tension, $\text{N}/(\text{m}\cdot\text{K})$
$\dot{\gamma}$	shear rate, $1/\text{s}$
$\dot{\gamma}_c$	critical value of shear rate, $1/\text{s}$
ε	molar absorptivity of fluorescent dye, m^2/kg
η	non-dimensional coordinate normal to solid wall
θ	non-dimensional temperature
θ_c	contact angle
κ	constant in Eq. (3.30)
λ_{EX}	wavelength of excitation light, nm
λ_{EM}	wavelength of emission light, nm
μ	dynamic viscosity, $\text{N}\cdot\text{s}/\text{m}^2$

ν	kinematic viscosity, m^2/s
ν_{EX}	frequency of excitation light, 1/sec
ν_{EM}	frequency of emission light, 1/sec
ξ	non-dimensional coordinate along solid wall
Π	disjoining pressure, Pa
ρ	density, kg/m^3
σ	surface tension, N/m
τ	shear stress, N/m^2

Subscripts

0	adsorbed film region
c	critical value
i	liquid-vapor interface
l	liquid phase
lv	liquid-vapor interface
sv	solid-vapor interface
sl	solid-liquid interface
TC	thermocapillarity
tr	transition
v	vapor phase
w	wall

CHAPTER I

INTRODUCTION

1.1 Problem Statement

Recently an advanced technology of micro-fabrication has made extraordinary miniaturization of microelectronic devices, which has introduced high heat dissipation per unit area. The conventional cooling techniques by natural or forced convection of single-phase are not enough to satisfy such a requirement of high heat flux dissipation, which has resulted in an increasing interest in change-of-phase heat transport. Phase-change process has been recognized as an efficient cooling mechanism over the past several decades. It has been reported to dissipate relatively large heat during the liquid-vapor phase change process compared to the conventional natural and forced convective heat transport process associated with single-phase flow. It has been examined that the cooling devices using single-phase have typically disadvantages such as large pressure drops and streamwise temperature non-uniformity along the liquid channel. On the other hand, phase-change heat transport process using latent heat of vaporization can achieve very high heat fluxes for constant flow rates under a small temperature differential and thus allows maintaining nearly uniform temperature (Ma et al., 1998; Tso and Mahulikar, 2000; Peles and Haber, 2000). Liquid-vapor phase change process is a major mechanism in a variety of phase-change heat transport devices such as heat pipe, capillary pumped

This dissertation follows the style of International Journal of Heat and Fluid Flow.

loop, looped heat pipe, grooved evaporator and condensers, and micro channel evaporator. Recently such phase-change heat transport devices have received much attention for the use of modern thermal management equipments. It has been demonstrated experimentally or theoretically that the effective thermal conductivity in phase-change heat transport devices can be several orders of magnitude greater than that of copper due to the benefit of latent heat during liquid-vapor phase-change process. In addition, such a phenomenon is a prime mechanism in nucleate boiling heat transfer where the thin film evaporation plays a primary role to make vapor bubble growing up within liquid pool with heating (Stephan and Hammer, 1994; Reyes and Wayner, 1997; Kern and Stephan, 2003a; Kern and Stephan, 2003b).

In the past several decades a variety of theoretical models have been developed for heat and mass transport associated with the liquid-vapor phase-change heat transport phenomena. Fundamentally, most of the researches have been based on a thin film evaporation concept of Wayner and co-workers (Potash and Wayner, 1972; Wayner et al., 1976). They investigated the evaporation of a liquid meniscus in a tiny area where the liquid-vapor interface approaches a wall. In spite of the small geometrical dimensions, a considerable amount of the supplied heat at the evaporator wall flows through the so-called thin film or transition film region. It has been found that in this region, microscale effects such as adhesion forces and interfacial thermal resistance in combination with a strong curvature change of the phase interface significantly influence local heat and mass transfer (Kern and Stephan, 2003a).

Although numerous extensive experimental or theoretical works on the thin film evaporation have been conducted, the fundamental understandings have not been achieved yet. Therefore, more advanced experimental techniques and analytical models capable of considering more realistic physical situation have been required for better understanding of the microscale heat and mass transport phenomena.

1.2 Engineering Applications of Phase Change Heat Transport

Capillary driven phase-change heat transport devices have several advantages over conventional single-phase systems. They are passively operated by means of capillary forces, so they need not any external power supply, which allows the cooling devices to be manufactured in compact size and light weight that are definitely required in modern microelectronic devices. In addition, they contain no mechanically moving parts and thus are free of vibration and noise, which increase the reliability of the system. Capillary phase-change heat transport devices have a number of commercial and military applications in terrestrial and space thermal management systems such as cooling systems for electronic components, avionics, satellites, notebook computer, refrigerator, air-conditioning, thermal protection of hypersonic and reentry vehicles, and heating systems for aircraft anti-icing, deicing of engine cowl, and road and bridge deicing.

Heat pipe and capillary pumped loop (CPL) are representatives using the capillary driven phase-change heat and mass transport process for a variety of cooling applications. The schematics of conventional heat pipe and CPL are illustrated in Figs. 1.1 and 1.2. The structures and the fundamental operating principles are very similar.

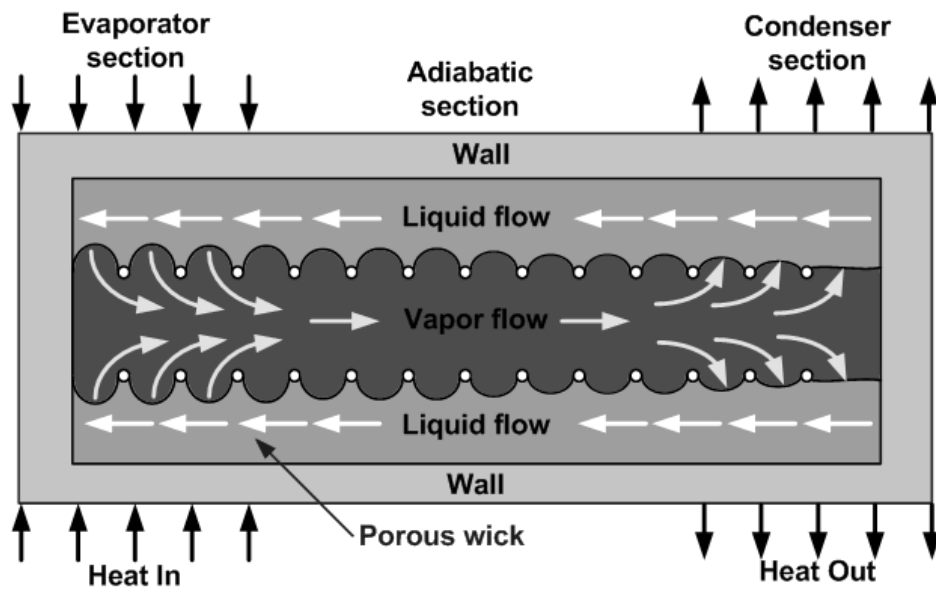


Fig. 1.1. Schematic of conventional heat pipe.

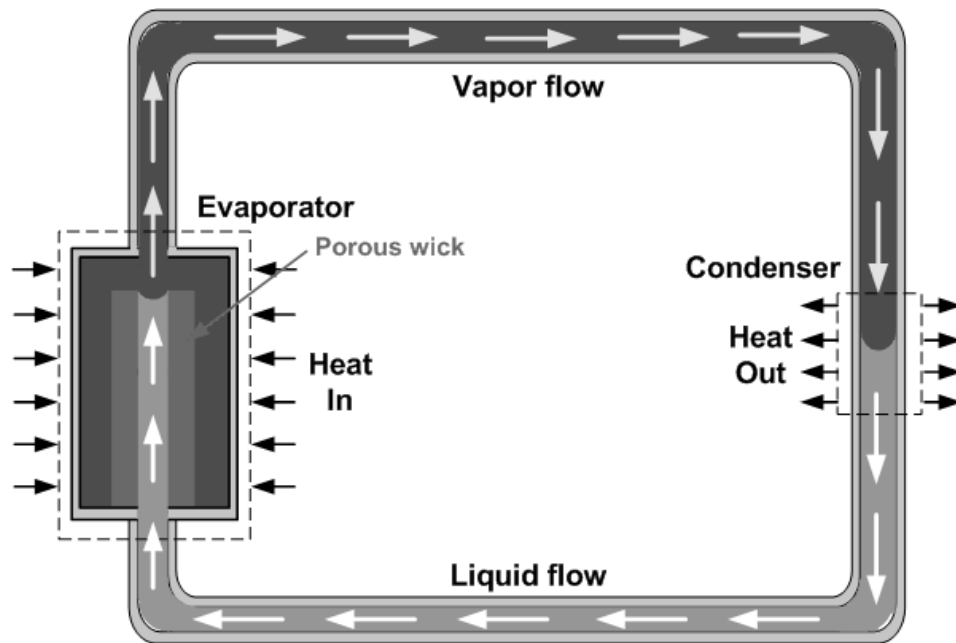


Fig. 1.2. Schematic of capillary pumped loop.

They are comprised of four major parts: evaporation section, condensation section, vapor line and liquid line. Heat pipes are passively pumped by means of capillary forces. The capillary forces are developed in a porous wick structure located within the evaporation section. When the evaporator is heated by external heat source, the working fluid evaporates in the porous wick structure. The evaporated vapor travels to condenser section by pressure gradient. At the condenser section, heat is removed to heat sink and then the vapor recondenses into liquid. The liquid returns back to the evaporator section by capillary action in the porous wick structure. This continuous cycle of vaporization and condensation transfers large amount of heat effectively. The capillarity of transporting large amounts of thermal energy between two terminals with a small temperature differential is equivalent to having an extra high thermal conductivity according to Fourier's law. In addition to its superior heat transfer characteristic, the heat pipe is structurally simple, relatively inexpensive, insensitive to the gravitational field and silent and reliable in its operations (Tien, 1975; Dunn and Reay, 1994; Faghri, 1995). The porous wick structure can be idealized by a bundle of microscopic capillary pores as schematically illustrated in Fig. 1.3. Each capillary pore can be modeled as a micro channel with heat flow from the wall. The present research concentrates on an evaporating extended meniscus within such heated capillary pore since it has been found experimentally or analytically that maximum evaporative heat and mass transport take place in the thin film region of the evaporating extended meniscus.

CPLs have also the same operating principles as conventional heat pipes. In contrast to the conventional heat pipes, CPLs have unique feature that is the wick

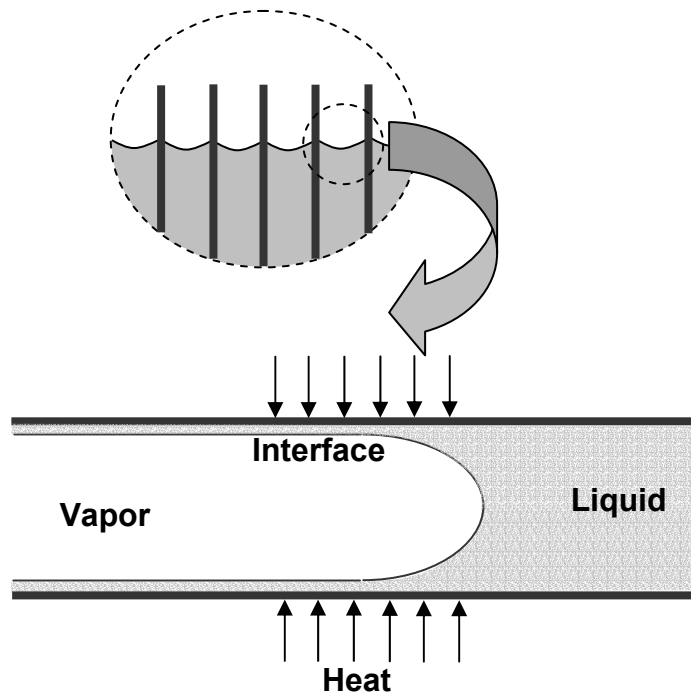


Fig. 1.3. Idealized porous wick structure with a bundle of microscopic capillary pores and an idealized capillary pore with heating.

structure isolated from the evaporator section. This allows CPLs to transfer relatively large heat over long distance since smooth wall tubing can be employed in the construction of the vapor and liquid transport lines as well as in the condenser zone, which avoids the significant liquid flow losses in the wick materials experienced in a conventional heat pipe. Thus, this results in a higher heat transport capability than that of conventional heat pipes. Extensive experiments have demonstrated that CPLs have enough potential to be used in advanced space-based thermal control system (Ku, 1993).

Recently micro heat pipes have received much attention for their promise to dissipate high-power densities since Cotter (1984) first proposed them. He defined a micro heat pipe as a wickless heat pipe in which the radius of curvature of the liquid-vapor interface is comparable in magnitude to the hydraulic radius of the flow channel. Their promise comes from the effective heat transport associated with phase change and their small geometry. Laplace-Young equation states that small hydrodynamic diameter associated with the geometry of micro heat pipe gives rise to high capillary force to pump liquid flow efficiently. For this reason, recently micro heat pipes have received much attention for cooling schemes of integrated circuits. The performance of micro heat pipes are extensively studied by Ma et al. (1994), Peterson and Ma (1999). An overview of the micro heat pipe has been done by Peterson (1992).

In nucleate boiling processes, the fluid flow and heat transfer associated with bubble growth also have been described by an evaporating liquid film as illustrated in Fig. 1.4 (Stephan and Hammer, 1994; Mitrovic, 1998; Son et al., 2002; Kern and Stephan, 2003a). A liquid film is assumed to exist between the vapor in the bubble and

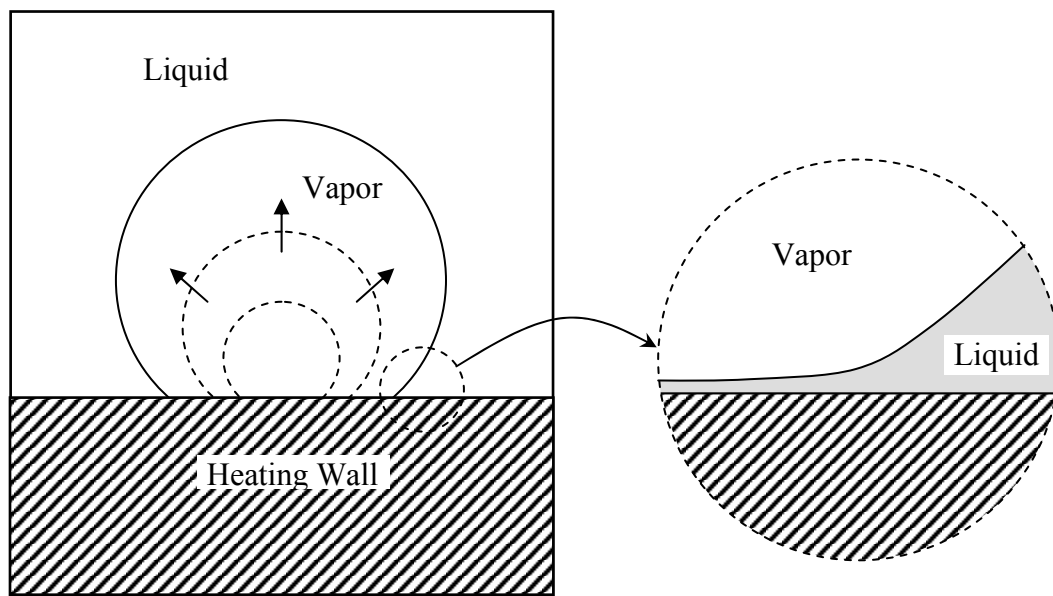


Fig. 1.4. Nucleate boiling heat transport: single bubble model.

the heated wall. In the models, the heated surface is connected to the vapor by a thin liquid film. The inner region of the film is considered as non-evaporating adsorbed film region due to a strong adhesion force, while the outer region of the film is the evaporating film. The evaporating liquid is re-supplied from the bulk meniscus region by liquid flow, which is driven by the combined action of capillary and disjoining pressures that are developed during an evaporation process in thin film region forming within typical porous wick structures.

1.3 Literature Review

In this section past major researches on the evaporating extended meniscus and laser induced fluorescence (LIF) thermometry are reviewed.

1.3.1 Evaporating Extended Meniscus

The foundation of thermodynamics and fluid flow for an evaporating thin film was established by Derjaguin and coworkers (Derjaguin and Zorin, 1957; Derjaguin et al., 1965). They introduced the concept of disjoining pressure to consider an intermolecular interaction force, so called van der Waals force, between liquid and solid molecules in the analysis of thin film evaporation.

Potash and Wayner (1972) used first the concept of a disjoining pressure to describe evaporation from a steady state, two-dimensional, extended meniscus on a heated vertical flat plate immersed in a liquid. They identified two important regions: a microscopic adsorbed film, in which the superheated liquid is restrained from

evaporation by strong intermolecular forces, and a curvature-controlled bulk meniscus, in which the liquid flow is dominated by capillary force. Different models were employed for describing transport processes in these two regions, which demonstrated discontinuities in the solutions, but that showed the essential features of evaporating menisci. They concluded that the pressure gradient and evaporative mass flux reached a maximum in an evaporating thin film region of the extended meniscus.

Wayner et al. (1976) examined evaporation from a stable extended meniscus formed on an inclined flat plate for non-polar liquids. Their analysis was based on the assumption that liquid flow into the evaporating extended meniscus resulted from a change in the meniscus profile creating the required disjoining pressure gradient. They modeled the fluid mechanics using boundary-layer type approximation in the thin film region with the characteristics of thin film having small interfacial slope and low Reynolds numbers. They also demonstrated that the heat transfer coefficient increased rapidly from zero at the adsorbed film to a constant value at the end of transition region over a very short distance.

Renk and Wayner (1979a, 1979b) conducted experimental and analytical works to examine an evaporating extended meniscus of ethanol. In their experiment, they measured the meniscus profile using interferometry technique and found that the meniscus shape was dependent on the applied heat flux. In their analysis, they found that the liquid flow resulting from change in the meniscus shape supplied liquid to the evaporation region and noted that the local evaporative heat transfer increased in the transition region.

Holm and Goplen (1979) developed an analytical model to describe heat and mass transfer in trapezoidal capillary grooves. They noted that about eighty percent of the total heat dissipation occurred in the transition film region. By combining the analytical model of Potash and Wayner (1972) and the experimental results of Derjaguin and Zorin (1957), they uniquely developed an analytical model for disjoining pressure of water.

Moosman and Homsy (1980) developed a second order differential equation for the liquid-vapor interfacial shape from a normal stress balance equation including disjoining pressure. The differential equation was solved by perturbation analysis. They determined the meniscus profile and the evaporative heat flux in a horizontal extended meniscus. Their analysis showed that the maximum heat flux and evaporative mass flux occurred in the transition region where the thermal resistance was small.

Cook et al. (1981) determined experimentally that a change in the thin film thickness profile of decane on a silicon substrate influenced the characteristics of fluid flow and heat transfer within an evaporating liquid thin film. They used a scanning microphotometer to determine the thickness profile by measuring the relative location of interference fringes formed in the film by the reflection of light. Since various mechanisms causing fluid flow are a function of the film profile, it is able to be used to evaluate their effects on evaporative heat transfer.

A series of studies (Tung et al., 1982; Tung and Wayner, 1984; Wayner et al., 1985) also used the scanning microphotometer to determine the heat transfer characteristics of a thin steady state evaporating liquid film forming on an inclined

silicon substrate which was partially submerged in a pool of liquid. The substrate was heated to cause liquid to evaporate from the liquid meniscus, resulting in liquid flow from the pool to the meniscus. They demonstrated that the optical techniques were very useful to determine the film profiles of hexane and decane forming on silicon surface.

Mirzamoghadam and Catton (1988) developed an analytical model of an evaporating meniscus developing on an inclined heated copper plate submerged in a non-polar liquid pool at various angles. They showed that the heat and mass transport and performance were dependent on angle of inclination of the plate and an angle of twenty to thirty degrees yielded an increase in the heat transfer coefficient by a factor of seven compared to a horizontal case.

Stephan and Busse (1992) uniquely calculated the heat and mass transport phenomena in the thin film region and then combined the solution with the macroscopic meniscus within a heat pipe with open grooves. They found that the heat transfer in micro region could have a significant influence on the overall macroscopic heat transfer. They showed that the maximum evaporation rate occurred in the transition region and that nearly 75 % of the heat dissipation occurred in this region despite its small geometrical dimensions.

Schonberg and Wayner (1992) provide an analytical solution for integral contact line evaporative heat sink including film conductivity effects. In the model, capillary and Marangoni effects were ignored. They identified that the Hamaker constant, thermal conductivity, latent heat and superheat enhanced the maximum integral heat sink which

was the heat adsorbed by the entire meniscus and viscosity had a detrimental effect to make large pressure drops which hinder evaporation.

Swanson and Herdt (1992) investigated the fluid flow and heat transfer in a three-dimensional capillary pore geometry by incorporating Marangoni convection, London-van der Waals dispersion forces, and nonisothermal interface conditions. They assumed a Hagen-Poiseuille flow field for the liquid in the meniscus and thin film regions and obtained the change in the meniscus shape with varying dispersion number. They showed that the local evaporative mass flux increased dramatically as the dispersion number increased.

Chebaro et al. (1992) and Chebaro and Hallinan (1993) provided the extension of the theoretical treatment developed by Wayner and Schonberg (1990) to a pore geometry. They analyzed the thin liquid film of an evaporating interface within a micropore under isothermal conditions, which was a simplified assumption of an interface temperature equal to the saturation temperature: however, the assumption of isothermal interfacial conditions was unrealistic since this assumption caused the evaporation rate to peak in the meniscus region instead of the thin film region. Such an abnormality was improved by considering more realistic nonisothermal condition (Hallinan et al., 1994). They yielded a non-dimensional equation for the thin film interfacial shape by combining the mass conservation along the thin film and the augmented Laplace-Young equation. The resulting fourth order nonlinear ordinary differential equation was solved by a shooting method. They uniquely provided the four boundary conditions needed to solve the equation.

DasGupta et al. (1993a, 1993b) measured the evaporating thin film profiles as a function of the evaporation rate using ellipsometry and image processing interferometry. They also developed a numerical model to evaluate the experimental data using numerical solutions of equilibrium and non-equilibrium models based on the augmented Young-Laplace equation. They obtained Hamaker constant from the experimental data and noted that it was not a function of the evaporation rate. It was also noted that the fluid flow in the thin film resulted from the disjoining pressure gradient.

Hallinan et al. (1994) developed a model to describe the evaporating thin film within micropores of porous wick structure of a heat pipe under nonisothermal condition and thus accounted for thermocapillary stresses at the interface condition. They extended the study of Chebaro and Hallinan (1993) to consider a more realistic nonisothermal evaporating extended meniscus. They justified the effect of circumferential curvature term on the flow of the liquid in the extended meniscus could be negligible, which made the mathematical formulation for the interfacial shape more simplified. They also found that maximum evaporative fluxes were present in the extended meniscus with constant wall temperature. In the scaling analysis, they demonstrated that the thermocapillary stresses become more important as superheat, pore size and slope of surface tension verse temperature increase and diminish for higher cohesion and adhesion forces. They also demonstrated that vapor recoil stresses become more significant as surface tension effects are diminishing with increasing pore size.

He and Hallinan (1994) developed a mathematical model for the investigation of the effect of thermocapillary stress on the thin film evaporation. The mathematical

formulation was based on the perturbation theory of Burelbach et al. (1988). They found that the thermocapillary stresses significantly affect the flow field and heat transfer within the extended meniscus even when the extended meniscus heat transport is very small. Using scaling arguments, they defined a critical Marangoni number to estimate the liquid flow choked in the film as a result of the thermocapillary effect. It was noted that small sized pore was more effective to overcome the impact of thermocapillary stresses on the replenishment of the liquid flow. Such a trend was also found in the experiment of Pratt et al. (1998).

Park et al. (2003) developed a mathematical model to describe the transport phenomena for a thin film region of a micro channel with a non-polar liquid under isothermal conditions. They showed that the gradient in the vapor pressure had a significant influence on the thin film profile. They found that the length and the maximum thickness of the thin film decreased exponentially as the heat flux increased.

1.3.2 Laser Induced Fluorescence Thermometry

Coppeta and Rogers (1998) tried to measure dual emission laser induced fluorescence for some scalar behavior such as pH and temperature distribution. In their experiment, numerous combinations of fluorescent dyes were used for ratio technique to determine their compatibility in the measurement technique. Especially, they discussed three main spectral conflicts usually encountered in ratiometric technique using fluorescence, where the conflicts are associated with the overlaps between absorption and emission bands.

Coolen et al. (1999) measured the temperature field of a natural convection flow using laser induced fluorescence with only one fluorescence dye sensitive to temperature. They proposed a normalization of calibration function every experiment using two reference intensity fields at different temperatures to correct measurement errors resulting from the intensity variation between different experiments. They demonstrated that photobleaching and shadowgraph effects could lead to errors of temperature measurement usually encountered in laser induced fluorescence technique.

Sakakibara and Adrian (1999) described a two-color laser induced fluorescence technique to measure the instantaneous three-dimensional temperature field in water. In the experiment, Rhodamine-B was used for temperature sensitive dye and Rhodamine-110 was for non-temperature sensitive dye. They successfully measured the three dimensional temperature field of thermal convection from a horizontal surface with uniform heating.

Hidrovic and Hart (2002) used a two-dye laser induced fluorescence ratiometric scheme to get a two-dimensional thickness and temperature mapping of fluids. They developed a liquid film thickness measurement using emission reabsorption in an optically thick system, which has been considered to be detrimental to the measurement of most scalars such as temperature and pH. They also made use of such a ratiometric technique at the temperature mapping in an optically thin system.

Recently, Kim et al. (2003) used ratiometric laser induced fluorescence to examine its capability for microscale full-field temperature mapping. They measured the temperature field resulting from thermal buoyancy inside a cuvette with 1 mm width.

They showed that the measured temperature fields were consistent with numerically predicted results with spatial measurement resolution of 0.92°C for $76\ \mu\text{m}$ resolution.

Lee (2003) measured a temperature field of natural convection within rectangular cuvette using ratiometric LIF thermometry. He discussed extensively the difficulties encountered in the measurement of heated meniscus region in a capillary pore due to reabsorption resulting from total internal reflections of laser light at the liquid-vapor interface.

1.4 Summary of Research Objectives

1.4.1 Numerical Analysis

According to most of the previous researches on the evaporating thin film, several typical features have been found in the thin film evaporation process. It was concluded that the maximum evaporative heat and mass transport occurs in the transition film region where the intermolecular force and capillary pressure are equally important to the evaporation phenomena and the thermocapillary stress also have a significant effect on the thin film evaporation. Therefore, it is essential to understand microscopic fluid flow and heat/mass transport phenomena taking place in the evaporating extended meniscus to design the efficient capillary phase-change heat transport devices and improve their performance.

In the numerical part, a mathematical modeling is developed for the extensive understanding of microscale heat and mass transport phenomena occurring in an evaporating extended meniscus, especially concentrating on thin film region. The

dimension of evaporating phenomena is so small that it is nearly impossible to study the evaporation process in experimental methods. Therefore, theoretical and analytical researches in the thin film evaporation have been concentrated, however, the complete understanding has not been achieved yet. In this work, extensive numerical investigations are uniquely performed by considering several specific effects such as thermocapillary effects, slip boundary condition at wall, polarity effect of working fluid and binary mixture evaporation, all of which have been considered to play important roles in the thin film evaporation. The successful analytical solutions can provide a better understanding of the fluid flow and heat and mass transport within the evaporating thin film formed in the phase-change heat transport devices.

1.4.2 Experimental Investigation

The extremely small spatial dimension of the transition film region to be investigated gives rise to several problems for measurements. For example, even the smallest available thermocouples are still one or two orders of magnitude bigger than the dimension of the transition film region. As a result, other promising alternative to the conventional measurement technique is necessary such as the various optical diagnostic techniques using laser optics recently have extensively received attentions due to their characteristics of non-intrusive and high resolution.

In experimental part, recently developed a ratiometric laser induced fluorescence thermometry is introduced, which is expected to be a potential measurement technique for temperature fields in microscale geometry. The potential and applicability of the

ratiometric laser induced fluorescence thermometry to the thin film region will be discussed by measuring the temperature fields established inside a heated glass channel of 1 mm by 1 mm square cross section.

CHAPTER II

BACKGROUND

2.1 Evaporating Extended Meniscus

In capillary tube, there exists a curved shaped liquid-vapor interface, which is usually called meniscus. Normal stress balance across the meniscus is described by Laplace-Young equation, which states that the interfacial pressure differential balances with capillary force. The capillary force is a pumping head for a liquid column going up against gravity within capillary tube. This conventional Laplace-Young equation describes the normal force balance applicable only in macroscale. In molecular level an additional force existing between liquid and solid molecules should be considered in the force balance which is called disjoining pressure proposed by Russian scientist Derjaguin. The disjoining pressure describes the molecular adhesion of liquid molecular interacting with solid molecules of the wall, which makes the liquid film spread out along solid wall. This phenomenon is defined as spreading. In ideal, if the liquid is pure and the solid wall is perfectly clean, the meniscus will extend infinitely. Thus, spreading phenomena occur as a result of the disjoining pressure, and such spreading liquid film is called extended meniscus. In the case of heat applied from the wall, such curved shaped spreading system is defined as evaporating extended meniscus. While a number of extensive studies on fluid flow and heat transport of the evaporating extended meniscus have been performed experimentally or analytically, a complete understanding has not been achieved yet.

In change-of-phase heat transport devices, capillary forces drive overall circulation of working fluid from an evaporator section to a condenser section, whereas the thin film flows at the evaporating meniscus are driven by capillarity and disjoining pressure gradient. Figure 2.1 shows an evaporating extended meniscus developed on the wall within a capillary pore. The extended meniscus is composed of three distinct regions (Potash and Wayner, 1972): the adsorbed film, the thin film, and the bulk meniscus. The distinction between the three regions is based on the relative importance of the forces associated with the interactions of liquid-vapor and solid-liquid. The adsorbed film region, nearly constant in thickness, cannot be modeled by continuum theories and is dominated by extremely strong short-range intermolecular forces between the liquid molecules and the solid substrate as described by Israelachvili (1992) which restrain superheated liquid molecules from evaporation in that region, so it is called as non-evaporation region. While the adsorbed film region is governed by the disjoining pressure due to intermolecular interactions, the bulk meniscus region is dominated by capillary forces in which the evaporative flux is less due to the resistance to thermal conduction in the liquid film as the film thickness increases as shown in Fig. 2.1. The thin film region, which is called a transition region, exists between the bulk meniscus and the adsorbed film region. The effect of capillarity and disjoining pressure are equally important in this region for fluid flow and heat transfer. According to previous works, it has been identified that the maximum evaporative heat and mass transport take place in the thin film region (Potash and Wayner, 1972; Moosman and Homsy, 1980; Stephan and Busse, 1992; Hallinan et al., 1994). Therefore, it is very importance to better

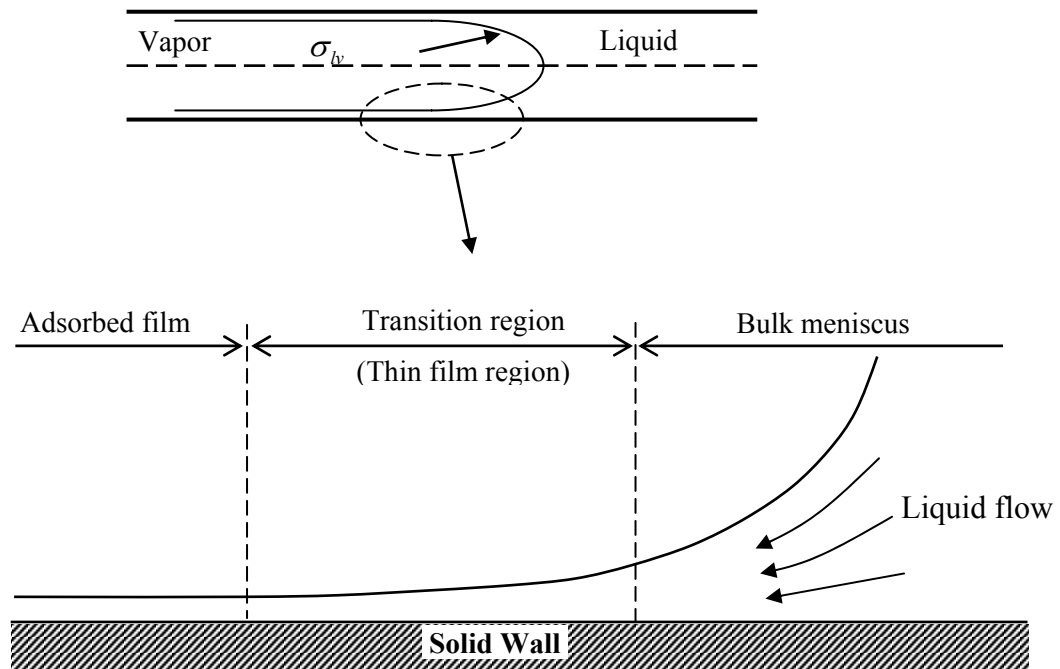


Fig. 2.1. Idealized model of extended meniscus within a capillary pore: adsorbed film, thin film (transition film), bulk meniscus region.

understand the heat and mass transport phenomena taking place within phase-change transport devices to make sure the stable operation and to enhance the performance.

2.2 Physics of Interfacial Phenomena

2.2.1 Surface Tension

The apparent interfacial tension or surface tension is equivalent to an energy stored in the interface region per unit area. The magnitude of the surface tension for a substance is directly linked to the strength of intermolecular forces in the material. Non-polar liquids typically have the lowest surface tension. Water and other polar molecules have somewhat higher surface tension, and liquid metals such as mercury, which exhibit metallic bond attraction, have very high surface tension. The surface tension for any pure liquid varies with temperature. It decreases almost linearly with increasing temperature, vanishing altogether at the critical point where the distinction between phases disappears (Carey, 1992).

Surface tension is a major effect producing capillary pumping force in capillary driven phase-change device. Liquid pressure gradients, leading liquid flow in evaporation region, are composed of disjoining pressure gradients and capillary pressure gradients. This capillary pressure is created by the action of surface tension of the liquid and curvature effect of meniscus shape. When heat is applied to the liquid through heated substrate, the gradient in the surface tension along the liquid-vapor interface introduces thermocapillary stress, which critically influences the stability of evaporation process. The thermocapillary stresses will be explained in subsequent section.

2.2.2 Wettability

Wetting behavior of a liquid on a solid surface is of critical importance in industrial processes such as thin film lubrication, coating of solids, and thin film evaporation associated with phase-change heat transport. In the engineering application of heat and mass transport phenomena, the proper utilization of surface wettability can improve the heat transport effectiveness by yielding a flow field that will enhance heat transfer. The understanding of wetting phenomena is crucial for optimum design of an advanced heat exchanger which will provide the highest heat transfer rate at the lowest overall cost (Mirzamoghadam and Catton, 1988).

The way, however, in which the liquid and vapor contact the solid walls through which the energy is transferred, will strongly affect the resulting heat and mass transfer in the system. Consequently, the performance of heat transport equipment in which vaporization or condensation occurs may strongly depend on the way the two phases contact the solid walls. It can be observed that the behavior of liquid in contact with solids may vary from one surface to another and with the type of liquid (Carey, 1992).

The degree of the affinity of liquids for solids is referred to as the wettability of the liquid, which is quantified by the contact angle. Young equation described a macroscopic wettability from balance of related forces on a contact line. In contact line region, the force balance at point 0 produces the relationship of interfacial tensions of three phases at equilibrium as shown in Fig. 2.2,

$$\sigma_{sv} = \sigma_{sl} + \sigma_{lv} \cos \theta_c \quad (2.1)$$

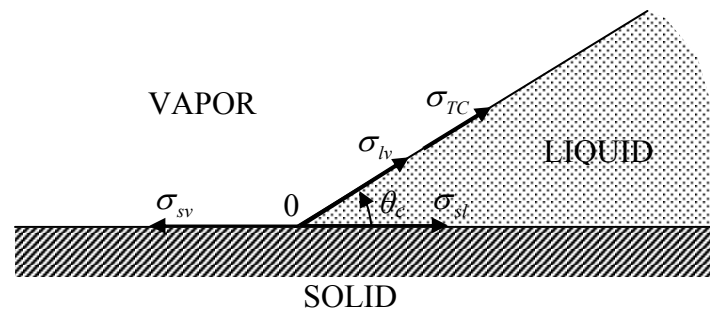


Fig. 2.2. Balance of interfacial tensions on a contact line.

where θ is contact angle which represents a macroscopic wetting characteristics. When a liquid is in contact with a solid surface, one of three conditions is possible at equilibrium: complete wetting ($\theta_c = 0$), partial wetting ($0 < \theta_c < 90^\circ$), or nonwetting ($\theta_c > 90^\circ$). In Eq. (2.1), σ_{sv} , σ_{sl} and σ_{lv} are interfacial tensions between solid-vapor, solid-liquid and liquid-vapor, respectively. The interfacial tension between liquid-vapor is generally called as surface tension that decreases with increasing temperature. As θ_c decreases, the liquid spreads more over the solid surface. Equation (2.1) can be rearranged to the form,

$$\cos \theta_c = \frac{\sigma_{sv} - \sigma_{sl}}{\sigma_{lv}} \quad (2.2)$$

Under heating condition, Eq. (2.2) is modified by considering thermocapillary stresses resulting from imbalance of surface tension along interface (Pratt and Hallinan, 1995),

$$\cos \theta_c = \frac{\sigma_{sv} - \sigma_{sl}}{\sigma_{lv} + \sigma_{TC}} \quad (2.3)$$

where σ_{TC} represents the thermocapillary stresses which result from the gradient of interfacial temperature. Equation (2.3) shows that liquid having lower surface tension gives a smaller contact angle which in turn elongates the liquid film longer on the solid wall. In addition, it also indicates that lower thermocapillary stress makes the liquid film extended. Therefore, to enhance the wettability of the liquid film it is necessary to employ the liquid having lower surface tension and lower thermocapillary stress. Even though Young's equation is applicable only to contact line region where three phases meet, it provides us the intuition of wettability of the liquid film forming on solid wall.

Young's equation provides a basic idea of how to enhance the wettability in the liquid-vapor phase-change transport in order to improve the effectiveness of heat and mass transfer process.

Another parameter indicating the wetting characteristics is wicking height which is defined as the liquid column height within a capillary tube. The wicking height is most easily measurable macroscopic wetting characteristic of a liquid in a capillary tube. Ma et al. (1998) conducted a theoretical work to better understand the wetting characteristics of evaporating liquid in a heated capillary tube. By comparing the numerically obtained wicking height with experimental results, they identified that the wettability of a liquid was influenced by the combined effects of thermocapillary stresses, capillary forces, dynamic flow effect and disjoining pressure. Pratt and Hallinan (1997) experimentally showed that the relationship between the liquid-vapor interfacial temperature gradient and the wetting characteristics of a liquid within capillary pores. They demonstrated that thermocapillary stresses in the transition film region of the evaporating extended meniscus degrade the wettability of the liquid by reducing the wicking height. As a result, the degradation of wetting leads to a reduction of heat and mass transport in the devices. Pratt and Kihm (2003) experimentally demonstrated that the thermocapillary stresses could be counteracted by concentration gradients associated with distillation process in binary mixture evaporation.

In practice, the phase-change heat transport encountered the capillary heat transport limitation rarely. Of the possible reasons of this unexpected motion of the devices, it has been remarkable that design predictions over-predict the wetting

characteristics since they are based on a maximum capillary potential which presumes that the liquid within the porous structure is perfectly wetting and static conditions exist at the evaporating meniscus. Thus, it is important to identify the detrimental effects which degrade the wetting ability of the working fluid in capillary driven heat transport equipments (Pratt and Kihm, 2003).

2.2.3 Disjoining Pressure

The notion of disjoining pressure was first formulated in 1936 based on experiments with thin aqueous interlayers formed between two flat mica surfaces (Churaev, 2003). After then the concept of disjoining pressure was established by Derjaguin et al. (1965) to account for the intermolecular interaction force in thin liquid film, where the conventional hydrodynamics is not applicable to explain the molecular interaction force. Over the past several decades, the concept of disjoining pressure has been incorporated into various analytical models for the fluid flow and the heat transfer in the evaporating extended meniscus to describe the effect of molecular interaction between liquid molecules and solid molecules at wall. A historical review of disjoining pressure of Derjaguin and his co-workers has done by Churaev (2003). In practice, the disjoining pressure for non-polar liquids is expressed as a simple polynomial function of thin film thickness and dispersion constant. On the other hand, for polar liquids the disjoining pressure is presented in the form of a logarithmic function of thin film thickness and thermal properties. Due to the complexity of the disjoining pressure of polar liquids, non-polar liquids have been used in various extensive models to examine

the effect of the disjoining pressure on heat and mass transport of phase-change evaporation phenomena.

DasGupta et al. (1993b) experimentally obtained the value of the disjoining pressure and Hamaker constant using optically measured extended meniscus profiles. Using the experimentally obtained parameters, the thickness of adsorbed film was obtained for varying superheat conditions. The liquid film was influenced by long-range intermolecular forces, in particular van der Waals forces. According to their previous analytical models, it was noted that these forces might locally degrade evaporation, but might become a major driving force for liquid flow into the thin film region from a bulk pool.

2.2.4 Vapor Recoil

Since mass is conserved at the liquid-vapor interface during the evaporation process, the slowly moving liquid particles are accelerated dramatically upon evaporation due to the significant difference in densities between the liquid and the vapor. As a result of the vapor velocity being much larger than the liquid velocity, an additional normal force is introduced in the form of the evaporative mass flux times the vapor velocity. This normal force can be considered to be as an additional pressure acting down on the liquid-vapor interface. Such normal force exerted on the liquid-vapor interface by these escaping liquid particles is called vapor recoil (Burelbach et al., 1988; Anderson and Davis, 1995). The vapor recoil stresses are maximal in the thin film region since the local evaporation rate becomes to peak there as stated previously. Scaling

analysis of Hallinan et al. (1994) showed that the contribution of vapor recoil stresses to the normal stress balance is negligible relative to the disjoining and capillary pressures when surface tension decreases with increasing capillary pore size. For the simplicity in the mathematical formulation, the effect is not included in this study.

2.3 Thermocapillary Effects

The dynamic behavior resulting from evaporation in the liquid film have a significant effect on the wettability of working fluid in porous wick structure of capillary phase-change devices. Fluid flow and heat transfer of evaporating liquid film give rise to the temperature gradient on liquid-vapor interface which is associated with non-isothermal interface as a result of non-uniform temperature along solid wall and non-uniform evaporation of the liquid film. As the film thickness increases, temperature at the liquid-vapor interface decreases since thermal resistance increases with increasing distance from solid wall. Generally, surface tension and temperature are inversely related. Thus, such imbalance of temperature on the liquid-vapor interface induces the gradient in surface tension which is defined as Marangoni effect or thermocapillary effect. The resulting surface shear stress is called thermocapillary stress and the effective surface tension due to the temperature differential makes circulating flow at the transition region and the bulk region, so-called Marangoni circulation. The flow field is coupled to the temperature field through the thermocapillary stress. As stated previously, the capillary pumping ability is decided by the wetting ability of the liquid. Therefore, the thermocapillary stress have a detrimental effect on the capillary pumping potential by

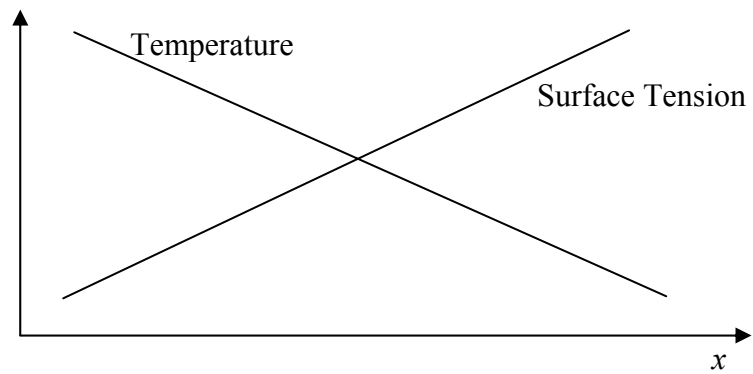
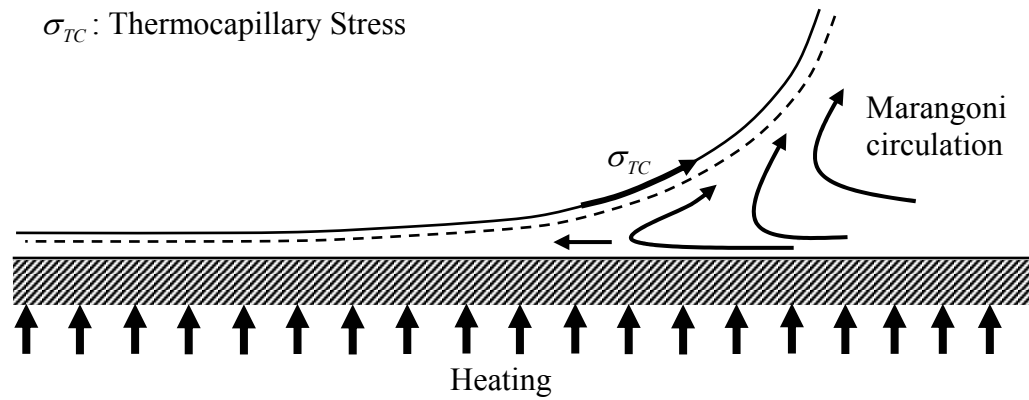


Fig. 2.3. Schematic for explanation of thermocapillary stress.

pulling the liquid film toward the bulk meniscus region. As shown in Fig. 2.3, the relatively cooler pore center, with higher surface tension, can act to pull the evaporating hotter thin film region with lower surface tension toward the bulk meniscus region, which degrades the wettability of the liquid. Such a degradation of wettability due to thermocapillary effects has been reported in many previous works (He and Hallinan, 1994; Pratt and Hallinan, 1997). As a result, the thermocapillary stresses influence the change of interface shape and thus heat and mass transport at the evaporating thin film, and consequently degrade the stability of evaporating meniscus. A historical review of the Marangoni effect has been done by Scriven and Sternling (1960). The reason of considering the thermocapillary stresses herein is that they play an important role in the microscopic heat and mass transport phenomena at an evaporating extended meniscus.

CHAPTER III

NUMERICAL ANALYSIS

3.1 Mathematical Formulation

To describe steady-state heat and mass transfer one has to consider a nonlinear free-boundary problem; the shape of the evaporating extended meniscus is not known a priori and has to be determined as part of the solution. Once the shape is obtained numerically or experimentally, the other properties can be obtained by utilizing the information of the profile since all other thermo-physical properties such as liquid pressure, interfacial temperature and evaporative mass flux are related to the meniscus shape in equations stated later. In this chapter, the mathematical formulation to achieve the shape of an evaporating extended meniscus and other properties will be described.

The following assumptions have been made for the present mathematical model:

1. The working fluid is Newtonian and compressible.
2. The steady-state operation is considered.
3. Two-dimensional channel flow is considered.
4. One-sided formulation is developed in which only liquid side is considered.
5. Inertia force is neglected.
6. Gravitational body force is neglected.
7. Wall temperature is assumed constant.
8. Heat flux along the channel is uniform.
9. Working fluids in adsorbed region wet completely the wall.

10. The wall is assumed to be perfectly flat and smooth.

11. Vapor recoil stress is not considered.

A one-sided formulation, based on the evaporation model of Buelbach et al. (1988), is developed for liquid side since the properties of vapor phase such as the density, viscosity, and the thermal conductivity are much less than those in liquid phase. This one-sided formulation allows for the determination of the liquid-vapor interface shape without the necessity of computing the thermal and flow fields in the vapor phase (Anderson and Davis., 1995). In microscale flow, the velocity is too low, so the inertia force is negligibly small and the gravitational body force is also small compared to surface force that is also neglected. The mathematical model for the slotted pore geometry is considered in rectangular coordinate frame of reference which is employed with the x -axis along the wall and the y -axis normal to the wall as illustrated in Fig. 3.1. The origin is set at the junction of the non-evaporating adsorbed film region and the evaporating transition region.

3.1.1 Interfacial Normal Stress Balance

The geometry of interest is depicted in Fig. 3.1. An evaporating two-dimensional meniscus is formed in the slotted pore. The liquid is assumed to be heated by a uniform heat flux from a solid substrate causing evaporation from the liquid-vapor interface. It is assumed that the evaporative flow from the thin film is sustained by constant liquid inflow from the bulk meniscus driven by gradients in capillary and disjoining pressure. The wall temperature, T_w , is assumed constant and the vapor phase is assumed to remain

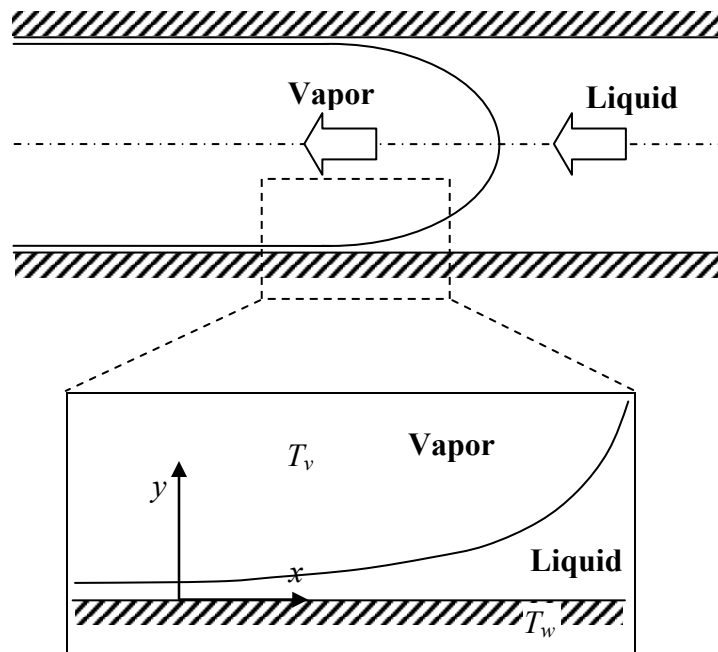


Fig. 3.1. Two-dimensional channel geometry and transition region.

in the saturated state at the temperature of T_v . Especially, the transition region is focused on the analysis because most of the heat and mass transport occur in the region and the understanding of the fluid flow and heat/mass transport phenomena taking place in the region is of major importance in the design and analysis of the change of phase heat transport devices.

The finding of liquid vapor interface profile starts from normal force balance in a liquid-vapor interface by well-known Laplace-Young equation,

$$P_v - P_l = \sigma K \quad (3.1)$$

which describes the relation of hydrostatic pressure and capillary pressure in the liquid-vapor interface. Equation (3.1) is the governing equation describing the normal force balance along the interface encountered in various two-phase interfacial situations having liquid-vapor interface such as bubble, droplet, liquid film and a multitude of phase-change interface.

For molecular configuration, an additional term, which represents the intermolecular interaction force, should be included in Eq. (3.1) yielding a following modified form which is called augmented Laplace-Young equation that represents normal stress balance along the liquid-vapor interface of liquid film,

$$P_v - P_l = \sigma K + \Pi \quad (3.2)$$

where P_v and P_l are the pressure of the vapor and liquid phases, respectively. The film is assumed to be sufficiently flat so that the liquid pressure does not vary in the direction perpendicular to the wall and thus the liquid pressure is a function of axial axis alone. The vapor phase is assumed to have a uniform pressure and temperature. Furthermore, it

is assumed to be in equilibrium with the bulk liquid at temperature T_v that is saturation temperature. Π is the disjoining pressure, which represents the intermolecular interaction force between the liquid and solid molecules present in the thin liquid film, σ is a liquid-vapor interfacial surface tension, and K is a mean curvature of liquid-vapor interface. The curvature for two-dimensional channel geometry is represented in terms of the first and second derivative of the film thickness with the distance along the substrate:

$$K = \frac{d^2 h}{dx^2} \left[1 + \left(\frac{dh}{dx} \right)^2 \right]^{-1.5} \quad (3.3)$$

where h is the thickness of the film. The surface tension is related to the local liquid-vapor interfacial temperature using a linear approximation,

$$\sigma = \sigma_0 - \gamma(T_i - T_v) \quad (3.4)$$

where σ_0 is the reference surface tension at a reference temperature which is chosen as the vapor temperature of T_v , γ is a positive constant for typical liquids which represents the slope in the diagram of temperature versus surface tension, and T_i is the liquid-vapor interfacial temperature. Equation (3.4) gives rise to the thermocapillary effects through the balance of shear stress with surface tension gradients along the liquid-vapor interface, which will be incorporated in a boundary condition of momentum equation. The disjoining pressure for non-polar liquids is expressed in the polynomial function of the film thickness in the non-retarded form (Derjaguin and Zorin, 1957),

$$\Pi = \frac{A}{h^3} \quad (3.5)$$

where $6\pi A$ is the Hamaker constant, which is positive for a completely wetting liquid, and A is called the dispersion constant or the modified Hamaker constant which accounts for the London-van der Waals forces between molecules. On the other hand, the disjoining pressure for polar liquids such as water is expressed in a logarithmic function of the film thickness and the thermal properties. The logarithmic function is difficult to be scaled and the experimental data of intermolecular forces for polar liquids are not available in literatures so that extensive researches of an evaporating thin film for non-polar liquids have been performed due to the relative simplicity of mathematical modeling the intermolecular forces. The effect of polar liquids will be discussed in subsequent section in detail.

The liquid flow in the extended meniscus occurs due to the liquid pressure gradient which replenishes the liquid evaporated in an evaporation region by pumping the liquid from bulk region. The liquid pressure gradient can be determined by differentiation of Eq. (3.2) with respect to x with assumption of constant vapor pressure,

$$\frac{dP_l}{dx} = -\sigma \frac{dK}{dx} - K \frac{d\sigma}{dx} - \frac{d\Pi}{dx} \quad (3.6)$$

The vapor pressure can be considered constant since in many practical cases the vapor pressure drop is very small compared with the liquid pressure drop. Equation (3.6) shows that the liquid flow in the transition film region is controlled by gradients in curvature, surface tension, and disjoining pressure. Of these, the disjoining pressure term makes a major contribution of driving liquid flow into the transition film region. In the case of mixture flow, the effect of a concentration gradient is also added in Eq. (3.6).

3.1.2 Fluid mechanics: Momentum Equation

The thin film is taken to be fairly flat so the dynamics of liquid flow in the thin film region are described by lubrication theory of fluid mechanics, which is the same as a boundary layer approximation,

$$\mu_l \frac{\partial^2 u}{\partial y^2} = \frac{dP_l}{dx} \quad (3.7)$$

To achieve the solution of Eq. (3.7), following boundary conditions are required at solid wall and liquid-vapor interface,

$$u = 0 \quad \text{at } y = 0 \quad (3.8)$$

$$\mu \frac{du}{dy} = \frac{d\sigma}{dx} \quad \text{at } y = h(x). \quad (3.9)$$

The first condition Eq. (3.8) is no slip condition at the wall and the second condition Eq. (3.9) is the shear stress condition at the liquid-vapor interface, which equates the interface shear stress to the change in surface tension. The fluid flows resulting from the surface tension gradient on the superheated liquid surface are generally called thermocapillary flow or Marangoni flow. The gradient of surface tension also can be induced by composition gradients at the liquid-vapor interface, which will be discussed in detail in later section of binary mixture evaporation. The velocity profile is obtained by solving Eq. (3.7) with the boundary conditions Eqs. (3.8) and (3.9),

$$u(y) = \frac{1}{\mu} \left[\frac{dP_l}{dx} \left(\frac{y^2}{2} - hy \right) + \frac{d\sigma}{dx} y \right]. \quad (3.10)$$

The second term in the resulting liquid velocity profile represents the surface tension gradient due to the thermocapillary stress. The mass flow rate is obtained by the integration of the velocity profile over the cross section of height h and unit width,

$$\Gamma = \int_0^{h(x)} \rho_l u dy = -\frac{h^3}{3\nu_l} \frac{dP_l}{dx} + \frac{h^2}{2\nu_l} \frac{d\sigma}{dx} \quad (3.11)$$

where ν_l is the kinematic viscosity of the liquid. The first term accounts for flow rate driven by pressure gradient and the second term accounts for flow rate resulting from surface tension gradient due to the changes in temperature and composition along the liquid-vapor interface. Using the definition of disjoining pressure of non-polar liquid (Eq. (3.5)) in non-retarded form, the relationship of surface tension (Eq. (3.4)) and the curvature with small slope assumption, $K \approx h_{xx}$, Eq. (3.6) can be rearranged,

$$\frac{dP_l}{dx} = -(\sigma_0 - \gamma(T_i - T_v))h_{xxx} + \gamma \frac{dT_i}{dx} h_{xx} + 3Ah^{-4}h_x \quad (3.12)$$

where the subscript x indicates the derivative with respect to x . Combining Eqs. (3.12) and (3.11) one obtains the mass flow rate in terms of the film thickness and temperature,

$$\Gamma = -\frac{h^3}{3\nu_l} \left\{ -(\sigma_0 - \gamma(T_i - T_v))h_{xxx} + \gamma \frac{dT_i}{dx} h_{xx} + 3Ah^{-4}h_x \right\} - \frac{\gamma h^2}{2\nu_l} \frac{dT_i}{dx} \quad (3.13)$$

3.1.3 Evaporative Mass Transfer

Based on kinetic theory, Schrage (1953) related the net mass flux of matter crossing a liquid-vapor interface to a jump change in interfacial conditions at the interface:

$$\dot{m}_{evp} = C \left(\frac{M}{2\pi R} \right)^{\frac{1}{2}} \left(\frac{P_{lv}}{T_i^{1/2}} - \frac{P_v}{T_v^{1/2}} \right) \quad (3.14)$$

where C is the evaporation coefficient, M is the molecular weight, R is the universal gas constant, P_{lv} is the saturation vapor pressure at the interfacial temperature of T_i . Taking the accommodation coefficient equal to one, the evaporation coefficient becomes 2.0 (Schonberg and Wayner, 1992). Equation (3.14) is referred to as the Hertz-Knudsen-Schrage equation, which describes an evaporative mass flux across a flat liquid. In order to extend Eq. (3.14) to curved liquid films, Wayner et al (1976) used an extended Clapeyron equation (Eq. (3.15)) which equates the variation in the interfacial saturation vapor pressure with temperature and disjoining pressure.

$$P_{lv} - P_v = \frac{P_v M h_{fg}}{R T_v T_i} (T_i - T_v) + \frac{V_l P_v}{R T_i} (P_l - P_v) \quad (3.15)$$

where h_{fg} is the latent heat of vaporization and V_l is the liquid molar volume. The vapor phase is assumed to have a uniform pressure and temperature. As a result, using the approximation of $T_i^{1/2} \approx T_v^{1/2}$ and substituting Eq. (3.15) into Eq. (3.14), the evaporative mass flux for a curved liquid film is obtained as,

$$\dot{m}_{evp} = C \left(\frac{M}{2\pi R T} \right)^{1/2} \left\{ \frac{P_v M h_{fg}}{R T_v T_i} (T_i - T_v) + \frac{V_l P_v}{R T_i} (P_l - P_v) \right\} \quad (3.16)$$

Equation (3.16) states that evaporation mass flux leaving the liquid-vapor interface is modeled as a function of the temperature and pressure jump at the interface. As a result, the local evaporation rate is a function of the local superheat and the local liquid pressure. The resistance to transport in the vapor phase in the actual process is ignored in the

model. The pressure jump at the liquid-vapor interface accounts for the reduction in the evaporation mass flux due to the capillary pressure and disjoining pressure by the interfacial normal stress balance equation given by Eq. (3.2) (Wayner and Schonberg, 1990; Wayner, 1991). Multiplying the latent heat of vaporization by the evaporative mass flux, the evaporative heat flux is obtained,

$$q''_{evp} = \dot{m}_{evp} h_{fg} \quad (3.17)$$

Thus, the evaporative heat flux depends on a difference in the temperature and pressure across the liquid-vapor interface.

3.1.4 Thermal Field and Heat Transfer: Energy Equation

The evaporative heat flux depends on the interfacial temperature. The liquid-vapor interface temperature can be obtained using the steady-state energy equation. The thickness of the liquid film is so small that the conduction heat transfer through the liquid thin film is assumed to be present only the direction perpendicular to the solid surface. According to Stephan and Busse (1992), the calculated normal temperature gradients are several orders of magnitude larger than the gradients parallel to the surface. Also, the conduction heat transfer rate from the wall through the liquid film to the liquid-vapor interface balances to both of evaporation and convection at the interface (Moosman and Homsy, 1980). Of these two, evaporative heat transfer is dominant. Thus, the conduction heat transfer rate would be equal to the evaporation heat flux at the interface. This yields a simplified energy equation resulting in one dimension conduction equation,

$$\frac{d^2T}{dy^2} = 0 \quad (3.18)$$

Two boundary conditions are necessary at wall and the liquid-vapor interface for obtaining the temperature distribution,

$$T = T_w \quad \text{at } y = 0 \quad (3.19)$$

$$-k_l \left. \frac{dT}{dy} \right|_{y=h} = \dot{m}_{evp} h_{fg} \quad \text{at } y = h \quad (3.20)$$

where k_l is the thermal conductivity of the liquid. These correspond to a specified wall temperature and a balance between conduction and evaporation heat transfer at the liquid-vapor interface, respectively. Solution of the energy equation (Eq. (3.18)) subject to these boundary conditions gives the temperature variation along the interface,

$$T_i(x) = -(\dot{m}_{evp} h_{fg} / k_l)h(x) + T_w \quad (3.21)$$

With the substitution of the evaporation mass flux given by Eq. (3.16) into Eq. (3.21), the interfacial temperature is related with the film thickness, superheat, capillarity and disjoining pressure. As a result, the liquid-vapor interfacial temperature is a function of position.

3.1.5 Mass Conservation in the Transition Film Region

Considering mass conservation in the thin film, the evaporative mass flux is related to the change in mass flow rate for differential length as illustrated in Fig. 3.2,

$$\Gamma_{x+\Delta x} = \Gamma_x + \dot{m}_{evp} \cdot \quad (3.22)$$

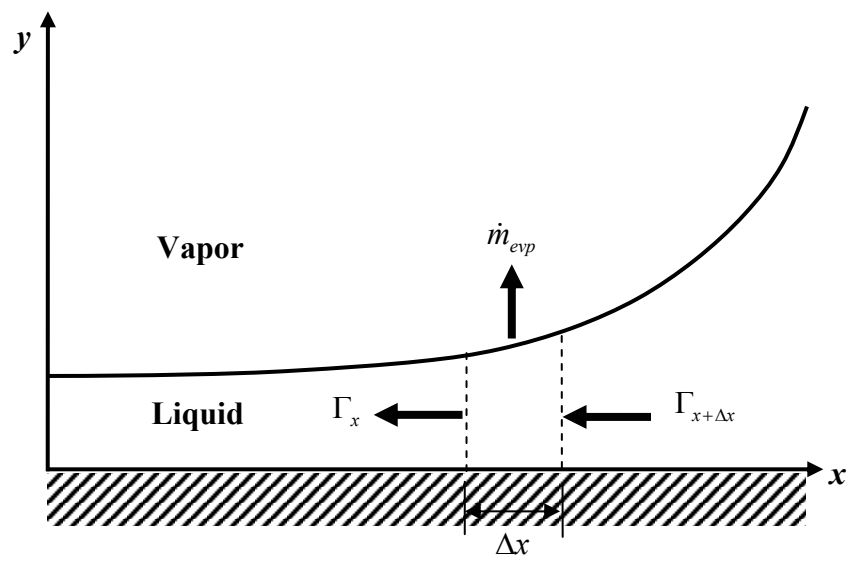


Fig. 3.2. Schematic for describing mass conservation within evaporating thin film.

Using Taylor series expansion for $\Gamma_{x+\Delta x}$, the evaporation mass flux is related to the mass flow rate in the thin film through mass conservation,

$$\frac{d\Gamma}{dx} = -\dot{m}_{evp} \quad (3.23)$$

Finally, substituting Eqs. (3.13) and (3.16) into Eq. (3.23) gives a forth-order, nonlinear, ordinary differential equation for the film thickness. This can be treated as an initial-value problem by specifying the initial conditions at the adsorbed film (at $x = 0$).

3.1.6 Nondimensionalization

The governing equations and boundary conditions are scaled using the following nondimensional variables defined as,

$$\eta = \frac{h}{h_0}, \quad \xi = \frac{x}{x_0} \quad (3.24)$$

$$\Pi_d = \frac{\Pi}{\Pi_0} = \frac{1}{\eta^3} \quad (3.25)$$

$$\dot{m}_{id} = \rho_l u_0 \quad (3.26)$$

$$Ca = \frac{\mu_l u_0}{\sigma_0} \quad (3.27)$$

$$x_0 = \left(\frac{\sigma_0 h_0}{\Pi_0} \right)^{\frac{1}{2}} \quad (3.28)$$

$$\theta = \frac{T_i - T_v}{T_w - T_v} \quad (3.29)$$

$$\kappa = \frac{h_{fg} \dot{m}_{id}}{(k/h_0)} \quad (3.30)$$

$$\Delta T_0 = T_w - T_v \quad (3.31)$$

$$\dot{m}_{id} = C \left(\frac{M}{2\pi RT} \right)^{1/2} \left[\frac{P_v M h_{fg}}{RT_v T_i} (T_i - T_v) \right] \quad (3.32)$$

where, ξ = dimensionless coordinate along the wall,

η = dimensionless coordinate normal to the wall,

h_0 = adsorbed film thickness,

x_0 = axial characteristics length,

Π_d = dimensionless disjoining pressure,

Π_0 = disjoining pressure at adsorbed film,

\dot{m}_{id} = ideal evaporative mass flux,

u_0 = characteristics velocity,

Ca = capillary number,

σ_0 = reference surface tension,

θ = dimensionless temperature,

κ = ratio of evaporative interfacial resistance to conductive resistance,

ΔT_0 = superheat.

The specification of scaling variables is based on the work of Hallinan et al. (1994). The axial coordinate and the film thickness are scaled by different characteristic lengths since the length of transition is one order of magnitude larger than the thickness of thin film for a normal heat input. The film thickness is scaled by the thickness of adsorbed film

which is obtained by setting the evaporation mass flux zero in Eq. (3.16) with the assumption of non-evaporation in the adsorbed film region (Wayner and Schonberg, 1990), and the thickness is given as,

$$h_0 = \left(\frac{V_l T_v A}{M h_{fg} \Delta T_0} \right)^{\frac{1}{3}} \quad (3.33)$$

Equation (3.33) indicates that the thickness of the adsorbed film decreases with increase in the superheat (ΔT_0) which is the temperature differential between the heated wall and vapor phase, and such a trend was observed in previous experimental works. The axial characteristic length is chosen as the length of the transition region by balancing the capillary pressure and disjoining pressure,

$$\sigma_0 \frac{h_0}{x_0^2} = \Pi_0 \quad (3.34)$$

where the subscript '0' represents the value at the reference state of adsorbed film region and then x_0 is obtained. The ideal evaporative mass flux (\dot{m}_{id}) is defined as evaporative mass flux associated with evaporation due to only a temperature jump at the liquid-vapor interface. The characteristic velocity (u_0) comes from the ideal evaporative mass flux. The non-dimensional temperature (θ) is defined as the ratio of the interfacial temperature differential to superheat. Capillary number is defined as the ratio of viscous force to surface tension force.

Using non-dimensional variables and combining with Eqs. (3.12), (3.13), and (3.16), Eq. (3.23) can be expressed in non-dimensional form,

$$-\left[\eta^3\eta_{\xi\xi\xi} - 3\eta^{-1}\eta_{\xi} - A_1\eta^3(\eta_{\xi\xi}\theta)_{\xi} - \frac{3}{2}A_1B_1\eta^2\theta_{\xi}\right]_{\xi} = C_1[\theta - \eta_{\xi\xi} + A_1\theta\eta_{\xi\xi} - \eta^{-3}] \quad (3.35)$$

where,

$$A_1 = \frac{\gamma\Delta T_0}{\sigma_0}, \quad (3.36)$$

$$B_1 = \frac{x_0^2}{h_0^2}, \quad (3.37)$$

$$C_1 = \frac{3Ca}{(\Pi_0 h_0 / \sigma_0)^2}, \quad (3.38)$$

$$\theta = \frac{\Delta T_0 + \kappa(\eta\eta_{\xi\xi} + \eta^{-2})}{\Delta T_0 + \kappa\eta + \kappa A_1\eta\eta_{\xi\xi}}, \quad (3.39)$$

and the subscript ξ represents the derivative with respect to ξ .

Equation (3.35) is a fourth-order, nonlinear, ordinary differential equation for the nondimensional film thickness. The resulting differential equation can be solved iteratively by Gear's method (Gear, 1971), which is a higher-order implicit method and designed to solve stiff nonlinear equations with much larger stability limits.

The procedure of solving Eq. (3.35) is based on the procedure developed uniquely by Chebaro and Hallinan (1993). The fourth-order differential equation needs four initial conditions at the adsorbed region, $x = 0$. For a completely wetting film the slope approaches a very small value at the adsorbed film region; thus first derivative of film thickness is zero. The second and third derivatives of the thickness would be zero as well. But these initial conditions yield the trivial solution of a constant film thickness profile. In order to avoid these trivial solutions, a small perturbation can be applied to the thickness and the slope (Wayner et al., 1976; Hallinan et al., 1994). The solution of Eq.

(3.35) is extremely sensitive to the specification of the initial condition for the second derivative of the thickness especially as the superheat increases. An iterative technique is employed to guess the slope at $x = 0$ such that the solution converges to the appropriate curvature in the bulk meniscus region. Once the liquid film thickness profile $h(x)$ is obtained from Eq. (3.35), the other properties are readily determined since they are all functions of $h(x)$, such as temperature (Eq. (3.21)), pressure gradient (Eq. (3.12)), and the evaporative mass flux (Eq. (3.16)).

Based on the mathematical formulations and numerical treatments stated above, the specific effects such as thermocapillary stress (Section 3.2), slip boundary condition at wall (Section 3.3), binary mixture evaporation (Section 3.4) and liquid polarity (Section 3.5) on the microscale heat and mass transport phenomena within a heated capillary pore, will be extensively discussed in detail in subsequent sections.

3.2 Effect of Thermocapillary Stress

3.2.1 Background

It was found that capillary pumped loop devices have not operated satisfactorily in low gravity, mainly due to deprime of the evaporator (Ku, 1993). In the environment of micro gravity, the buoyancy effect is negligible so that thermocapillary effect is dominant force inducing liquid flow in thermal field.

As discussed in Section 2.3, the thermocapillary stresses degrade the wettability of liquid film with an increase in superheat by pulling the thin film toward the bulk meniscus, which tends to reduce the flow of liquid into the evaporation region.

Thermocapillary stresses become more important as the radius of capillary pore (R), superheat (ΔT_0), and the slope in the relation of surface tension and temperature (γ) increase, and diminish for higher cohesion and adhesion forces (σ and A , respectively) from scaling analysis (Hallinan et al., 1994). In general the thinnest portion of the evaporating meniscus near the adsorbed film is implicitly stable due to the stabilizing effects of solid-liquid adhesive forces. On the other hand, the most likely location for the onset of instability of evaporating meniscus is at the end of the transition region, where the effects of the adhesive forces are no longer dominant relative to surface tension and in addition thermocapillary stresses are also most severe in this region since the interfacial temperature gradients are maximum in the transition region (Pratt et al., 1998).

In this section, based on the numerical model stated in Section 3.1, the impact of thermocapillary effect on microscale heat and mass transfer within heated capillary pore is investigated and the evaporative phenomena is also discussed under various superheat conditions.

3.2.2 Review of Previous Studies

He and Hallinan (1994) developed a mathematical model based on perturbation theory to investigate the effect of the thermocapillary stress on the heat and mass transport associated with evaporation of micro pores. They found that thermocapillary effect influenced significantly the effectiveness of phase-change heat transport. They also found that smaller sized pore was more stable for thermocapillary effect.

Pratt and Hallinan (1995), Pratt et al. (1997) and Pratt and Hallinan (1997) examined experimentally how the flows induced by thermocapillary stresses near the contact line affect the heat transport from the meniscus. They determined the influence of thermocapillary effects near contact line on evaporative heat transfer effectiveness by plotting the Nusselt number versus Marangoni number. The Marangoni number is defined as the ratio of thermocapillary forces to viscous forces. They found that for a small Marangoni number, the heat transfer effectiveness was enhanced with increasing heat input, but at some critical Marangoni number (approximately 4100), the heat transfer coefficient began to decrease, and over than Marangoni number of 10000, the evaporative transport effectiveness became insensitive to Marangoni effects. They concluded that thermocapillary stresses degraded the wettability of the liquid thereby reducing the wicking height and consequently influenced the heat and mass transfer characteristics in the thin film evaporation.

Pratt et al. (1998) conducted both experiments and analysis to identify the thermocapillary effects on the stability of curved menisci within heated capillary pores. They demonstrated experimentally that the instability of an evaporating meniscus was initiated by oscillation in pressure and based on the experimental results the analysis was carried out to determine the conditions causing the meniscus to be unstable. They identified the thermocapillary effect induced the instabilities of the contact line region of evaporating menisci within capillary pores and found that heated meniscus in smaller pores are significantly more stable than in larger pores. Pratt and Kihm (2003) experimentally demonstrated that adding a small amount of second component could

improve the stability of evaporating meniscus by enhancing the wetting of the liquid which was realized by allowing the distillation-driven capillary stress to counteract the thermocapillary stresses.

3.2.3 Results and Discussion

As stated in Section 3.1, the thermocapillary effect are included in momentum equation by considering the gradient of surface tension along liquid-vapor interface in the boundary condition (Eq. (3.9)) and then the contribution of thermocapillary effect is incorporated in mass conservation (Eq. (3.23)). The working fluid is chosen as pentane in two-dimensional slotted pore of 20 μm width. The physical properties are obtained at working temperature of 300 K, and the corresponding vapor was assumed to be saturated. The physical properties of working fluids used in this work are summarized in Table 3.1. Note that $x = 0$ is set to the point of zero evaporation mass flux as the beginning of the transition region in all the presented results.

Figure 3.3 shows meniscus profiles for three superheat conditions. The superheat, represented by the temperature differential between T_w and T_v , is specified by the boundary condition of Eq. (3.19). The length of thin film (transition region) decreases with increasing superheat and the adsorbed film thickness also decreases with an increase in superheat by the action of increasing capillarity and disjoining pressure which occurs naturally to supply more liquid from bulk meniscus to the evaporation region. The trends obtained herein are consistent with the results of Wayner and Schonberg (1990) and Hallinan et al. (1994). As a result of such changes in the film

Table 3.1
Physical properties of water, pentane, decane and ammonia (NIST, 2003)

Physical Properties	Water (at 373K)	Pentane (at 300K)	Decane (at 300K)	Ammonia (at 300K)
ρ_l (kg/m ³)	958	619	726.4	600
μ_l (N·s/m ²)	2.817×10^{-4}	2.144×10^{-4}	9.08×10^{-4}	1.293×10^{-4}
k_l (W/m·K)	0.679	0.111	0.134	0.480
h_{fg} (KJ/kg)	2258	361	348.9	1187
σ (N/m)	$0.1162-1.477 \times 10^{-4} T$	$0.0484-1.102 \times 10^{-4} T$	$0.0508-0.920 \times 10^{-4} T$	$0.0860-2.182 \times 10^{-4} T$

profiles, the steady evaporation can be maintained. In a magnified view of meniscus profile near the adsorbed region as shown in Fig. 3.4 it is clearly demonstrated the thickness of the adsorbed film decreases with increasing superheat.

Figure 3.5 shows the curvature profiles corresponding to the thin film profiles. The profiles indicate that the curvatures approach an asymptotic constant value in the bulk meniscus region and the values are the same for different superheat conditions because the meniscus shape in bulk region is maintained. Experimentally, Welter (1991) observed that for stable evaporating interfacial conditions a variation in the evaporation rate did not noticeably alter the radius of curvature of the meniscus region, which was observed to be equal to the radius of the capillary tube for the perfectly wetting liquids considered in his experiments. His experimental observation was used in the boundary condition for the thin film profiles in the studies of Chebaro and Hallinan (1993). This, the experimental observation is consistent with the curvature profiles in Fig. 3.5. It should be noted that the gradients in the curvature are maximum in the transition region, which accounts for the capillary forces are important contribution to the liquid flow in the transition region. Such a tendency is also found in liquid pressure gradient. In Fig. 3.6 the location of peak liquid pressure gradient roughly corresponds to the location of maximum curvature gradient in Fig. 3.5. The maximum level of the pressure gradient increases with increasing superheat since a higher flow rate directed from the bulk to the thin film region is required to compensate the increased evaporation flux. The evaporative mass flux also has the same trend in Fig. 3.7 which shows the evaporative mass flux distributions calculated from Eq. (3.16) along the thin film for different

superheat levels. The point of maximum evaporation mass flux exists within the thin film region for all superheat levels, and this has been persistently identified in the previous studies. As expected, the evaporative mass flux increases with increasing superheat.

Figure 3.8 shows interfacial temperature profiles calculated from Eq. (3.21) for the same superheat conditions. The temperature differential between the interfacial temperature and vapor temperature leads to the evaporation. In this study, the vapor temperature is 300 K. As shown in Fig. 3.8, the temperature differential is peak at the adsorbed film due to the closeness of the adsorbed film to the heated wall and decreases to minimum at bulk meniscus region due to large conductive resistance of relatively thick liquid film at the bulk region. However, the evaporative mass flux (Fig. 3.7) becomes to maximum at the transition region since the intermolecular force is significant to keep the film from evaporation even though the temperature differential is enough. The temperature profiles indicate that the temperature gradients become to maximum at the transition region. Since thermocapillary stress is caused by the temperature gradient, the thermocapillary stresses are most severe at the transition region and the impact of the thermocapillarity will become more severe in higher heat fluxes. The resulting thermocapillary stresses will degrade the wetting ability of working fluid and then leads to the unstable operation of the devices.

Figure 3.9 shows the distribution of disjoining pressure and capillary pressure. They are calculated from Eq. (3.5), and Eqs. (3.3) and (3.4), respectively, using obtained meniscus profiles. The disjoining pressure, as expected, becomes maximal in the

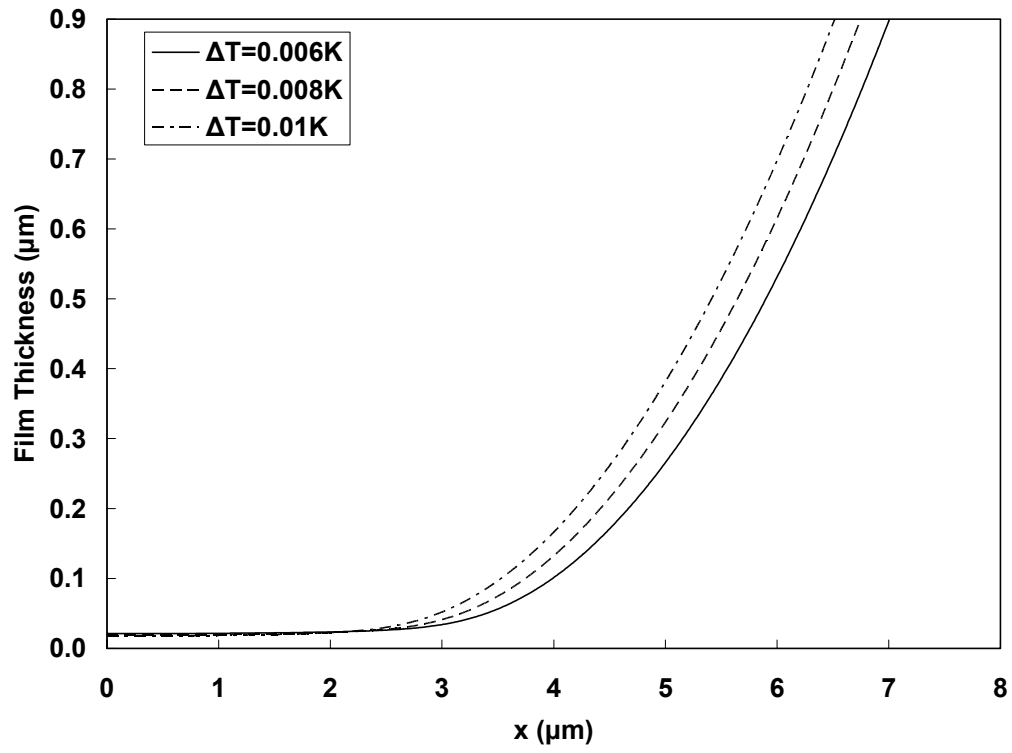


Fig. 3.3. Film thickness profiles for different superheat conditions.

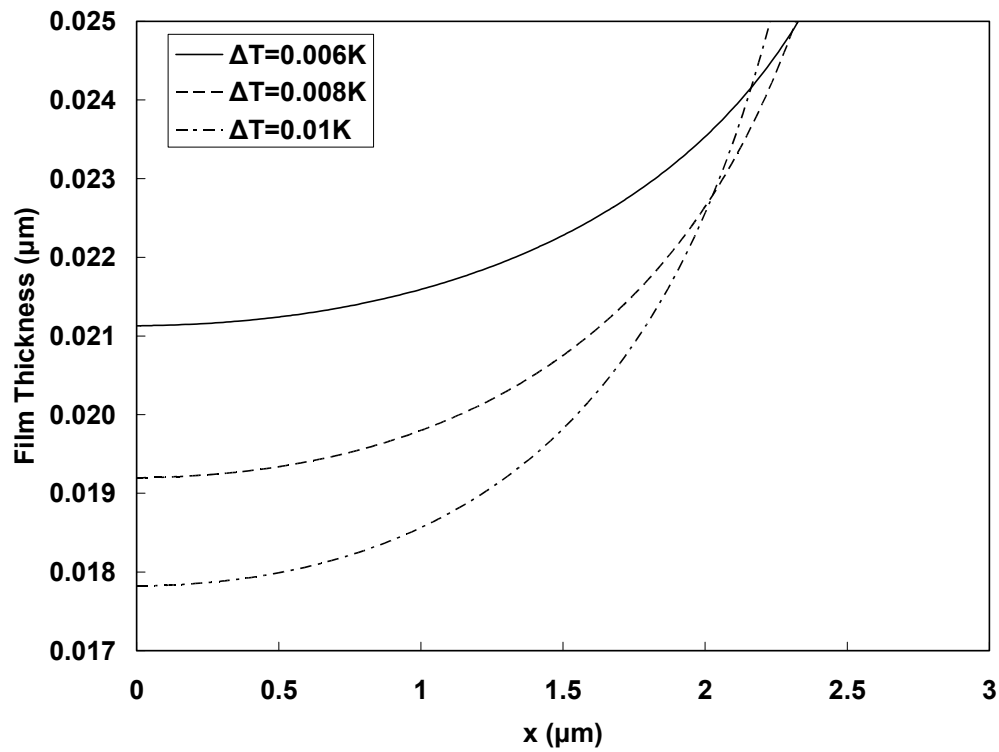


Fig. 3.4. Magnified view of film thickness profile at near adsorbed region for different superheat conditions.

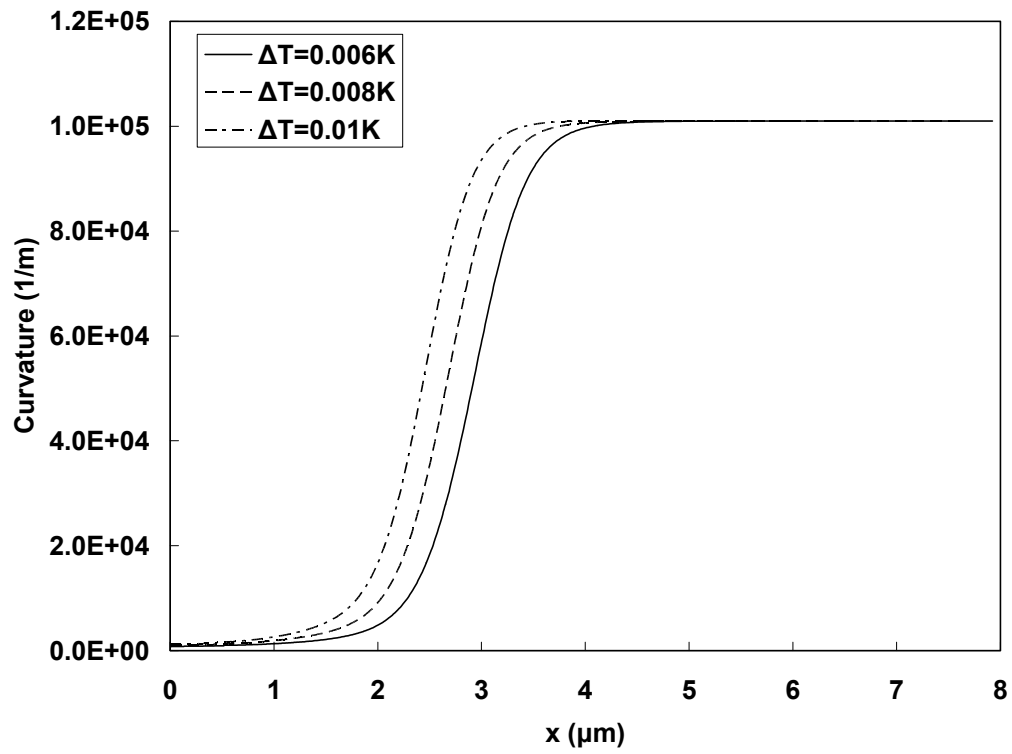


Fig. 3.5. Distribution of curvature for different superheat conditions.

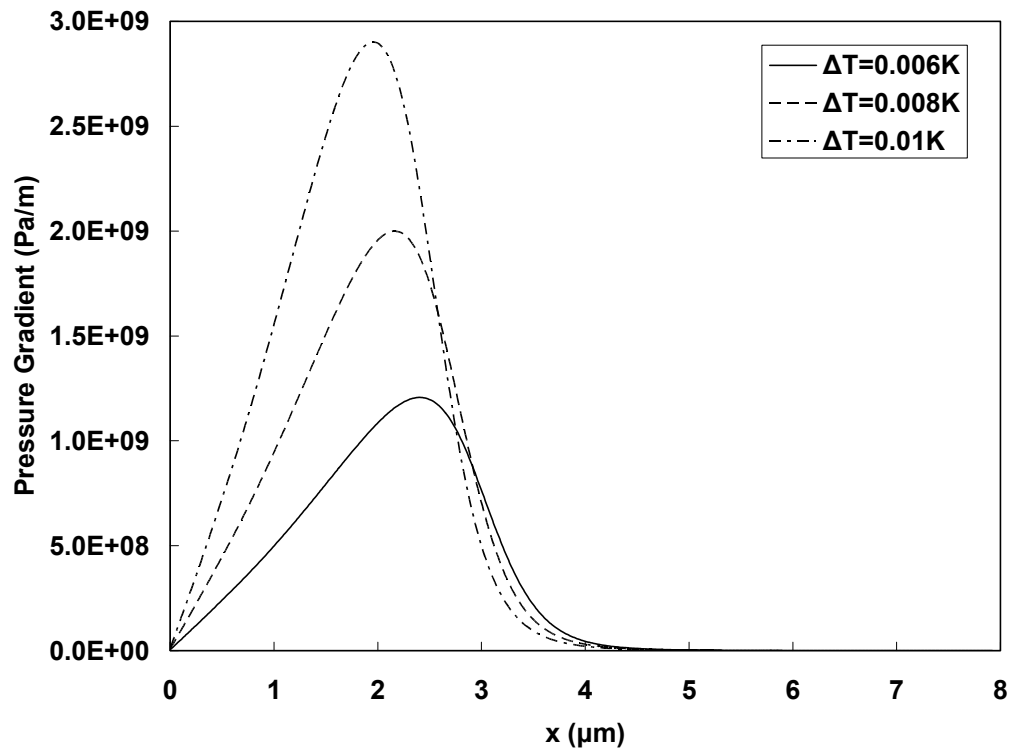


Fig. 3.6. Distribution of liquid pressure gradient for different superheat conditions.

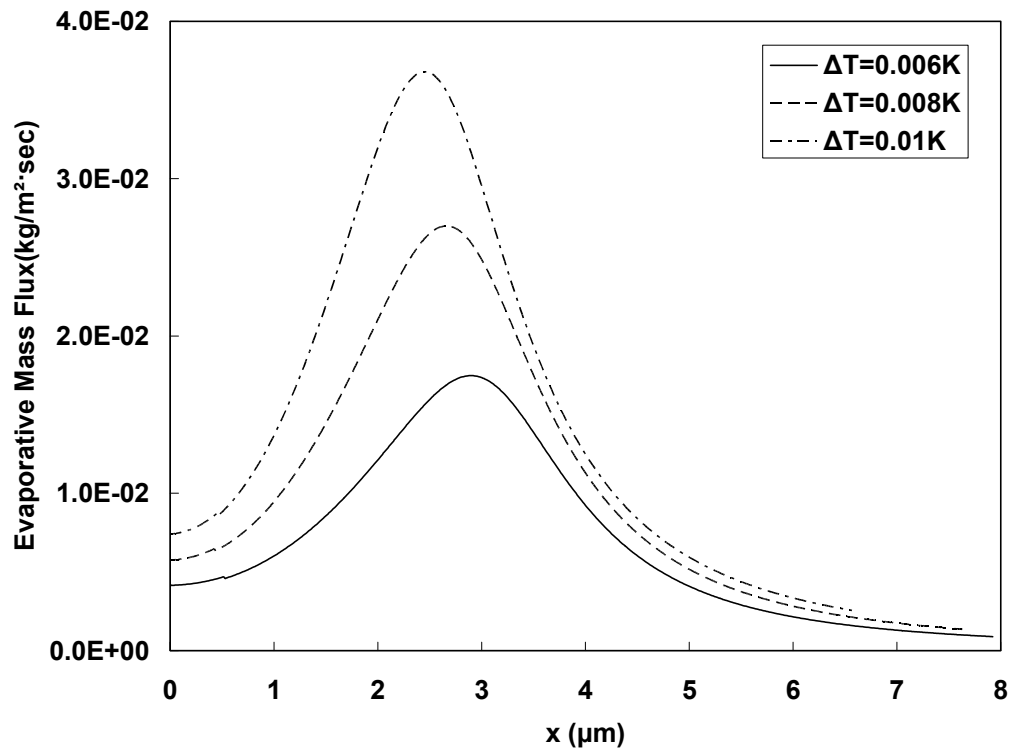


Fig. 3.7. Distribution of evaporative mass flux for different superheat conditions.

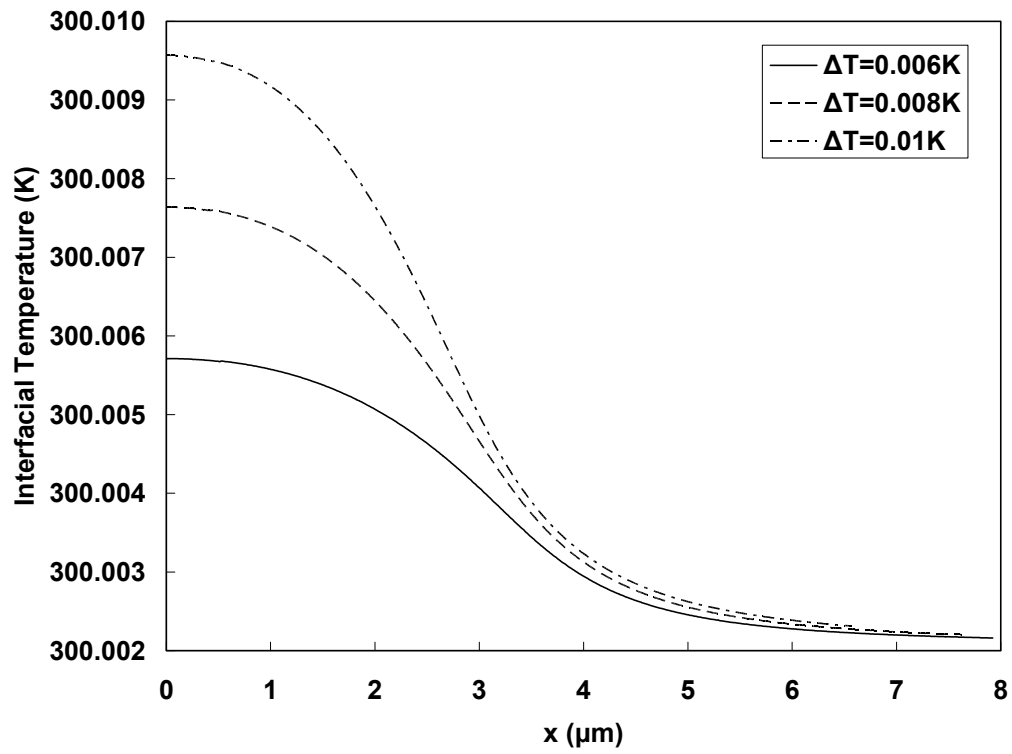


Fig. 3.8. Distribution of interfacial temperature for different superheat conditions.

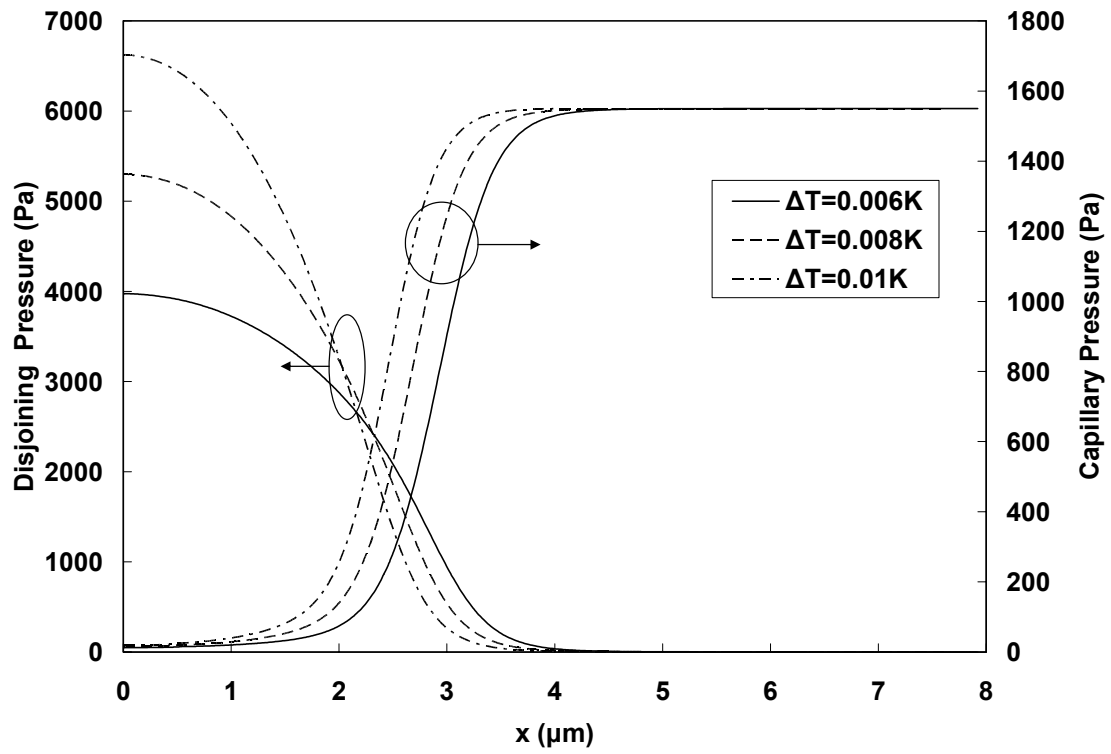


Fig. 3.9. Distribution of disjoining pressure and capillary pressure for different superheat conditions.

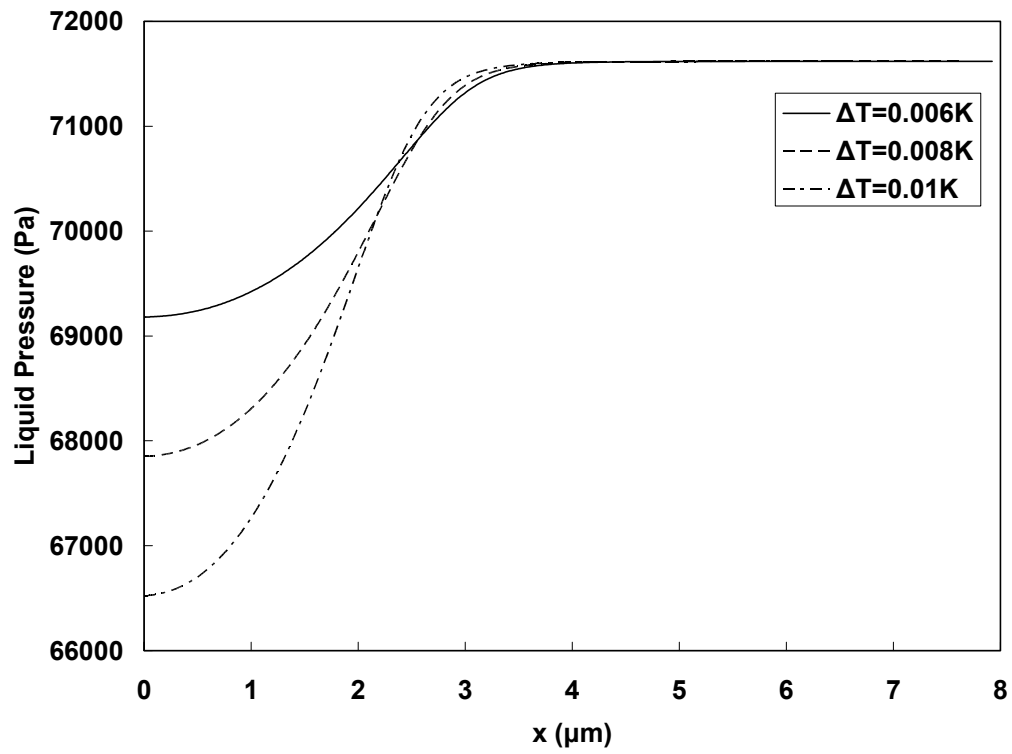


Fig. 3.10. Distribution of liquid pressure for different superheat conditions.

adsorbed film region, in contrast the capillary pressure approach maximum value in bulk region. In practice, the disjoining pressure is negative value and thus this suction the liquid into the transition region. Consequently, the disjoining pressure is potential for replenishing the liquid flow into evaporation region from bulk liquid and thus the disjoining pressure must minimally overcome the thermocapillary stresses and the viscous force applied at solid wall to maintain the steady evaporation. In the transition region, the disjoining pressure and the capillary pressure are equally important. Figure 3.10 depicts the liquid pressure profiles, which demonstrates the pressure drop resulting from a change in meniscus shape increases with increasing superheat to replenish more liquid into the evaporation region.

Figure 3.11 is presented to examine the effect of thermocapillary stress on the thin film profiles for ammonia at the vapor temperature of 300 K. As stated previously, the thermocapillary stress degrades the wettability of the working fluid in the evaporating meniscus (Pratt and Hallinan, 1997), which makes the transition region shorten by pulling the liquid film toward the adsorbed region as shown in Fig. 3.11. The thermocapillary stresses become important in the liquid with increasing the slope (γ) in the diagram of surface tension versus temperature (Hallinan et al., 1994). As indicated in Table 3.1, the slope of ammonia is larger than that pentane, so the changes in the thin film is significant for ammonia.

Figure 3.12 shows the change in the evaporative mass flux profiles due to thermocapillary effect. The peak value of the evaporative mass flux is larger compared to the case of that thermocapillary stress is not considered. However, the integrated

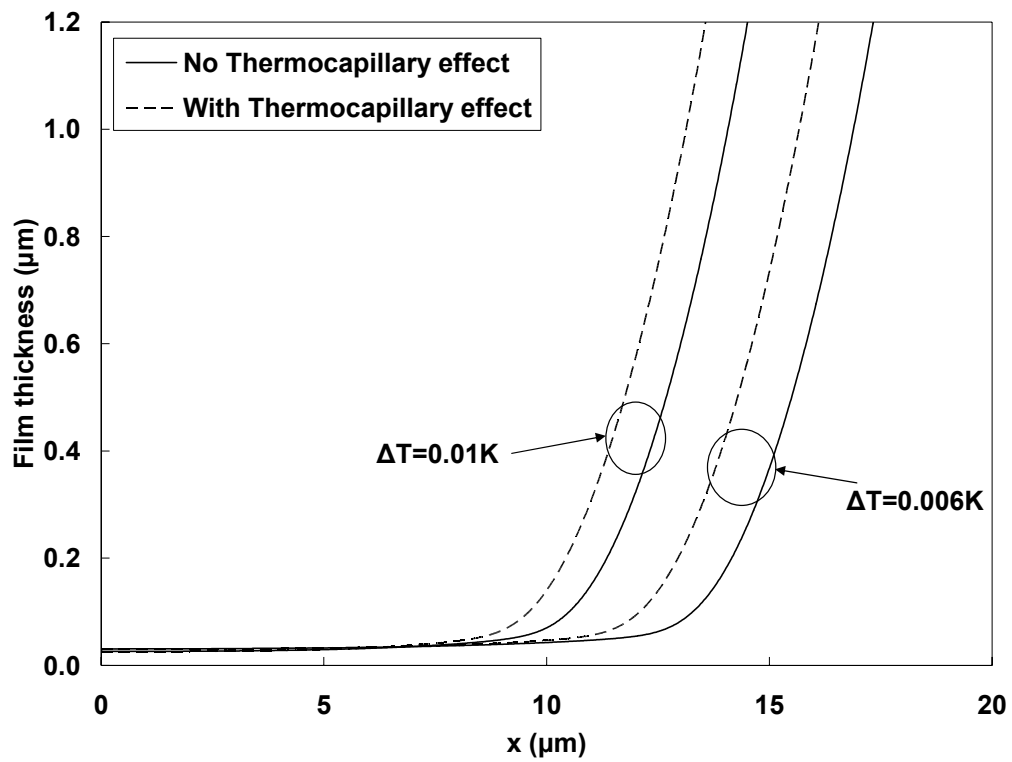


Fig. 3.11. Comparison of thin film profiles with thermocapillary effect and without thermocapillary effect for ammonia at vapor temperature of 300 K.

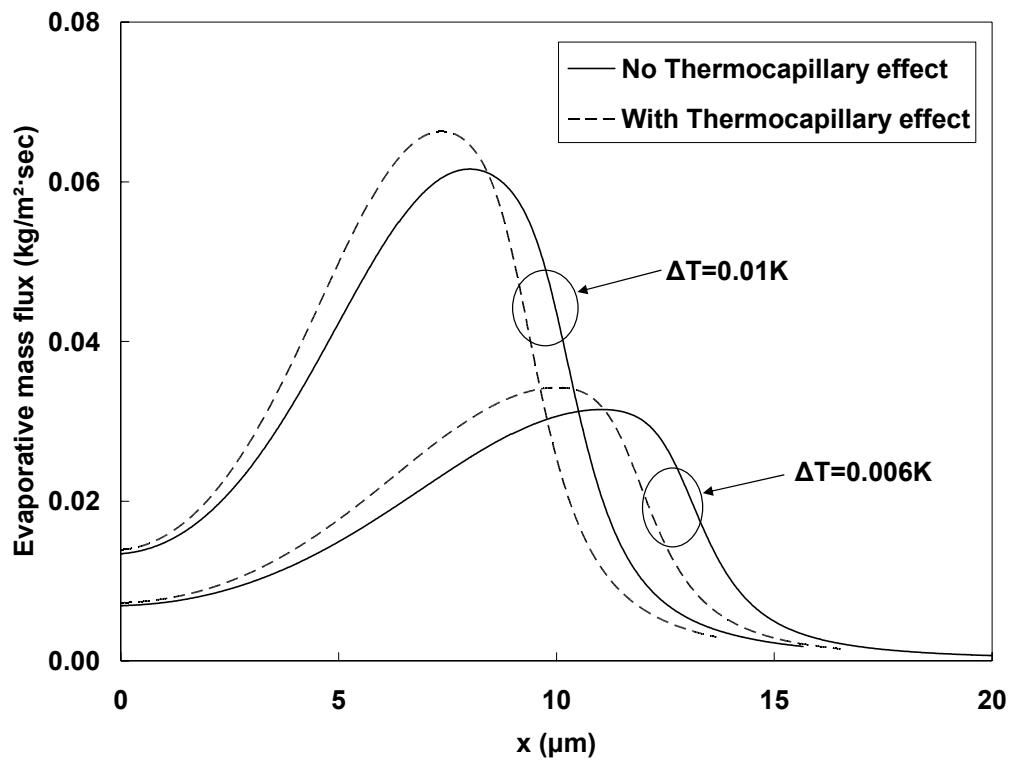


Fig. 3.12. Comparison of evaporative mass flux with thermocapillary effect and without thermocapillary effect for ammonia at vapor temperature of 300 K.

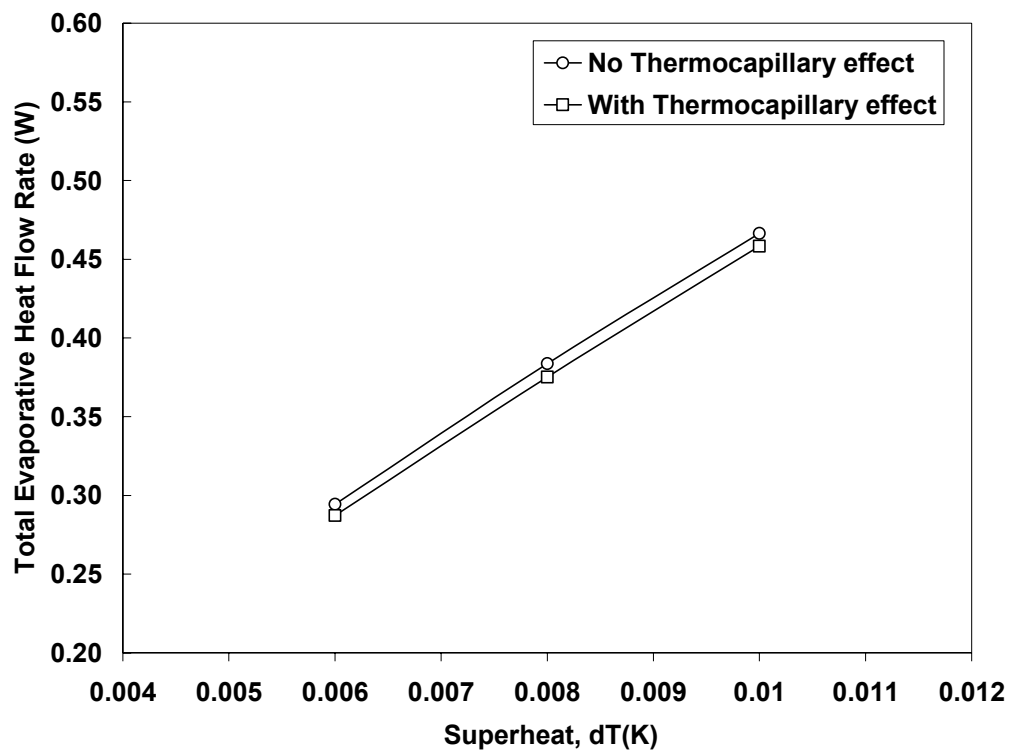


Fig. 3.13. Total evaporative heat flow rate per unit depth for both with thermocapillary effect and without thermocapillary effect at different superheat levels for ammonia.

evaporative mass flow rate decrease due to the thermocapillary stresses since the evaporation region decreased owing to the detrimental effect of thermocapillary stresses, which is confirmed in Fig. 3.13. The figure shows the change in the total evaporative heat flow rates per unit depth that are obtained by the multiplication of the integrated value of evaporative mass flow rate in the transition region and the latent heat of vaporization of ammonia. As expected, the total evaporative heat flow rate increases with increasing the superheat and it clear shows that the thermocapillary stresses degrade the heat transport performance.

3.3 Effect of Slip Boundary Condition at Wall

3.3.1 Background

With the proliferation of MEMS and nano technology, flow phenomena have been studied at smaller scales. At the micro/nano scale, flow cannot be modeled based on a continuum hypothesis. The deviation of the gas flow from the continuum hypothesis is measured by the Knudsen number, which is defined as the ratio of the mean free path to the characteristic length scale. For liquids, however, the concept of the mean free path is not useful so that the Knudsen number cannot be defined. This is one of obstacles to determine the slip effect of liquid flow (Gad-el-Hak, 2001). However, several researchers have recently demonstrated that the no-slip boundary condition may not be applicable to both the micro- and nano-scale liquid flow. Ruckenstein and Dunn (1977) established a model for a slip velocity at the contact line region of a spreading liquid drop on a solid surface. They noted that a gradient of chemical potential along the

interface of liquid and solid induces a force which causes the slip. Neogi and Miller (1982) calculated spreading of an axisymmetric sessile drop over a solid medium using a slip condition which was equal to the slip velocity of Ruckenstein and Dunn (1977). They demonstrated that intermolecular forces in the contact line region had an effect on the surface diffusion of adsorbed molecules which produced slip on a wall substrate. Ruckenstein and Rajora (1983) compared the slip velocity modeled by a chemical potential theory with the slip velocity measured experimentally in a sufficiently small capillary. They determined the slip velocity with the use of the chemical potential theory, where the slip velocity was proportional to a gradient in the chemical potential caused by pressure drop in capillary pore. They demonstrated that the slip velocity was related to the surface diffusion coefficients and the pressure gradient. Recently, Thompson and Troian (1997) provided molecular dynamic (MD) simulations to quantify the slip-flow boundary conditions in liquid flows. Based on the results of MD simulation, they suggested a more general boundary condition for liquid flow at a solid-liquid interface. Choi et al. (2002) examined the slip effects of water flow in hydrophilic and hydrophobic microchannels experimentally. They explained that the effect of slip velocity made the measured flow rate different in two microchannels. In the experimental results they obtained the relation of shear rate and slip length that had the same form as that of Thompson and Troian (1997) with different coefficients. Tretheway and Meinhart (2002) measured the velocity profile in hydrophobic microchannel using micro particle image velocimetry. In their experiments, they measured an apparent slip velocity, which was about 10% of free stream velocity and a slip length was

approximately 1 μm . They concluded that the no-slip condition could be inaccurate for micro scale fluid flow modeling.

While all the above mentioned studies considered only hydrodynamic aspects of slip boundary conditions, the only published study accounting for the evaporation under slip, based on the authors' literature search, is presented by Park et al. (2003). They applied the slip velocity conditions to the evaporating micro channel filled with water under excessively simplified conditions, i.e., assuming isothermal interfacial conditions without incorporating the thermocapillary effects. Nevertheless, they concluded that the slip velocity boundary condition had a significance influence on the fluid and heat transport processes.

The slip boundary condition is related to pressure gradient that gives rise to the flow field of an evaporating meniscus within capillary driven heat transport. Such devices rely upon large pressure gradients in the thin film region to sustain the evaporation. A larger evaporative flow, and therefore thin film pressure gradient, yields an increased slip velocity. Therefore, recently developed thermal control devices having high thermal performance and thus large liquid pressure gradients in thin films can only be accurately modeled by considering a slip velocity condition near the contact line. As the characteristic length of a pore or groove decreases, the slip effects become more important. Further, the slip velocity becomes more important with increase in heat flux in thin film transition region, as will be shown in detail later. According to several experimental investigations, the film thickness in the transition region has been measured to be on the order of tens to hundreds of nanometers (DasGupta et al., 1993a).

Given slip lengths on the order of submicron, slip cannot be ignored when modeling the thermo-fluid characteristics of an evaporating thin film. In this section, the effect of the slip boundary condition on the fluid flow and heat transfer is examined.

3.3.2 Mathematical Model of Slip Boundary Condition

In momentum equation (3.7), the boundary condition for slip motion at wall can be included as follows:

$$u = L_s \left. \frac{du}{dy} \right|_{wall} \quad \text{at } y = 0 \quad (3.40)$$

where L_s is slip length. At a solid wall, the slip velocity is incorporated in velocity field by considering slip length and shear rate at the wall. The slip length is obtained by experimentally and theoretically. The slip boundary condition, Eq. (3.40), is the slip boundary condition at wall, which was proposed by Navier (1823) to incorporate the possibility of flow slip. L_s is the slip length that is an imaginary length from wall at which the velocity extrapolates to zero. If L_s is zero, this is identical to a no-slip condition. Thompson and Troian (1997) proposed the following relation of slip length and shear rate,

$$L_s = L_{s0} (1 - \dot{\gamma} / \dot{\gamma}_c)^{-1/2} \quad (3.41)$$

where L_{s0} is asymptotic limiting value of slip length, $\dot{\gamma}$ is shear rate and $\dot{\gamma}_c$ is the critical value of shear rate. The relation was achieved in the numerical study of a micro Couette flow by the use of molecular dynamics simulations. A similar form of the

relation was obtained experimentally by Choi et al. (2002) in hydrophobic and hydrophilic microchannels with water as shown,

$$L_s = \alpha_1 \dot{\gamma}^{\beta_1} \quad (3.42)$$

where the coefficients, α_1 and β_1 , are experiment dependent. The coefficients obtained in the experiment for hydrophilic microchannel are $\alpha_1 = 0.059$ and $\beta_1 = 0.485$ for water. In this study, using the correlation of Thompson and Troian (1997) the slip effect on microscale heat and mass transfer is investigated for working fluids of pentane and ammonia, and for water the slip model of Choi et al. (2002) is utilized.

The resulting differential equation incorporating slip effect is obtained from Eq. (3.35) given as,

$$\begin{aligned} & - \left[\eta^3 \eta_{\xi\xi\xi} - 3\eta^{-1} \eta_{\xi} - A_1 \eta^3 (\eta_{\xi\xi} \theta)_{\xi} - \frac{3}{2} A_1 B_1 \eta^2 \theta_{\xi} \right]_{\xi} \\ & - \frac{3L_s}{h_0} \left[\eta^2 \eta_{\xi\xi\xi} - 3\eta^{-2} \eta_{\xi} - A_1 \eta^2 (\eta_{\xi\xi} \theta)_{\xi} - A_1 B_1 \eta \theta_{\xi} \right]_{\xi} = C_1 [\theta - \eta_{\xi\xi} + A_1 \theta \eta_{\xi\xi} - \eta^{-3}] \end{aligned} \quad (3.43)$$

where,

$$A_1 = \frac{\gamma \Delta T_0}{\sigma_0}, \quad B_1 = \frac{x_0^2}{h_0^2}, \quad C_1 = \frac{3Ca}{\left(\frac{\Pi_0 h_0}{\sigma_0} \right)^2}, \quad Ca = \frac{\mu_l u_0}{\sigma_0}, \quad \theta = \frac{\Delta T_0 + \kappa (\eta \eta_{\xi\xi} + \eta^{-2})}{\Delta T_0 + \kappa \eta + \kappa A_1 \eta \eta_{\xi\xi}}$$

The differential equation can also be solved numerically using the same iteration method as stated in Section 3.1.

3.3.3 Results and Discussion

The working fluid is pentane at temperature of 300 K. The radius of micro-channel is 10 μm . Thermocapillary stress is also included in mathematical model. The slip length is about 5 nm, which is calculated with thermo-physical properties using the correlation of Thompson and Troian (1998). The results of evaporating liquid film of pentane are compared with those of ammonia.

Figure 3.14 indicates change in thin film profiles due to the slip effect. As stated previously, the thermocapillary stress make the length of transition shorter which in turn induces instability of the evaporation process at specific superheat condition. However, the slip effect compensate for the defect associated with the thermocapillary stress as shown in Fig. 3.14. The slip effect at wall makes liquid of the transition region flow more with smaller flow resistance and then the length of the transition region is increased.

Figure 3.15 shows the distribution of the evaporative mass flux for pentane at different superheat levels, which clearly shows that the evaporative heat flux increase with increasing superheat. In the figure, it should be noted that the slip boundary condition enhances the evaporative mass flux because the flow resistance is reduced due to the slip effect at wall. The trend of the enhancement of the total evaporative heat flow rate per unit depth is shown in Fig. 3.16, which represents the comparisons of total evaporative heat flow rates for slip and no-slip conditions. Also, this figure describes definitely that total evaporative heat flow rates are increased by slip boundary condition. These total evaporative heat flow rates are obtained by multiplying the latent heat of

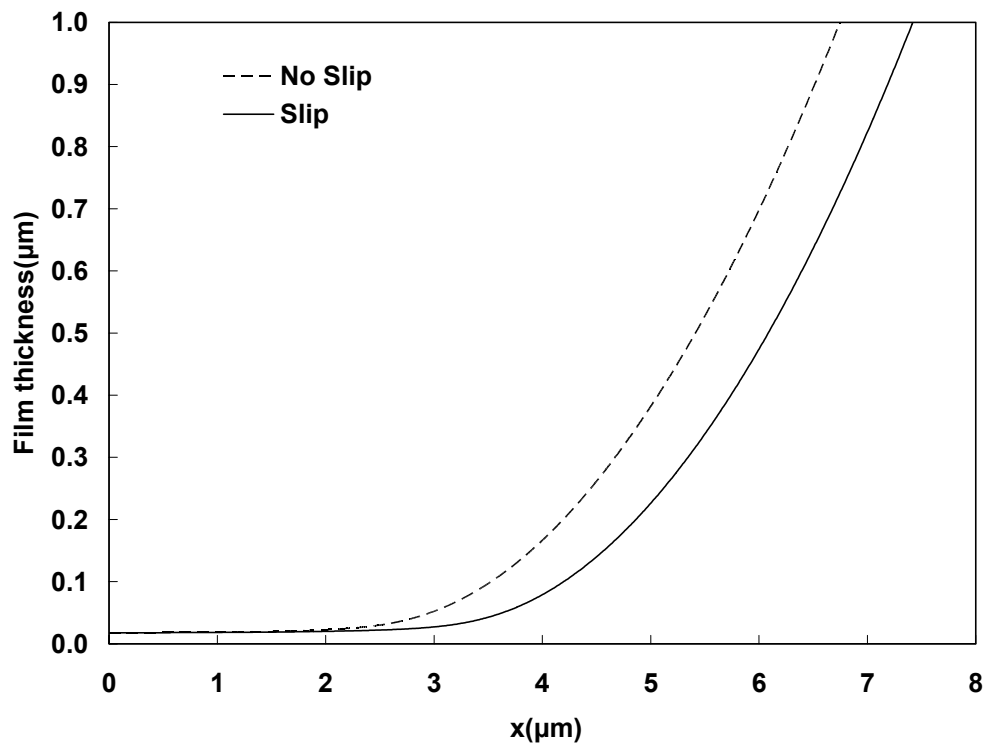


Fig. 3.14. Comparison of meniscus profiles for thermocapillary effect and slip condition for pentane at vapor temperature of 300 K ($\Delta T=0.01\text{K}$).

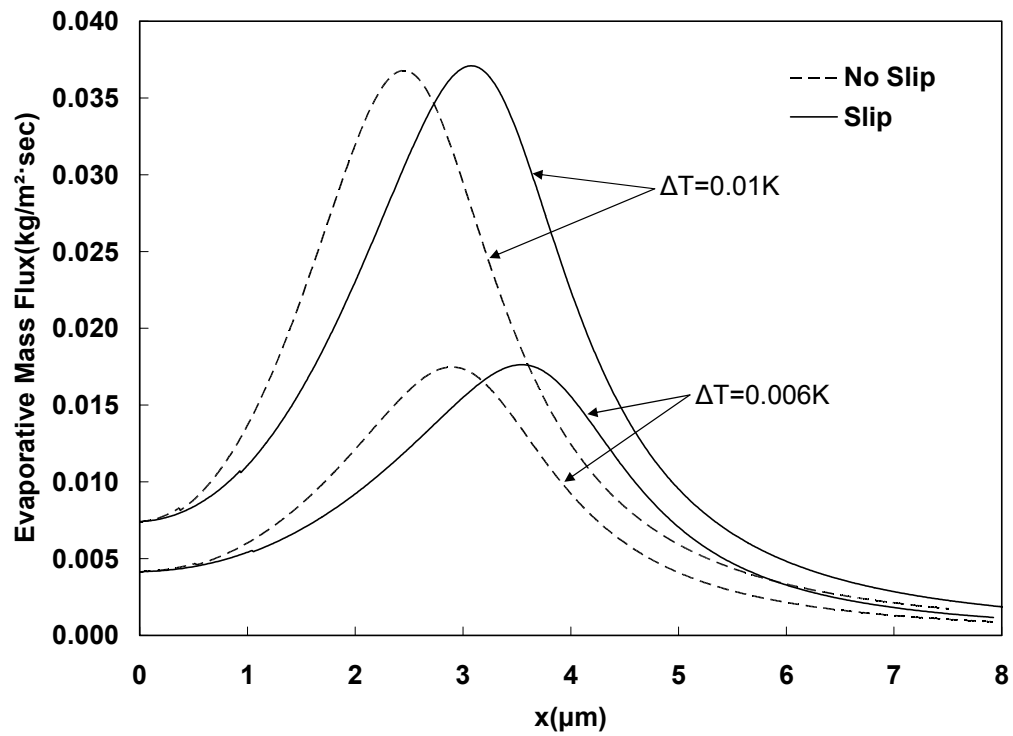


Fig. 3.15. Comparison of evaporative mass fluxes for both slip and no-slip wall conditions at different superheat levels for pentane at vapor temperature of 300K ($\Delta T=0.006K$ and $\Delta T=0.01K$).

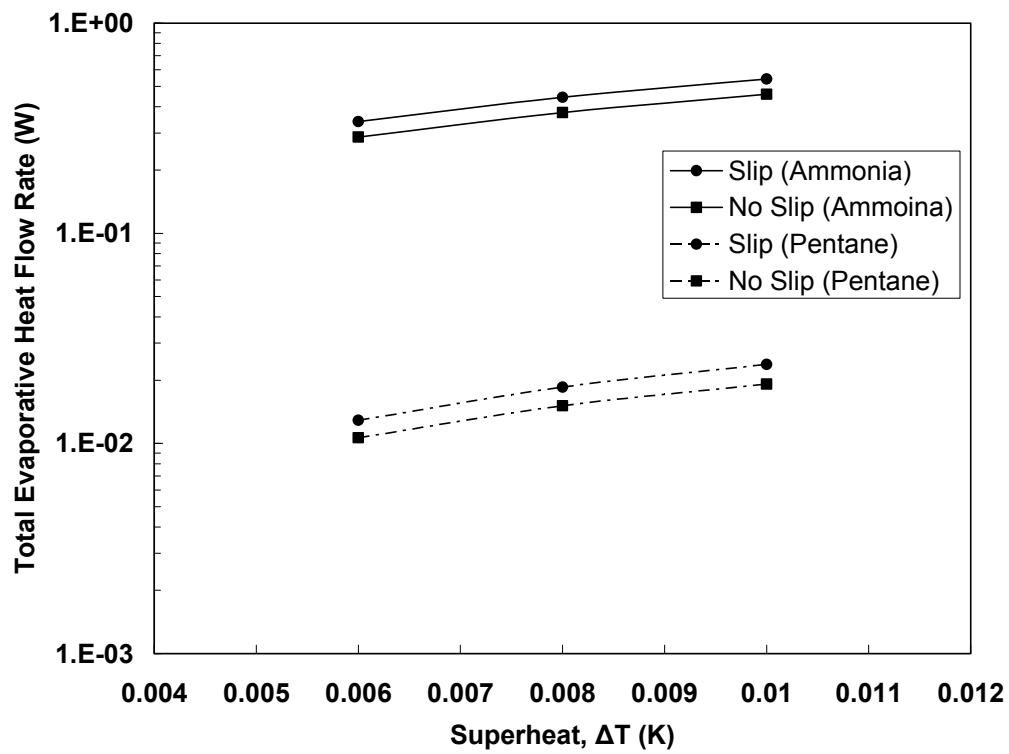


Fig. 3.16. Total evaporative heat flow rate per unit depth for both slip and no-slip wall conditions at different superheat levels for pentane and ammonia.

vaporization by the integrated evaporative mass fluxes in the transition film region. The transition film is defined as the region from the adsorbed film region to the location where capillary pressure becomes larger than or equal to disjoining pressure. In the Fig. 3.16 it should be noted that the total evaporative heat flow rate for ammonia is one order magnitude larger than that of pentane. The dispersion number of ammonia is about ten times larger than that of pentane, which makes longer transition region and then ammonia can evaporate in larger region. In addition, the latent heat of vaporization of ammonia is larger than that of pentane, which is another reason of a larger evaporative heat transfer rate for ammonia than for pentane.

Figure 3.17 represents the liquid pressure gradient distribution along axial axis. It is clear that the liquid pressure gradient increases as superheat increases since liquid flow needs more pressure differential at higher superheat condition. At the same superheat conditions, the flow with slip condition requires relatively smaller pressure gradient since the flow resistance is smaller due to slip effect at wall. The decrease in liquid pressure gradient becomes more significant as superheat increases, which was described in Eq. (3.12). Figure 3.18 shows the distribution of liquid pressure in thin film region. It also confirms that the liquid pressure gradient decreases at slip condition.

To better understanding of the slip effect, a scaling analysis can be used to identify the parameters controlling the slip length and velocity in the evaporating thin film (Hallinan, 2003). First, a characteristic axial velocity, u^* , is defined using the thin film mass flux present at the beginning of the thin film region.

$$u^* = \Gamma_{tr} / \rho_l h_{tr} \quad (3.44)$$

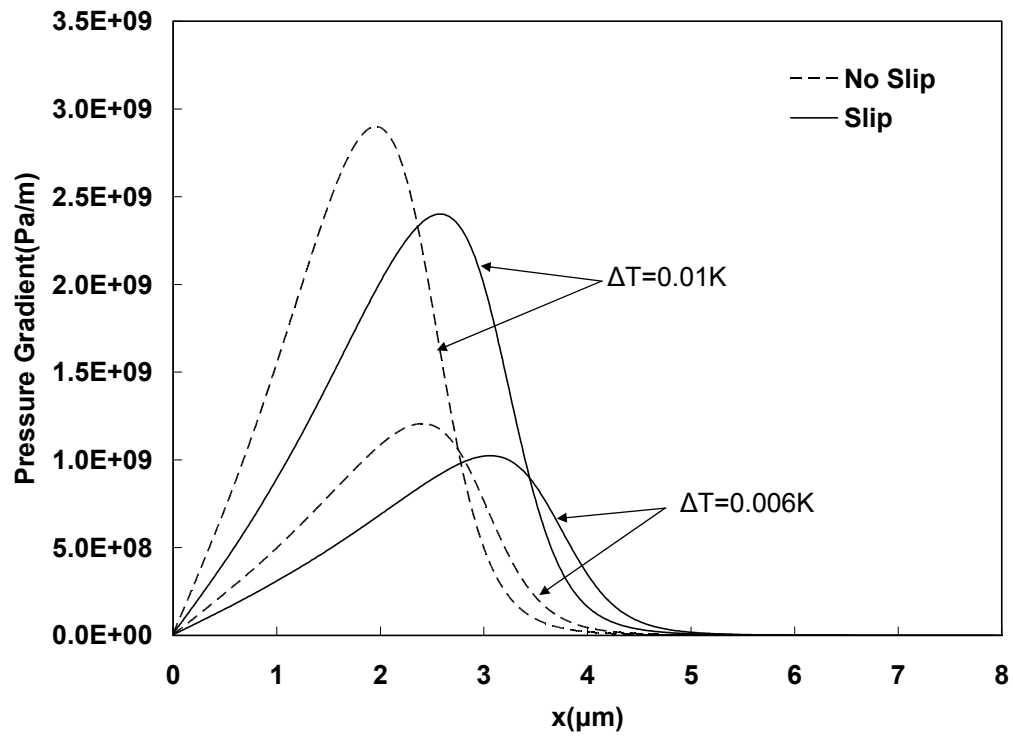


Fig. 3.17. Liquid pressure gradient distribution along axial position at different superheat levels for pentane at vapor temperature 300 K ($\Delta T=0.006\text{K}$ and $\Delta T=0.01\text{K}$).

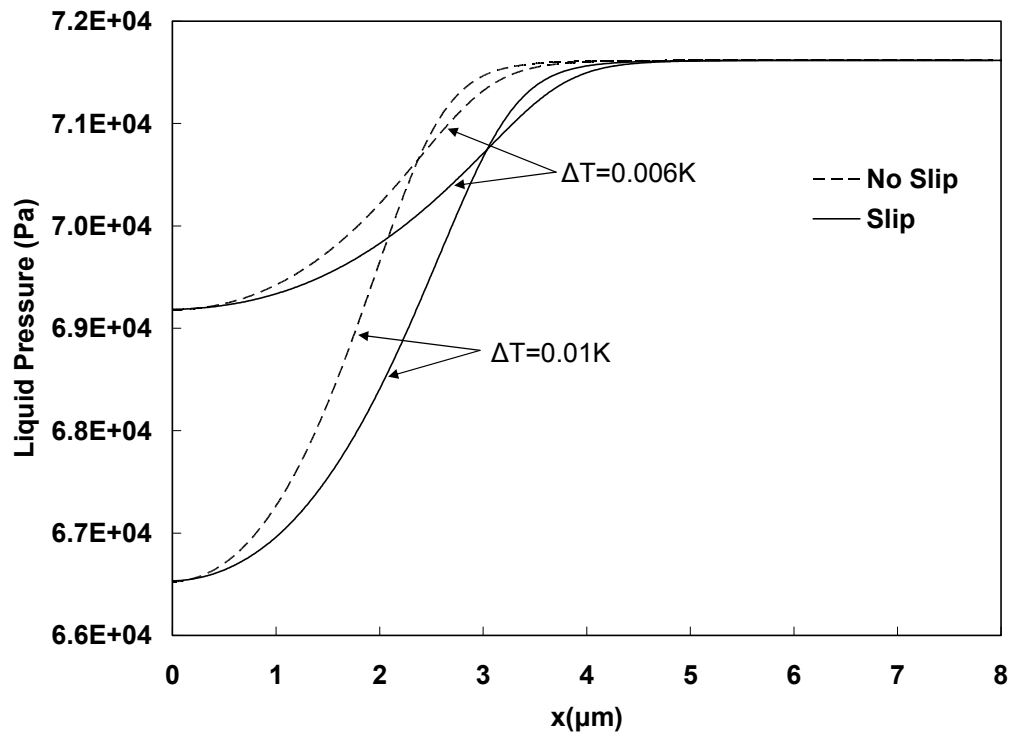


Fig. 3.18. Liquid pressure distribution along axial position at different superheat levels for pentane at vapor temperature of 300 K ($\Delta T=0.006\text{K}$ and $\Delta T=0.01\text{K}$).

where the subscript ‘ tr ’ refers to conditions at the transition between the bulk meniscus and the thin film. The transition mass flux can be related to the total heat transfer from the thin film according to:

$$\Gamma_{tr} h_{fg} \cong k \frac{T_w - T_i}{h_{tr}} \cdot L_{tr} \cong k \frac{T_w - T_v}{h_{tr}} \cdot L_{tr} \quad (3.45)$$

Here L_{tr} is the length of the thin film. The transition film length can be scaled using the lubrication form of the x -momentum equation. Ignoring thermocapillary stresses and scaling derivatives in u by $u^* - u_s$

$$\frac{u^* - u_s}{h_{tr}^2} \cong \frac{\Pi_0 - \Pi_{tr}}{L_{tr}}, \quad (3.46)$$

and Eq. (3.46) is rearranged with respect to L_{tr} ,

$$L_{tr} \cong \frac{(\Pi_0 - \Pi_{tr}) h_{tr}^2}{u^* - u_s} \quad (3.47)$$

Equation (3.47) shows that the transition film length increases as u_s increases and such trend was confirmed in Fig. 3.14. By combining Eqs. (3.45), (3.46) and (3.47), a final scaling for u^* is obtained.

$$u^* (u^* - u_s) \cong \frac{k}{\rho_l h_{fg}} \frac{T_w - T_v}{h_{tr}^2} h_{tr}^2 (\Pi_0 - \Pi_{tr}) \quad (3.48)$$

The slip velocity can be scaled as

$$u_s \cong u^* \left(\frac{L_s}{h_{tr}} \right) \quad (3.49)$$

Thus, the velocity scale, u^* , can be rewritten as

$$u^{*2} \left(1 - \frac{L_s}{h_{tr}} \right) \cong \frac{k}{\rho_l h_{fg}} (T_w - T_v) (\Pi_0 - \Pi_{tr}) \quad (3.50)$$

$$u^* = \left\{ \frac{k}{\rho_l h_{fg}} \frac{(T_w - T_v) (\Pi_0 - \Pi_{tr})}{(1 - L_s/h_{tr})} \right\}^{\frac{1}{2}} \quad (3.51)$$

The total heat transfer from the thin film can then be scaled as:

$$Q \cong \Gamma_{tr} h_{lv} \quad (3.52)$$

$$Q = \left\{ \frac{k}{\rho_l h_{fg}} \frac{(T_w - T_v) (\Pi_0 - \Pi_{tr})}{(1 - L_s/h_{tr})} \right\}^{\frac{1}{2}} \rho_l h_{fg} h_{tr} \quad (3.53)$$

Equation (3.53) describes that for a given superheat condition, $(T_w - T_v)$, and therefore a given $(\Pi_0 - \Pi_{tr})$, a larger slip length yields an increased heat transport. This result was also confirmed in Fig. 3.16.

3.4 Binary Mixture Evaporation

3.4.1 Background

In 1855, Thomson defined tears of wine phenomena which take place in wine glass. As known typically, alcohol evaporates earlier than water since alcohol is more volatile than water. As examined in previous sections, most of the evaporation takes place in the thin film region. Therefore, the concentration of water in thin film region is relatively denser than that in bulk region and thus the surface tension in thin film region is larger relative to that of bulk region because the surface tension of water is larger than that of alcohol. As a result, such a concentration gradient due to the preferential evaporation gives rise to surface tension gradient in the liquid film and then it causes the

liquid flow from bulk region to thin film region. This resulting surface tension makes the liquid climb up along the glass wall until forming drops, and then the drops roll down due to gravity. It repeats a cycle of climbing up and rolling back. It was defined the tears-of-wine phenomena by Thomson (1855). From this interesting phenomenon it should be noted that the direction of the effective surface tension caused by the binary mixture evaporation is opposite to the thermocapillary stress.

It has been noted experimentally or theoretically that for large heat flux, unstable oscillatory operations of the phase change devices have been observed. Such instability is identified to be caused by thermocapillary stresses along liquid-vapor interface resulting from temperature gradient that may degrade the wettability of the liquid within the phase-change heat transport devices, which subsequently leads to the reduction in the performance of the devices by diminishing the ability of the capillary pumping potentials. It is also found that the thermocapillary stresses become severe as the superheating due to heat flux increases. One available way to compensate the thermocapillary stresses has been proposed to introduce a small amount of second component having relatively large surface tension and lower vapor pressure so that the second component evaporates later than the main component. Typically, the interfacial temperature increases in the direction of fluid flow towards the transition film region as stated previously. Since the surface tension is reversely proportional to the temperature, the surface shear stress gradient caused by the temperature gradient in the transition region would hinder fluid flow toward the transition film region. On the other hand, the concentration of the second component of the mixture with higher surface tension and lower vapor pressure

can reverse the direction of flow. Therefore, a surface tension gradient due to a concentration gradient in the mixture may enhance flow toward the transition region. This is called a distillation-driven capillary stress (Pratt and Kihm, 2003).

It has been noted experimentally that since the thin film region is extremely thin, even a very small amount of a second component in the bulk meniscus region of the system can significantly affect the evaporation process in the thin film region. Although some research has been done on this very broad topic, these effects have not been sufficiently studied since the transport processes are more complex relative to those of a single fluid (Wayner, 1999).

In this section, based on the constant vapor pressure model developed by Parks and Wayner (1987a), a mathematical formulation of Hallinan et al. (1994) as depicted in Section 3.1 is extended to investigate the impact of binary mixture evaporation on the microscale heat and mass transport within evaporating thin film. The model also examines the change in surface stress field of the transition film region arising from a composition change due to preferential evaporation and explains experimentally observed enhancement in stability of binary mixture of Pratt and Kihm (2003). The composition gradient of the binary mixture is determined by the use of a binary mixture model developed by Parks and Wayner (1987a).

3.4.2 Review of Previous Studies

Experimentally phase change device showed an unstable behavior in the condition of higher heat input. In order to improve this unstable operation of phase

change device, two-component heat pipe was developed by Tien (1970). He investigated the operational characteristics of two-component heat pipes and found that two-component heat pipe improved the stability in the operation of the heat pipe.

Tung et al. (1982) and Wayner et al. (1985) conducted the experimental study of an evaporating thin liquid film formed on a heated inclined flat substrate immersed in a liquid pool of a mixture of decane and tetradecane. They found that composition gradient of the mixture in the contact line region has a significant effect on the thin film profile relative to a single fluid of decane. They noted that the addition of even a small percentage of second component significantly influences the transport processes in the contact line region of an evaporation thin film. The experimental results were analytically examined using a Marangoni flow model by Tung and Wayner (1984). The analysis demonstrated that surface shear resulting from both thermocapillarity and a concentration gradient has a significant impact on a multicomponent evaporating system even when the concentration of the second component is small in the bulk fluid.

Wayner et al. (1985) measured the evaporating extended meniscus profiles of binary mixture under varying heat flux using laser interference technique and compared those with the profiles of pure system. They found that the profiles for the mixtures were spread out relative to those for the pure system. It was noted that the evaporative heat transfer characteristics of the contact line region could be significantly altered by the addition of a small percentage of a second component and the proper use of this additional variable in devices that was dependent upon evaporation from a stationary thin film should lead to improved control and enhanced performance.

Parks and Wayner (1985) proposed constant vapor boundary condition to make the equation simplified and calculated the film thickness, temperature and concentration profiles over a small length of an evaporating binary mixture based on the results obtained in the experiment of Tung et al. (1982). They noted that the surface tension gradient and curvature gradient were significant contribution to the mass flow rate of the evaporating meniscus.

Volintine and Wayner (1986) made a model to examine the fluid flow in an ultra-thin film with isothermal interfacial condition by assuming that surface tension gradients and disjoining pressure gradients control the flow. They showed that the reduction of vapor pressure due to the liquid-solid interactions could be estimated from a modified form of the Kelvin relation.

Parks and Wayner (1987a; 1987b) developed the numerical model for binary evaporating near contact line region. Combining a constant vapor pressure boundary condition at the liquid-vapor interface with the meniscus profiles from experiments by Tung et al. (1982), they numerically obtained profiles of other physical properties such as concentration and temperature in evaporating meniscus using thermo-physical relations with the profile. The experimental profiles were fitted to polynomials in a least square sense. They demonstrated that the major contribution to the mass flow rate in the meniscus was surface tension gradients due to gradients in temperature and concentration. In the analysis, it was noted that a surface tension gradient caused by a concentration gradient was more dominant than by a temperature gradient.

Recently, Pratt and Kihm (2003) experimentally investigated the thermocapillary effects on a heated evaporating meniscus formed by binary mixtures of pentane and decane by measuring the wicking height of binary mixture in capillary pores. Their results demonstrated that interfacial thermocapillary stresses resulting from liquid-vapor interfacial temperature gradients, which have been known to degrade the wettability of the liquid, could be counteracted by concentration gradients associated with preferential evaporation in binary mixture. They found that the optimum concentration of the binary mixture significantly prolonged instability onset compared to the pure liquid. They also demonstrated that there was no degrading effect of the binary mixture on heat transport by applying a simple energy balance.

Kern and Stephan (2003a) developed a theoretical model for the effect of binary mixture evaporation on nucleate boiling heat transfer using a single bubble model. Their model included interfacial curvature, adhesive pressure, interfacial thermal resistance, Marangoni convection, and the local variation of composition. They described the heat and mass transfer in thin liquid film and combined it with the macroscopic solution for the liquid and solid domain. Comparison of the heat transfer coefficient of binary mixture with measurements from experiments showed a good agreement. They also examined that the heat transfer in the thin film had a strong influence on overall heat flow. Based on their theoretical model, Kern and Stephan (2003b) investigated the decisive mixture effects caused by concentration gradients in nucleate boiling of binary mixture. Their results showed that diffusive mass transfer and Marangoni convection had an almost insignificant influence on heat and mass transfer in the nucleate boiling

process. They also found that for binary mixture evaporation the maximum heat flux was reduced and the length of the thin film became longer relative to the evaporation of a pure liquid flow.

3.4.3 Mathematical Model of Binary Mixture Evaporation

As stated in Section 3.1, the fluid mechanics in the thin film regions are described by momentum equation,

$$\mu_l \frac{\partial^2 u}{\partial y^2} = \frac{dP_l}{dx} \quad (3.54)$$

and two boundary conditions are as follows:

$$u = 0 \quad \text{at } y = 0 \quad (3.55)$$

$$\mu \frac{du}{dy} = \frac{d\sigma}{dx} \quad \text{at } y = h(x). \quad (3.56)$$

The second boundary condition has a significant effect on the velocity distribution of binary mixture because of large gradients in concentration and temperature during evaporation, and thus the surface tension.

The necessary liquid flow in an evaporating thin liquid film is provided by the liquid pressure gradient, which is determined by differentiation of augmented Laplace-Young equation (Eq. (3.2)) with respect to x ,

$$\frac{dP_l}{dx} = -\sigma \frac{dK}{dx} - K \frac{d\sigma}{dx} - \frac{d\Pi}{dx} \quad (3.57)$$

For binary mixture, the gradient of surface tension consists of gradients of temperature and composition as follows:

$$\frac{dP_l}{dx} = -\sigma \frac{dK}{dx} - K \frac{\partial \sigma}{\partial c} \frac{dc}{dx} - K \frac{\partial \sigma}{\partial T} \frac{dT}{dx} - \frac{d\Pi}{dx} \quad (3.58)$$

where c is composition. Second term in R.H.S. of Eq. (3.58) is the effect of composition gradient and third term is for thermocapillary effect. Therefore, for an evaporation of binary mixture, the liquid flow is induced by combined effects of curvature, surface tension, composition, temperature and disjoining pressure. Especially, the composition gradient should overcome the temperature gradient to get the benefit of stabilizing ability of binary mixture. In general, the disjoining pressure in films of mixtures is a complicated function of composition, but in the case of mixtures of similar components such as two alkanes, the dielectric and optical properties of the components may be sufficiently close such that the molecular component of the disjoining pressure can be assumed independent of the composition (Volintine and Wayner, 1986).

For a binary mixture of low molecular weight alkanes, the surface tension can be represented by Reid et al. (1977),

$$\sigma = c_1 \sigma_1 + (1 - c_1) \sigma_2. \quad (3.59)$$

In this model a mixture of pentane and decane is considered. Subscript '1' and '2' represent pentane and decane, respectively, and c_1 is a mole fraction of pentane mixed in mixture and thus the maximum value of c_1 is one. In this work, a variety of mole fractions are taken into consideration to examine the effect of the mole fraction on the evaporation efficiency and the stability. Alkanes are one of the hydrocarbon families that have only carbons. Each carbon atom in the molecule is surrounded by single co-valent bonds. As a result, they are non-polar molecules since all of the C-H bond dipoles cancel

each other. The general molecular formula for the members of the alkane family is:



where n is number of carbon atoms in the alkane molecule. Pentane (C_5H_{12}) and decane ($C_{10}H_{22}$) belong to the alkane family (Logan, 1997).

By the chain rule the following equation of surface tension gradient is achieved.

$$\frac{d\sigma}{dx} = \left[c_1 \frac{d\sigma_1}{dT} + (1-c_1) \frac{d\sigma_2}{dT} \right] \frac{dT_i}{dx} + (\sigma_1 - \sigma_2) \frac{dc_1}{dx} \quad (3.61)$$

The surface tensions of the pure components are assumed to be linear functions of temperature given as,

$$\sigma_1(T_i) = \sigma_{10} - \gamma_1(T_i - T_v) \quad (3.62)$$

$$\sigma_2(T_i) = \sigma_{20} - \gamma_2(T_i - T_v) \quad (3.63)$$

where the reference surface tension σ_{01} and σ_{02} are for pentane and decane at vapor temperature T_v , respectively and γ_1 and γ_2 are the slope of surface tension, which are given by Reyes and Wayner (1997). Equation (3.59) is rearranged using the linear function of surface tension,

$$\sigma = c_1(\sigma_{10} - \gamma_1(T_i - T_v)) + (1-c_1)(\sigma_{20} - \gamma_2(T_i - T_v)) \quad (3.64)$$

Therefore, Eq. (3.61) can be rearranged using above relation,

$$\frac{d\sigma}{dx} = [-(\gamma_1 - \gamma_2)c_1 - \gamma_2] \frac{dT_i}{dx} + [\sigma_{10} - \sigma_{20} - (\gamma_1 - \gamma_2)(T_i - T_v)] \frac{dc_1}{dx} \quad (3.65)$$

The concentration gradient can be related to the temperature gradient at the liquid-vapor interface through the use of a constant vapor pressure boundary condition (Parks and Wayner, 1985).

$$P_{v_i} = c_i P_{v_i}^{sat}(T) \quad (3.66)$$

where $P_{v_i}^{sat}(T)$ is saturation pressure of component i at temperature T . The vapor pressure of pure components are calculated from the Antoine equation,

$$\ln P_{v_i}^{sat} = A_i + \frac{B_i}{T + C_i} \quad (3.67)$$

where the constants (A_i , B_i , C_i) for common liquids are given by Reyes and Wayner(1997).

When two liquids are mixed, the equivalent vapor pressure of the mixture roughly follows Raoult's law (Logan, 1997), which states that vapor pressure of the mixture is a function of the vapor pressures of the individual components and their mole fraction:

$$P_v = P_{v_1} + P_{v_2} = c_1 P_{v_1}^{sat}(T_i) + (1 - c_1) P_{v_2}^{sat}(T_i) \quad (3.68)$$

where $P_{v_1}^{sat}$ and $P_{v_2}^{sat}$ are the saturation vapor pressure of component 1 and 2, respectively.

Differentiating above equation with respect to x and setting the result equal to zero yields the following equation since it is assumed that total vapor pressure is constant.

$$\left(1 - \frac{P_{v_2}^{sat}}{P_{v_1}^{sat}}\right) \frac{dc_1}{dx} + \left\{c_1 \frac{d \ln P_{v_1}^{sat}}{dT} + (1 - c_1) \frac{P_{v_2}^{sat}}{P_{v_1}^{sat}} \frac{d \ln P_{v_2}^{sat}}{dT}\right\} \frac{dT_i}{dx} = 0 \quad (3.69)$$

where,

$$\frac{d \ln P_{v_1}^{sat}}{dT} = -\frac{B_1}{(T + C_1)^2} \quad (3.70)$$

$$\frac{d \ln P_{v_2}^{sat}}{dT} = -\frac{B_2}{(T + C_2)^2} \quad (3.71)$$

Therefore, the derivative of concentration is rearranged,

$$\frac{dc_1}{dx} = \frac{P_{v_1}^{sat}}{P_{v_1}^{sat} - P_{v_2}^{sat}} \left\{ c_1 \frac{B_1}{(T + C_1)^2} + (1 - c_1) \frac{P_{v_2}^{sat}}{P_{v_1}^{sat}} \frac{B_2}{(T + C_2)^2} \right\} \frac{dT_i}{dx} \quad (3.72)$$

Equations (3.65) and (3.72) can be combined to give the surface tension gradient in terms of the temperature gradient alone.

$$\frac{d\sigma}{dx} = \left[\begin{array}{l} \left\{ \sigma_{10} - \sigma_{20} - (\gamma_1 - \gamma_2)(T_i - T_v) \right\} \frac{P_{v_1}^{sat}}{P_{v_1}^{sat} - P_{v_2}^{sat}} \left\{ \frac{c_1 B_1}{(T + C_1)^2} + \frac{P_{v_2}^{sat}}{P_{v_1}^{sat}} \frac{(1 - c_1) B_2}{(T + C_2)^2} \right\} \\ -(\gamma_1 - \gamma_2)c_1 - \gamma_2 \end{array} \right] \frac{dT_i}{dx} \quad (3.73)$$

As stated in Section 3.1, the gradient of surface tension is substituted into the pressure gradient (Eq. (3.58)) and then the surface tension gradient makes a contribution to the mass flow rate in Eq. (3.56).

This model assumes that the concentration is uniform across the film at any x location and therefore diffusion in the y direction has not been included. There would be diffusion in the x direction due to the concentration gradients in the x direction, but this effect is secondary to the bulk convection term and thus has been neglected for simplification of the mathematical formulation.

$$\begin{aligned} & \left[\begin{array}{l} -F_1 \eta^3 (\eta_{\xi\xi} \theta c_1)_\xi - (F_2 - 1) c_1 \eta_{\xi\xi\xi} \eta^3 - F_2 (\eta_{\xi\xi} \theta)_\xi \eta^3 - (F_3 - 1) \eta_{\xi\xi} \eta^3 c_{1\xi} \\ + F_3 \eta_{\xi\xi\xi} \eta^3 - 3\eta^{-1} \eta_\xi + F_4 \eta^2 \left\{ (1 - F_3) c_{1\xi} - F_1 (c_1 \theta)_\xi - F_2 \theta_\xi \right\} \end{array} \right]_\xi \\ & = C_1 \left[\theta - ((1 - F_3) c_1 + F_3) \eta_{\xi\xi} + (F_1 c_1 + F_2) \theta \eta_{\xi\xi} - \eta^{-3} \right] \end{aligned} \quad (3.74)$$

where the coefficients are as follows:

$$F_1 = \frac{(\gamma_1 - \gamma_2)}{\sigma_{01}} \Delta T \quad (3.75)$$

$$F_2 = \frac{\gamma_2 \Delta T}{\sigma_{01}} \quad (3.76)$$

$$F_3 = \frac{\sigma_{02}}{\sigma_{01}} \quad (3.77)$$

$$F_4 = \frac{1.5x_0^2}{h_0^2} \quad (3.78)$$

$$C_1 = \frac{3v_1 x_0^2}{h_0^3 \Pi_0} \dot{m}_{id} \quad (3.79)$$

$$\theta = \frac{\Delta T_0 + \kappa \{((1 - F_3)c_1 + F_3)\eta\eta_{\xi\xi} + \eta^{-2}\}}{\Delta T_0 + \kappa\eta + \kappa(F_1 c_1 + F_2)\eta\eta_{\xi\xi}} \quad (3.80)$$

from (3.72)

$$c_{1\xi} = \frac{P_{v_1}^{sat}}{P_{v_1}^{sat} - P_{v_2}^{sat}} \left\{ c_1 \frac{B_1}{(\theta\Delta T + T_v + C_1)^2} + (1 - c_1) \frac{P_{v_2}^{sat}}{P_{v_1}^{sat}} \frac{B_2}{(\theta\Delta T + T_v + C_2)^2} \right\} \Delta T \theta_{\xi} \quad (3.81)$$

Differential equation (3.74) for thin film shape and Eq. (3.81) for concentration are solved simultaneously. For the numerical scheme for solving the differential equations, the Gear's implicit algorithm is also used herein.

3.4.4 Results and Discussion

A mixture of pentane and decane is chosen as the working fluid for investigation of distillation effect in a two-dimensional slotted pore of 2 μm width. The physical properties of pentane and decane are obtained at working temperature of 300 K as

presented in Table 3.1, and the corresponding vapor was assumed to be saturated. Note that $x = 0$ is set to the point of zero evaporation mass flux as the beginning of the transition region in all the presented results.

Figure 3.19 represents the distribution of concentration rate of pentane in the transition film region that is the result of differential Eq. (3.81). The concentration in bulk meniscus region was fixed at pentane of 98 % and decane of 2 %. The concentration gradient is related to surface tension gradient. As explained in Table 3.1, the surface tension of decane is larger than that of pentane at the same thermal condition. Thus, the resulting surface tension in the thin film where decane is relatively rich is larger than that in bulk meniscus. This is confirmed in Fig. 3.20 that shows the interfacial surface tension distribution. Due to the concentration gradients as indicated in Fig. 3.19, the effective surface tensions act toward the adsorbed film region and thus they give rise to the improvement of the wettability of the liquid by spreading out the thin film region longer. The difference between surface tension variations of the pure pentane and the mixture will be also shown later.

The thin film profiles of binary mixtures having different concentration ratio of pentane are compared to that of pure liquid in Fig. 3.21, which shows that the evaporating film of binary mixtures are elongated toward the bulk meniscus region by the combined action of thermocapillary stress and distillation-driven capillary stress. From this result, it could be expected that the binary mixture can improve the stability of the thin film evaporation.

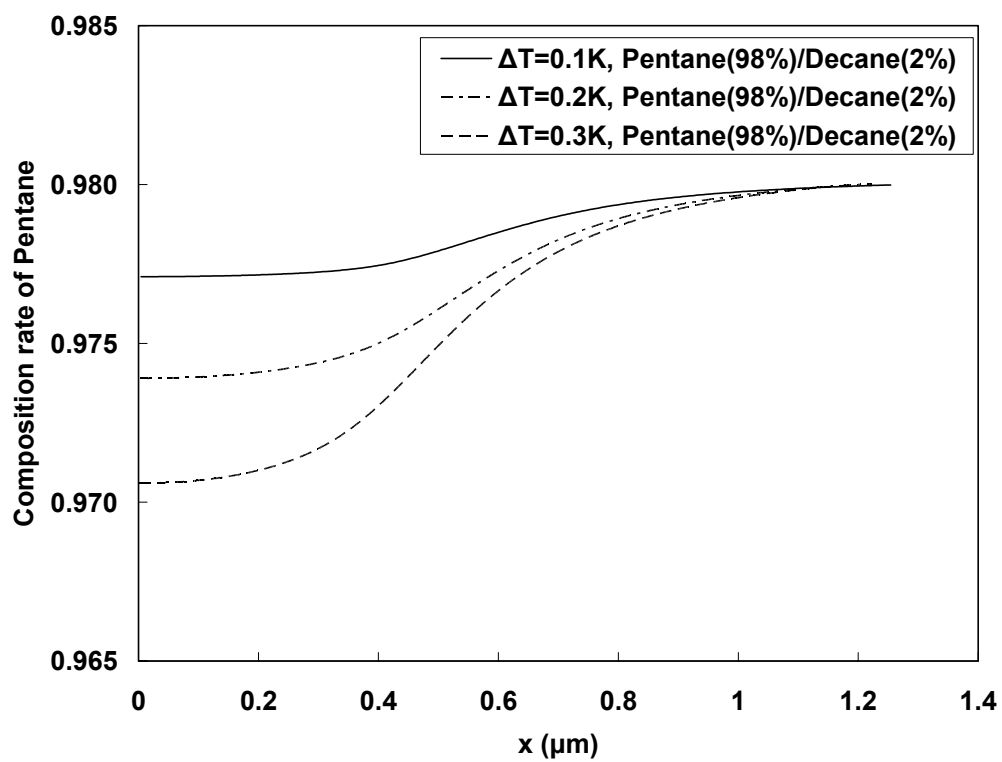


Fig. 3.19. Distribution of concentration rate of pentane under different superheat conditions.

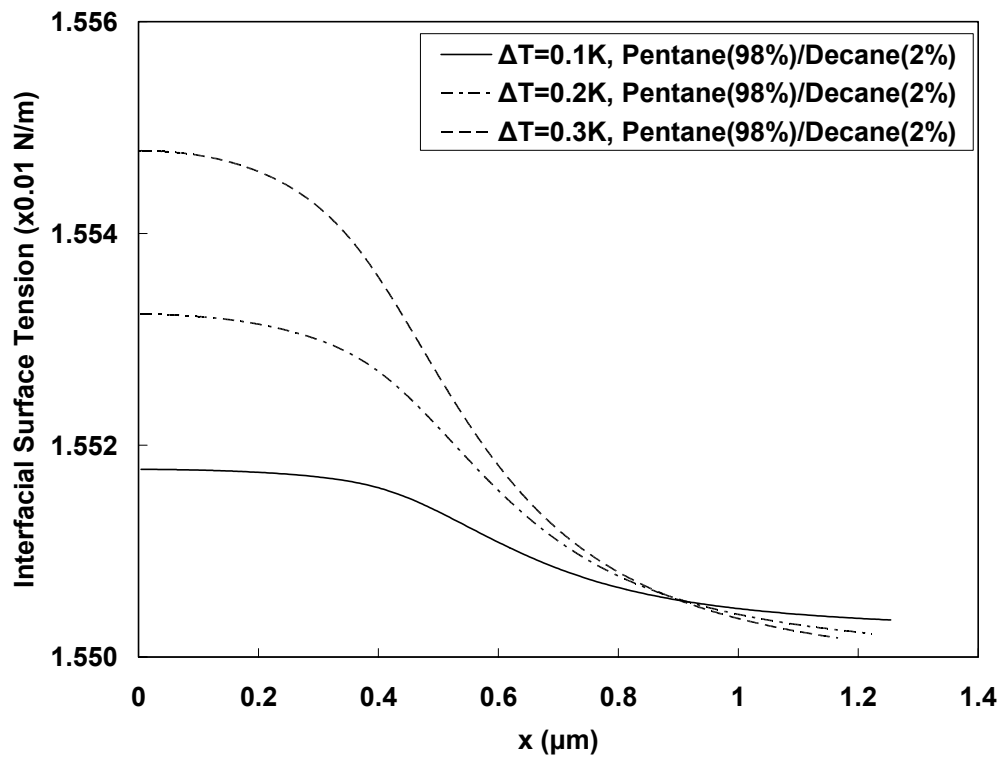


Fig. 3.20. Distribution of interfacial surface tension under different superheat conditions.

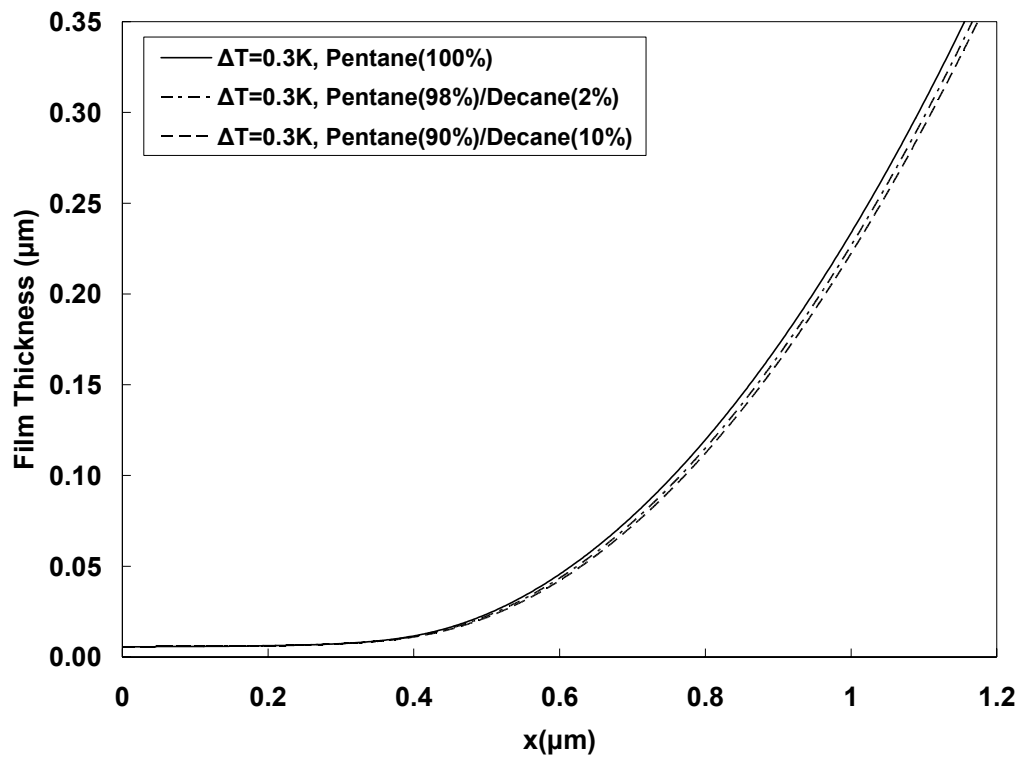


Fig. 3.21. Comparison of meniscus profiles between pure pentane (100%), mixture of pentane (98%) and decane (2%), and mixture of pentane (90%) and decane (10%) under the superheat of 0.3 K.

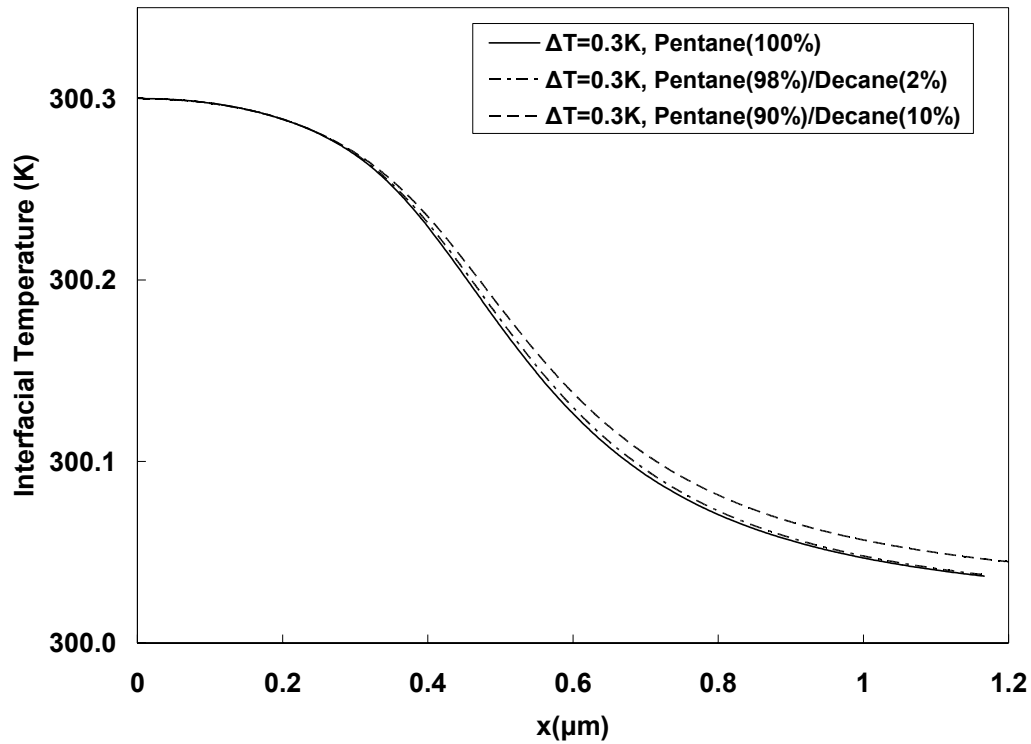


Fig. 3.22. Comparison of interfacial temperature distribution between pure pentane (100%), mixture of pentane (98%) and decane (2%), and mixture of pentane (90%) and decane (10%) under the superheat of 0.3 K.

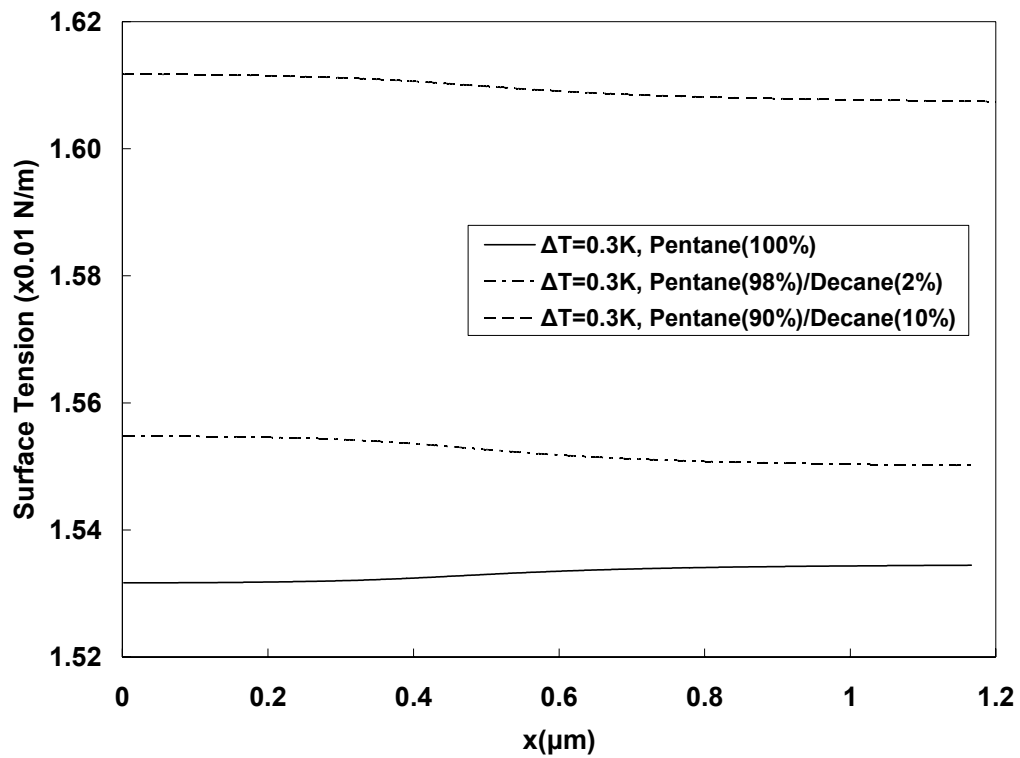


Fig. 3.23. Comparison of surface tensions between pure pentane (100%), mixture of pentane (98%) and decane (2%), and mixture of pentane (90%) and decane (10%) under the superheat of 0.3 K.

Figure 3.22 demonstrates the comparison of interfacial temperature profiles between the mixtures and the pure pentane at the superheat of 0.3 K. As expected, the gradients in temperature decrease in binary mixtures. As stated previously, the thermocapillary stress is induced due to the interfacial temperature gradient. Thus, the lower gradient in the temperature associated with the binary mixture evaporation leads to the smaller thermocapillary stresses and consequently such decreased thermocapillary stresses give rise to enhancement of stability in thin film evaporation.

Figure 3.23 shows the comparison of surface tensions between the pure pentane and the mixture of pentane and decane at the same superheat of 0.3 K. The figure definitely demonstrates a different distribution of surface tension for two cases. For pure pentane, the surface tension increases with increasing x -axis due to the interfacial temperature distribution and thus the resulting surface shear acts toward the bulk meniscus region that causes the length of thin film to be shorter. It results from the thermocapillary stress due to the temperature gradient. On the other hand, for the binary mixture of pentane and decane, the surface tension decreases with increasing axial coordinate and thus the effective surface shear acts toward the thin film region that causes the length of the thin film longer. It results from the combined effect of the thermocapillary stress and the distillation-driven capillary stress. Therefore, the distillation-driven capillary stress is larger than the thermocapillary stress and they are acting in opposite direction each other. The tendency of changes in film length for the pure pentane and the binary mixture was confirmed in Fig. 3.21.

3.5 Polarity Effect of Working Fluid

3.5.1 Background

The working fluid, which is usually used in a change of phase heat transport, is classified into polar and non-polar liquid by the polarity of the liquid. Pentane, decane, heptane, carbon tetrachloride belong to the non-polar liquid group, and water, ammonia, acetone, ethanol, and methanol are in the polar liquid group. Most of the liquids that have been used in the study of liquid-vapor phase change transport have been non-polar liquids since the mathematical formulation of non-polar liquid is simple compared to that of polar liquid. For non-polar liquid, the primary cause of the disjoining pressure is London dispersion forces resulting from the interaction of the positive nucleus of one molecule with the electrons of another molecule. The dispersion forces are the weakest of the van der Waals forces. Therefore, the intermolecular forces for non-polar molecules are weak for restraining the liquid molecules from evaporation and thus the evaporation rates are large. However, dispersion forces provide the most important contribution to the total van der Waals force between atoms and molecules because they are always present in non-polar and polar molecules as well. On the other hand, for polar liquids other interaction forces, such as dipole-dipole interactions are present. The positive charge of one molecule attracts the negative charge of another molecule (Logan, 1997). For a water molecule, negative charges around oxygen molecules attract the positively charged hydrogen molecule, which leads to strong dipole moment (Carpi, 1998). These forces are stronger and longer ranged than dispersion forces. Since polar fluid molecules yield much stronger intermolecular forces with a solid substrate, the

evaporation rate of polar liquid tends to be lower relative to non-polar liquid (Israelachvili, 1992). Most research of evaporating thin films has considered only non-polar liquids.

Recently, Qu and Ma (2002) studied the polarity effects of different working fluids on the evaporative heat transfer characteristics from a meniscus in a capillary tube. They noted that the disjoining pressure had strong effects on liquid film thickness profiles and the effects were more dominant in strongly polar working fluid such as water. They found that the strong disjoining pressure in a polar liquid leads to elongation of the evaporating interfacial region relative to that of non-polar liquids such as carbon tetrachloride and benzene. Their study, however, did not include the thermocapillary effect though nonisothermal interfacial conditions were incorporated.

Although extensive research of evaporating non-polar thin films has been performed due to the simplicity of modeling van der Waals intermolecular forces, a complete understanding has not been achieved yet. In this section, based on the study of Qu and Ma (2002), a mathematical model is developed to examine the effect of polar interactions between fluid and substrate by considering water as the working fluid. In this model a virtual non-polar model of water is imposed for the comparison of the polarity effect and the results are compared with those with a practical polar model to exclusively examine the polarity effect. The model developed in a cylindrical coordinate system also incorporates thermocapillary stresses due to nonisothermal interfacial conditions.

3.5.2 Mathematical Model of Polarity Effect

A mathematical model of an evaporating liquid thin film in steady state is considered for circular pore geometry as is illustrated in Fig. 3.24. The liquid is assumed to be heated by a uniform heat flux from a solid substrate causing evaporation from the liquid-vapor interface. It is assumed that the evaporative flow from the thin film is sustained by constant liquid inflow from the bulk meniscus controlled by gradients in capillary and disjoining pressure. The origin is set at the junction of the non-evaporating adsorbed film region and the evaporating transition region.

The mean curvature for circular pores is expressed as the sum of the circumferential curvature and axial curvature, which are represented in terms of the first and second derivative of the film thickness with the distance along the substrate:

$$K = \left(\frac{1}{R_o - h} \right) \left(1 + h_x^2 \right)^{-0.5} + h_{xx} \left(1 + h_x^2 \right)^{-1.5} \quad (3.82)$$

The subscript x indicates the derivative with respect to x and R_o is the radius of the circular pore.

The disjoining pressure form for polar liquid is utilized so as to ascertain the role of polar forces on the thin film thermo-fluid characteristics. For a polar liquid like water the disjoining pressure has been characterized for a two dimensional extended meniscus (Potash and Wayner, 1972) by the equation,

$$\Pi = -\rho_l R_g T_i \ln \left(P_{v,i} / P_{v,i}^0 \right) \quad (3.83)$$

where ρ_l is the density of the liquid phase, R_g is the gas constant, T_i is the liquid-vapor interface temperature, $P_{v,i}$ is the reduced saturation pressure of the film, and $P_{v,i}^0$ is the

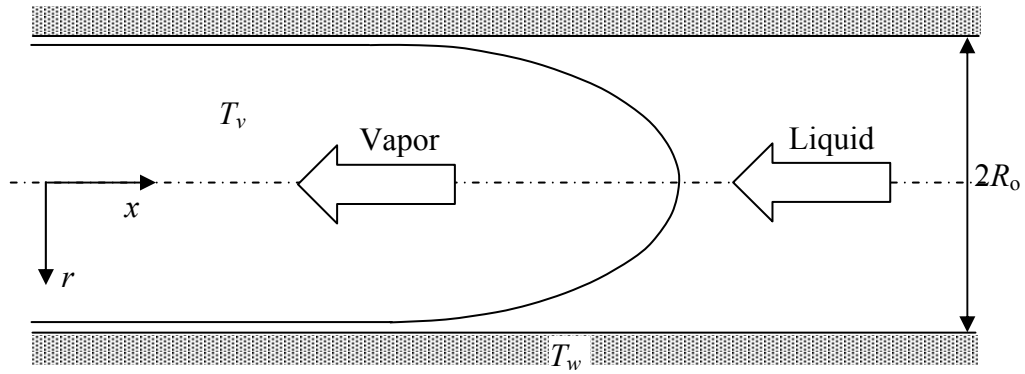


Fig. 3.24. Schematic of liquid-vapor interface forming within a cylindrical capillary pore with uniform wall temperature.

saturation pressure corresponding to T_i . Combining the experimental work of Derjaguin and Zorin (1957) with Eq. (3.83), Holm and Goplen (1979) developed the expression of the disjoining pressure as a logarithmic function of film thickness in the following form,

$$\Pi = -\rho_l R_g T_i \ln(\alpha h(x)^\beta) \quad (3.84)$$

For pure water on the quartz glass, the constants are given as $\alpha = 1.49$, $\beta = 0.0243$ (Holm and Goplen, 1979). The disjoining pressure for polar liquid is incorporated into augmented Laplace-Young equation (Eq. (3.1)) and evaporative mass flux equation.

The disjoining pressure for non-polar liquid is given in Eq. (3.5),

$$\Pi = \frac{A}{h^3} \quad (3.85)$$

where A is the dispersion constant equal to 3.11×10^{-21} Joules for water (Wayner et al., 1976).

The fluid dynamics can be modeled with the lubrication approximation yielding in cylindrical coordinate:

$$\frac{1}{r} \frac{\partial}{\partial r} \left(r \frac{\partial u}{\partial r} \right) = \frac{1}{\mu_l} \frac{dP_l}{dx} \quad (3.86)$$

The solution to the above differential equation is subject to the following boundary conditions at the solid wall and liquid-vapor interface respectively,

$$\text{at } r = R_o, \quad u = 0 \quad (3.87)$$

$$\text{at } r = R_o - h, \quad -\mu \frac{\partial u}{\partial r} = \frac{d\sigma}{dx} \quad (3.88)$$

The liquid velocity profile can now be determined by solving the axial momentum equation, Eq. (3.86), subject to the specified boundary conditions,

$$u(r) = \frac{1}{4\mu_l} \frac{dP_l}{dx} r^2 + C_1 \ln r + C_2 \quad (3.89)$$

$$\text{where } C_1 = -\frac{1}{\mu_l} \frac{d\sigma}{dx} (R_o - h) - \frac{1}{2\mu_l} \frac{dP_l}{dx} (R_o - h)^2 \quad (3.90)$$

$$C_2 = -\frac{1}{4\mu_l} \frac{dP_l}{dx} R_o^2 - C_1 \ln R_o. \quad (3.91)$$

Using the velocity profile given by equation (3.89), the mass flow rate across a cross sectional area of the film thickness h is obtained as follows:

$$\Gamma = \int_{R-h}^R \rho_l \left[\frac{1}{4\mu_l} \frac{dP_l}{dx} r^2 + C_1 \ln r + C_2 \right] 2\pi r dr \quad (3.92)$$

After integration, the following expression is derived:

$$\Gamma = C_6 \frac{dP_l}{dx} + C_7 \frac{d\sigma}{dx} \quad (3.93)$$

$$\text{where } C_6 = \frac{\pi}{8\nu_l} \left\{ [R_o^4 - (R_o - h)^4] - 4(R_o - h)^2 C_5 \right\} + \pi \rho_l (2R_o h - h^2) C_3, \quad (3.94)$$

$$C_7 = -\frac{\pi}{\nu_l} (R_o - h) C_5 + \pi \rho_l (2R_o h - h^2) C_4 \quad (3.95)$$

The coefficients C_3 , C_4 , and C_5 are defined as follows:

$$C_3 = \frac{1}{2\mu_l} \left[(R_o - h)^2 \ln R_o - \frac{1}{2} R^2 \right], \quad (3.96)$$

$$C_4 = \frac{1}{\mu_l} (R_o - h) \ln R_o, \text{ and} \quad (3.97)$$

$$C_5 = R_o^2 \left(\ln R_o - \frac{1}{2} \right) - (R_o - h)^2 \left[\ln(R_o - h) - \frac{1}{2} \right]. \quad (3.98)$$

These coefficients are related to the radius, R_o , film thickness, h , and μ_l and ρ_l . The evaporative mass flux is expressed in simplified form from Eq. (3.16),

$$\dot{m}_{evp} = a(T_i - T_v) + b(P_l - P_v) \quad (3.99)$$

The coefficients, a and b , are dependent on the physical properties of the liquid and defined as follows:

$$a = C \left(\frac{M}{2\pi RT_i} \right)^{1/2} \left(\frac{P_v M h_{fg}}{RT_v T_i} \right), \quad b = C \left(\frac{M}{2\pi RT_i} \right)^{1/2} \left(\frac{V_l P_v}{RT_i} \right) \quad (3.100)$$

A simplified energy equation for temperature profile is given in cylindrical coordinates,

$$\frac{\partial}{\partial r} \left(k_l r \frac{\partial T}{\partial r} \right) = 0 \quad (3.101)$$

Two boundary conditions are necessary at wall and liquid-vapor interface for obtaining the temperature distribution,

$$\text{at } r = R_o, \quad T = T_w \quad (3.102)$$

$$\text{at } r = R_o - h, \quad k_l \left. \frac{dT}{dr} \right|_{r=R_o-h} = \dot{m}_{evp} h_{fg} \quad (3.103)$$

These correspond to a specified wall temperature and a balance between conduction and evaporation heat transfer at the liquid-vapor interface, respectively. Solution of the energy equation, Eq. (3.101), subject to these boundary conditions gives the temperature variation along the interface,

$$T_i = -\frac{h_{fg}}{k_l} (R_o - h) \ln \left(\frac{R_o}{R_o - h} \right) \dot{m}_{evp} + T_w \quad (3.104)$$

The evaporation mass flux given by Eq. (3.99) is substituted into Eq. (3.104) and using the definitions for the disjoining pressure and capillary force to relate P_v in Eq. (3.99) to P_l , the final expression for the interfacial temperature results in

$$T_i = \frac{T_w k_l / F_1 + a T_v + b \sigma K}{k_l / F_1 + a + b \rho_l R_g \ln(\alpha h^\beta)} \quad (3.105)$$

$$\text{where } F_1 = (R_o - h) h_{fg} \ln\left(\frac{R_o}{R_o - h}\right) \quad (3.106)$$

Integrating the evaporative mass flux from the adsorbed film to an arbitrary x - location, the mass flow rate can be related to the interfacial temperature and film thickness as shown,

$$\Gamma(x) = -\frac{2\pi k_l}{h_{fg}} \int_0^x \frac{T_w - T_i}{\ln\left(\frac{R_o}{R_o - h}\right)} dx \quad (3.107)$$

This expression for $\Gamma(x)$ provides closure to Eq. (3.93). The R.H.S. of Eq. (3.93) must be equal to this expression for $\Gamma(x)$. In Eq. (3.93) the liquid pressure gradient can be obtained by differentiation of the augmented Laplace-Young equation, Eq. (3.2), in terms of x ,

$$\frac{dP_l}{dx} = -\sigma \frac{dK}{dx} - K \frac{d\sigma}{dx} - \frac{d\Pi}{dx} \quad (3.108)$$

The third order nonlinear differential equation for the film thickness profile can be obtained by substituting the expression for curvature (Eq. (3.82)) into Eq. (3.108) and rearranging:

$$\begin{aligned}
& h_{xxx} - 3h_{xx}^2 h_x (1 + h_x^2)^{-1} - h_{xx} h_x (R_o - h)^{-1} + h_x (1 + h_x^2) (R_o - h)^{-2} \\
& + \frac{\gamma}{\sigma} \left[(1 + h_x^2) (R_o - h)^{-1} + h_{xx} \right] \frac{dT}{dx} + \frac{1}{\sigma} (1 + h_x^2)^{1.5} \left(\frac{dP_l}{dx} + \frac{d\Pi}{dx} \right) = 0
\end{aligned} \tag{3.109}$$

The liquid pressure gradient in terms of x is achieved by equating Eqs. (3.93) and (3.107),

$$\frac{dP_l}{dx} = -\frac{C_7}{C_6} \frac{d\sigma}{dx} - \frac{2\pi k_l}{h_{fg} C_6} \int_0^x \frac{T_w - T_i}{\ln[R/(R-h)]} dx \tag{3.110}$$

In equation (3.109), the conservation of mass equation combined with the interfacial normal stress balance within the film reduced to a differential equation for the thin film thickness profile along the horizontal solid wall. In this equation, all of the related physical properties such as temperature, pressure, flow velocities and evaporative mass flux are represented in terms of the liquid film thickness, h , and its derivatives. The influence of polar solid-liquid intermolecular forces is imbedded in the disjoining pressure term in Eq. (3.109).

Due to the complexity of the model of disjoining pressure for polar liquid, the differential equation is difficult to be scaled in non-dimensional form as stated in previous sections. The ordinary differential Eq. (3.109) is directly solved using 6th order Runge-Kutta-Fehlberg method with three initial conditions at $x = 0$. In order to avoid trivial solutions as explained previously, a small perturbation is applied to the thickness and the slope. The solution of Eq. (3.109) is extremely sensitive to the specification of the initial condition for the first derivative of thickness especially as the superheat increases. An iterative technique is employed to guess the slope at $x = 0$ such that the solution converges to the appropriate curvature in the bulk meniscus region.

3.5.3 Results and Discussion

The working fluid is chosen as water for investigation of polarity effect in a cylindrical capillary pore of 20 μm diameter as presented in Fig. 3.24.

Figure 3.25 shows the change in the thin film profile for polar and non-polar liquids for the same superheat condition of 0.1 K. The length of the thin film or transition region, L_{tr} , is defined as the distance from the adsorbed region to the junction where the value of disjoining pressure is equal to that of capillary pressure. The length of transition region is calculated to 286 nm for polar liquid of water and to 96 nm for the case of non-polar liquid of water with its polarity bluntly neglected. The higher disjoining pressures of polar liquid tend to extend the junction of pressure equality toward the bulk region, which in turn results in the remarkable increase in L_{tr} . Also, the stronger attractive forces between the polar liquid and the solid substrate substantially increase the thin film thicknesses for the same superheat level. The elongation of the thin film region was similarly observed at high dispersion numbers, defined as the ratio of disjoining pressure to surface tension force, by Swanson and Herdt (1992). Qu and Ma (2002) compared the meniscus profiles of water with those of other non-polar liquids, such as carbon tetrachloride and benzene, and also showed that the transition region of a polar liquid is much longer than that of a non-polar liquid under the same superheat condition.

Figure 3.26 represents the comparison of disjoining pressure profiles for polar water (solid lines) and non-polar water (dashed lines) for the same superheat condition of 0.1 K. It is shown that the transition film length where the disjoining pressure is

significant is longer for the polar case due to its slower decrease of disjoining pressure, while the maximum value of the disjoining pressure remains the same for polar and non-polar water. The disjoining pressure of non-polar liquid gradually goes to zero based on Eq. (3.85), but that of polar liquid rather sharply drops to zero, reflecting the limitation of the disjoining pressure model for a polar liquid represented by Eq. (3.84). This deficiency later creates abrupt changes in the profiles of other physical parameters.

Figure 3.27 shows that the evaporative mass flux of non-polar liquid is larger than that of polar liquid. The discontinuity shown in the evaporative mass flux distribution for a polar liquid is attributed to the aforementioned deficiency of the model used to describe the disjoining pressure for polar liquids. The average evaporative mass flux per unit axial length of the thin film region, for a unit width of 1-m, is calculated to 0.155 kg/(m·sec) for a non-polar liquid and 0.027 kg/(m·sec) for a polar liquid. The associated evaporative heat transport rate in the transition region is 35 W/cm² for a non-polar and 6 W/cm² for a polar liquid. As stated previously, the strong intermolecular forces retard the evaporation of liquid molecules from liquid-vapor interface in polar liquid. Due to this reason the evaporative mass flux is smaller for a polar liquid than that of a non-polar liquid under an identical level of superheating.

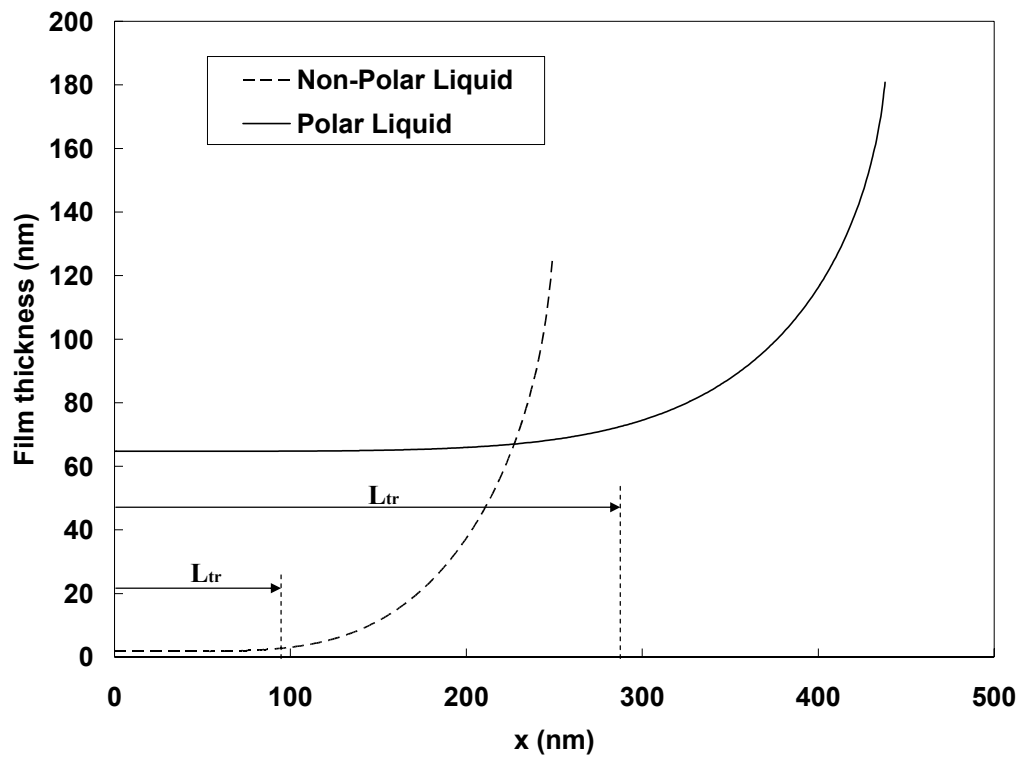


Fig. 3.25. Comparison of the thin film profiles of non-polar water and polar water for the same superheat condition of $\Delta T = 0.1$ K.

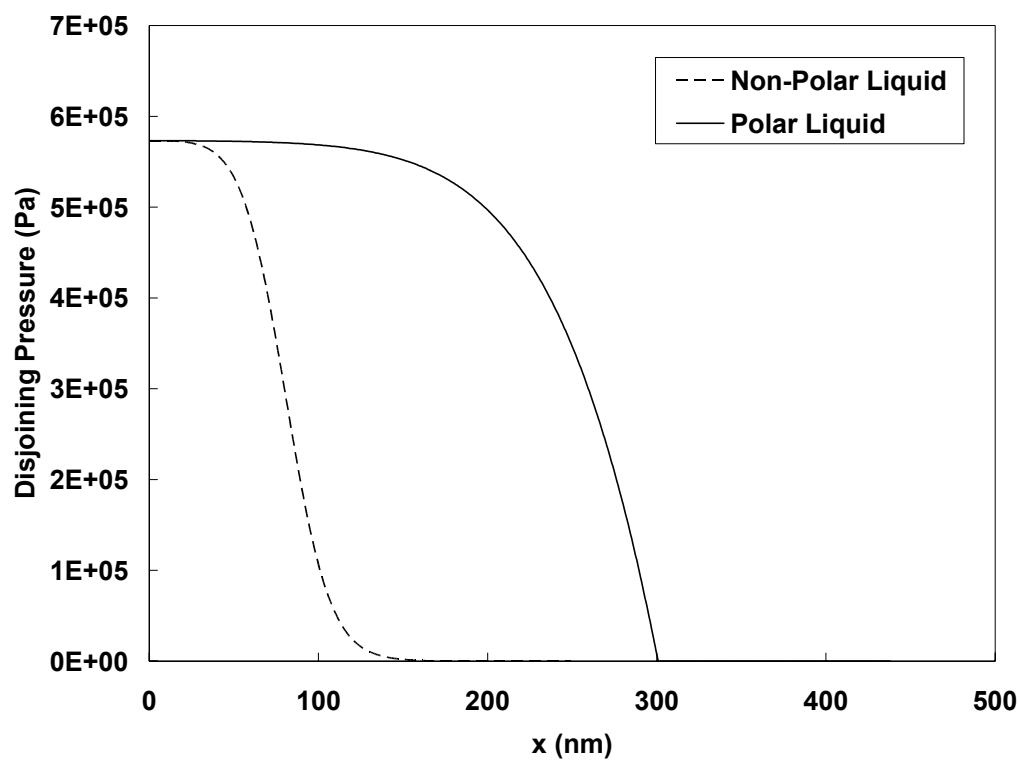


Fig. 3.26. Comparison of the disjoining pressure of non-polar water and polar water for the same superheat condition of $\Delta T = 0.1$ K.

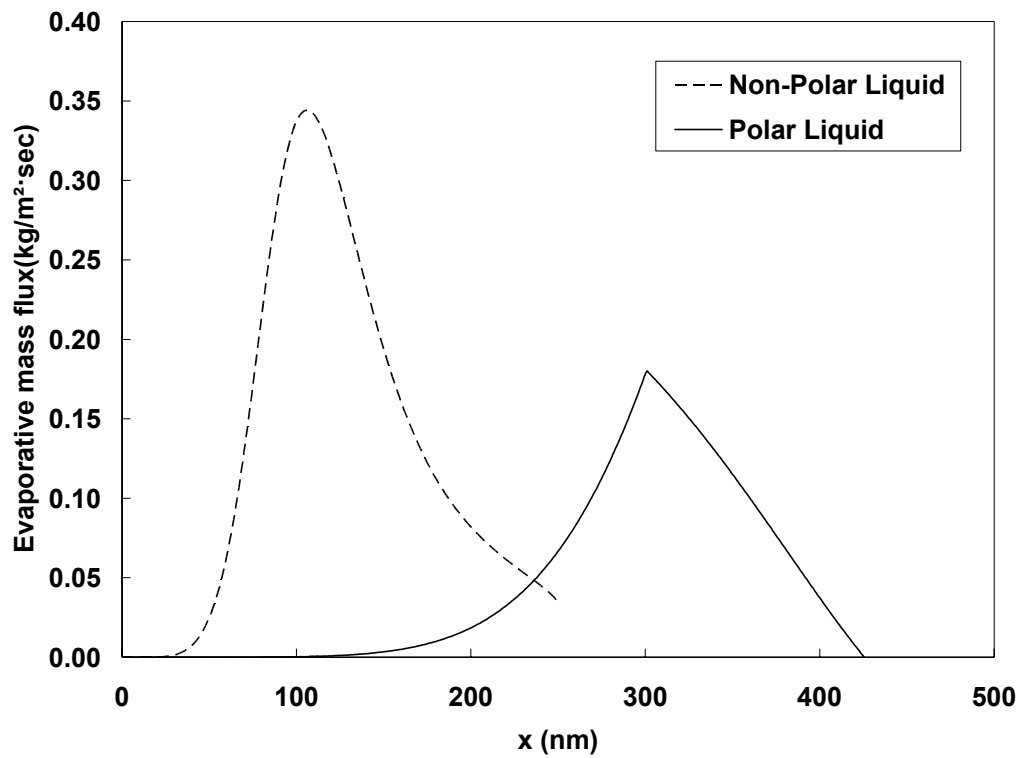


Fig. 3.27. Comparison of the evaporative mass flux of non-polar water and polar water for the same superheat condition of $\Delta T = 0.1$ K.

CHAPTER IV

EXPERIMENTS

4.1 Introduction

Recently a number of measurements techniques have been developed and extensively studied for increasing the resolution of measurements using advanced techniques in laser, optics, digital image processing and computer interface. Optical techniques using laser have provided many promises to the area of measurements. While various measurement techniques for velocity fields such as particle image velocimetry (PIV), particle tracking velocimetry (PTV), laser doppler velocimetry (LDV) have been relatively well developed, the techniques for temperature measurement are less developed. Currently the application of non-intrusive temperature measurement techniques is limited even though temperature is one of primary physical variables and the temperature distribution is also of critical importance in heat transfer researches. Most common means for temperature measurement is the use of thermocouple probe for a wide range of heat transfer application, but they have relatively large spatial resolution and are physically intrusive in the flow field. Other common technique for temperature measurement is based on thermo-chromic liquid crystals (TLC), but the spatial resolution of TLC is not enough for the application of thermometry in microscale temperature measurement. Instead of TLC, in order to bypass such difficulties of conventional methods in laser optical technique has been developed for temperature measurement of microscale area (Sakakibara and Adrian, 1999; Kim et al, 2003).

In general, the fluorescence intensity is proportional to the exciting light intensity and the concentration of the fluorescent dye. For some fluorescent dye like Rhodamine B, the fluorescence intensity depends on the temperature. This characteristic can be used to measure the temperature field of the flow containing the fluorescent dye if both the concentration and the exciting light intensity can be kept constant. The relative accuracy of this method is higher than that of the TLC method because it allows a wider range of variation of the temperature. However, the exciting light intensity may vary due to several effects such as laser beam divergence, scattering by small particles in the beam path, and refraction of the light passing through the thermal field itself. This may give rise to significant error in the optical measurement using single fluorescent dye. In order to overcome this problem, a new technique recently has been proposed to employ two fluorescent dyes whose emission intensities depend differently upon temperature. The ratio between the two fluorescence intensities is nearly independent of the incident light intensity (Sakakibara and Adrian, 1999).

Ratiometric laser induced fluorescence (LIF) thermometry using two fluorescence dyes, one with strong temperature dependence (Rhodamine-B, $2.3\% \text{ K}^{-1}$) and the other with little temperature dependence (Rhodamine-110, $0.13\% \text{ K}^{-1}$), have been developed for temperature measurement (Sakakibara and Adrian, 1999). The ratiometric LIF thermometry can provide a microscale spatial resolution without any background noise and laser light variation associated with convectional LIF technique. In this chapter, using these advantages of ratiometric LIF thermometry, the temperature measurement of a heated meniscus is investigated.

4.2 Principle of LIF Technique

4.2.1 Fundamentals of Fluorescence

Fluorescence is the property of certain molecules that is excited by incident light at a particular wavelength to a stimulated absorption state at a higher quantum energy level, and after a very short interval, termed the fluorescence lifetime, re-emits light at longer wavelengths, which are illustrated by the simple electronic-state diagram, called Jablonski diagram shown in Fig. 4.1. The process has three stages: excitation, quenching and emission. Fluorescent dye (or called fluorophore) adsorbs photon energy from external light source such as an incandescent lamp or a laser and the energy of a photon of the excitation light is given,

$$E_{EX} = \bar{h} \nu_{EX} = \bar{h} \frac{c_o}{\lambda_{EX}} \quad (4.1)$$

where \bar{h} is Planck's constant (6.62618×10^{-34} J·sec), c_o is light velocity, ν_{EX} is frequency of the excitation light and λ_{EX} is wavelength of the excitation light. The absorption of energy causes the fluorescent dye excited from ground state (G) to first excited state (S_1), which is excitation or absorption process. At the excited state, due to energy dissipation during the excited-state lifetime (typically 1-10 nano seconds), the energy of this photon is lower to second energy level (S_2) by quenching effect. The quenching is resulting from energy loss during the interaction with environment, which is usually caused by thermal dissipation. Finally fluorescent dye emits the light of a photon of energy ($\bar{h} \nu_{EM}$) and returns back to the initial ground energy level (G). The energy of a photon of the emission light is given,

$$E_{EM} = \bar{h} \nu_{EM} = \bar{h} \frac{c_o}{\lambda_{EM}} \quad (4.2)$$

where ν_{EM} is frequency of the emission light and λ_{EM} is wavelength of the emission light. Physically the emission of a photon is referred to as fluorescence. The emission light can be detected by a CCD camera. Fluorescent lamp has the same operating principle. As a result of energy loss resulting from quenching effect, excitation photon energy ($\bar{h} \nu_{EX}$) is larger than emission photon energy ($\bar{h} \nu_{EM}$). The difference in energy representing by $(\bar{h} \nu_{EX} - \bar{h} \nu_{EM})$ is called ‘Stokes shift’, which is referred to the fact that emission is generally shifted to longer wavelengths than the absorption because emission occurs from lower energy states. Stokes shift is a fundamental feature of fluorescence to allow one to separate the emission light from the excitation light optically, and the feature has been used for various optical measurement techniques (Haugland, 2002) such as laser induced fluorescence (LIF) thermometry and microscale particle image velocimetry (micro-PIV).

Fluorescence intensity emitted per unit volume at a specific point is defined as,

$$F = I_0 \varepsilon [c] \bar{Q} \quad (4.3)$$

where $F(W/m^3)$ is the measured fluorescence intensity for a fluorescent dye with molar absorptivity of $\varepsilon (m^2/kg)$ at a point in the incident light with intensity $I_0 (W/m^2)$, with concentration of the fluorescent dye solution $[c] (kg/m^3)$. In most organic dyes, the quantum efficiency is known to be temperature dependent. The fluorescence quantum efficiency or quantum yield \bar{Q} is a measure of the emission efficiency of the fluorescent

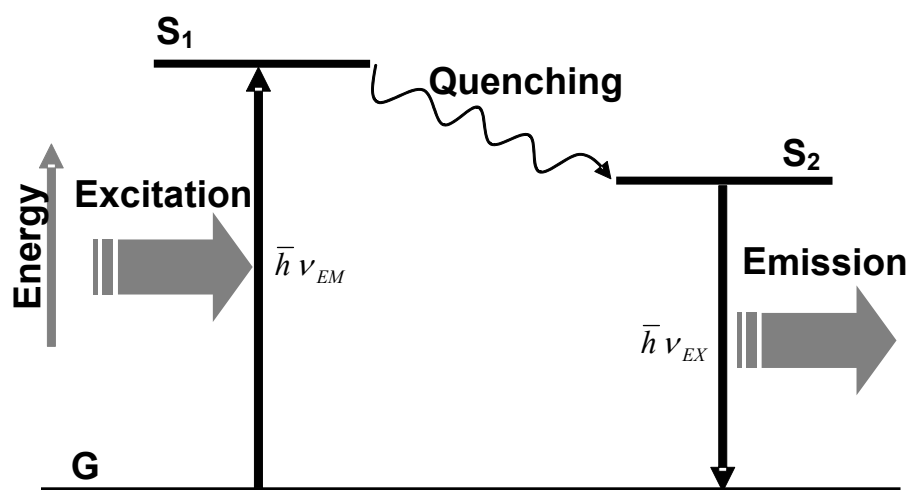


Fig. 4.1. Jablonski diagram describing excitation and emission of a photon.

dye and is expressed as the ratio of the number of photons emitted to the number of photons absorbed,

$$\bar{Q} = \frac{\textit{photons emitted}}{\textit{photons absorbed}} \quad (4.4)$$

The value of quantum efficiency ranges from 0 to 1 due to the energy loss (Herman, 1998).

As explained above, the exciting light intensity I_0 is influenced by various effects including convergence and divergence of the light sheet and refraction of the light passing through the thermal field. In addition to the spatial non-uniformity, the laser light is likely to be inhomogeneous temporally as well. In order to avoid these problem, it has been developed to measure the local, instantaneous intensity of the illuminating light at the same time. This can be done using additional fluorescent dye with a quantum efficiency that is not sensitive to temperature and thus it can be possible by using a mixture of two fluorescent dyes whose quantum efficiencies differ. In addition, the two dyes should have different emission spectra so that the two emitted lights can be separated by optical means. For the reason, a mixture of Rhodamine-B and Rhodamine-110 is used in this work. As a result, the ratiometric LIF technique can be a good alternative to temperature measurement without any troubles usually encountered in conventional LIF technique using single fluorescent dye. When the temperature dependency of quantum efficiencies of the two fluorescent dyes differs significantly, the ratiometric LIF technique will provide a good sensitivity to temperature (Sakakibara and Adrian, 1999).

For the case of a laser beam of light passing through a homogeneous fluorescent solution containing Rhodamine-B (Rh-B) and Rhodamine-110 (Rh-110), the intensity ratio of the two fluorescence emissions can be expressed as

$$\frac{F_{RhB}}{F_{Rh110}} = \frac{I_{0RhB} \varepsilon_{RhB} [c]_{RhB} \overline{Q}_{RhB}}{I_{0Rh110} \varepsilon_{Rh110} [c]_{Rh110} \overline{Q}_{Rh110}} \quad (4.5)$$

where molar absorptivity is ε is nearly independent of temperature. It was noted that the temperature dependence of the absorption coefficient is less than 0.05 % K⁻¹ for both fluorescence dyes (Sakakibara and Adrian, 1999). The ratio of the absorption spectral intensity, I_{0RhB}/I_{0Rh110} , is invariant when a single illumination source is used for both dyes. In addition, if the constant concentration ratio, $[c]_{RhB}/[c]_{Rh110}$, is maintained, the fluorescence intensity ratio, F_{RhB}/F_{Rh110} , is solely dependent on the quantum efficiency ratio of the two dyes, $\overline{Q}_{RhB}/\overline{Q}_{Rh110}$. Therefore, Eq. (4.5) indicates that the fluorescence intensity ratio is dependent on temperature since the quantum efficiency is dependent on temperature, not illuminating light intensity while keeping the concentration of dye.

4.2.2 Spectral Characteristics of Rh-B and Rh-110

In this experiment, two fluorescent dyes having different spectral characteristics are used. Rhodamine-B (J. T. Baker, Inc.) is used for temperature sensitive dye because its temperature sensitivity as large as 2.3% K⁻¹ and its absorption spectrum covers the range of 470-600 nm, which makes the dyes excited easily by conventional visible lasers such as Argon-ion laser. Rhodamine-110 (Molecular Probes, Inc.) is used for non-temperature sensitive dye since its temperature dependence is much smaller (0.13% K⁻¹)

and it has an absorption spectrum similar to Rh-B but a different emission band. Figure 4.2 shows the spectra of absorption and emission of Rh-B and Rh-110. Since the overlapping region of each absorption spectrum ranges from 480 to 530 nm as shown in the figure, the exciting light wavelength should be in this range to excite both fluorescent dyes simultaneously. For this reason 488 nm line of Argon-ion laser was chosen as the exciting light wavelength in this work. It should be also noted that the emission spectrum is shifted from absorption spectrum by Stokes shift, which allows the emission spectrum to be separated from the absorption spectrum by means of optical filtering using two color filters for two dyes. Table 4.1 summarizes the spectral characteristics of Rh-B and Rh-110.

Table 4.1
Spectral characteristics of Rh-B and Rh-110 (Solvent: de-ionized water, T=20°C)
(Sakakibara and Adrian, 1999)

Dye	Absorption peak[nm]	Emission peak[nm]	Temperature sensitivity	Quantum efficiency
Rh-B	554	575	2.3% K ⁻¹	0.31
Rh-110	496	520	0.13% K ⁻¹	0.8

4.3 Calibration Experiment

4.3.1 Experimental Setup

To measure a temperature field of water solution using ratiometric laser induced fluorescence technique, the correlation between fluorescence intensity and temperature should be determined in calibration experiment before actual application of the

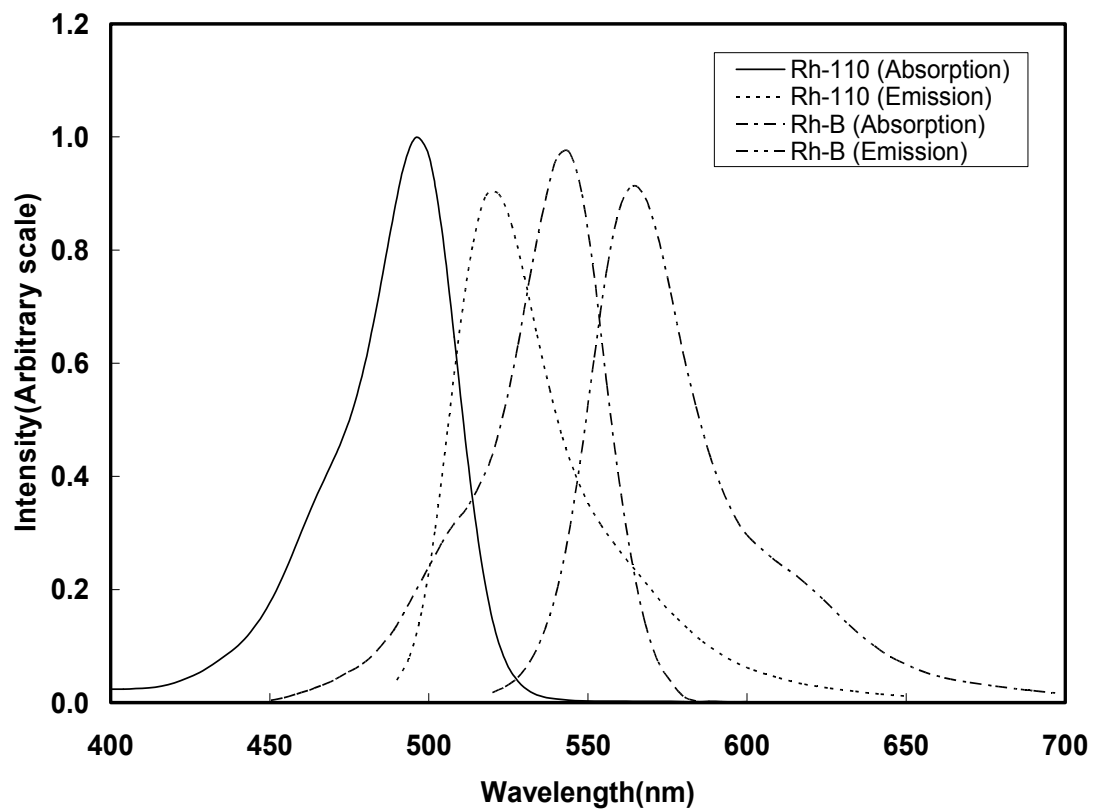


Fig. 4.2. Absorption and emission spectra of Rhodamine-110 and Rhodamine-B.

measurement. The schematic layout of the experimental setup employed in this experiment is shown in Fig. 4.3. The main objects in this set up are an Argon-ion laser (20 mW), a convex lens and a cylindrical lens, CCD camera (SONY XC75), color filters (Edmond Industrial Optics) and test section. The test section is comprised of a glass cuvette (Cole Parmer Co.) containing the mixture of Rh-B (1 mg/liter) and Rh-110 (0.17 mg/liter). The dye solution of the current system was diluted relative to that of Kim (2001) and Lee (2003) so that a reabsorption problem associated with total internal reflection of laser light in curved liquid-vapor interface could be bypassed. The glass cuvette is 10 mm in width and 35 mm in length. The glass cuvette is held by copper blocks soldered onto copper pipes which are connected to water hoses from two thermostats that circulate water at different temperature to obtain intended thermal field inside the glass cuvette. The convex lens and the rod lens (Edmond Industrial Optics) are used to expand the light of a laser beam with a wavelength of 488 nm emitted from the Argon-ion laser to a laser sheet with a thickness of approximately 0.5 mm that covers the whole thermal field of interest. The emission lights of Rh-B and Rh-110 are optically separated by the use of the two color filters: a longpass filter ($\lambda > 560 \text{ nm}$) and a bandpass filter ($505 \text{ nm} < \lambda < 515 \text{ nm}$). Figure 4.4 describes the incident light and optical filtering in the spectral diagram. The 488 nm line of Argon-ion laser excites two dyes at the same time. At the spectral line two dyes are excited by different amount of intensity due to the different spectral characteristics of fluorescent dyes. Thus, the optimum of the concentration ratio should be determined to maximize the accuracy of temperature measurement at the given spectral line of the exciting light. The

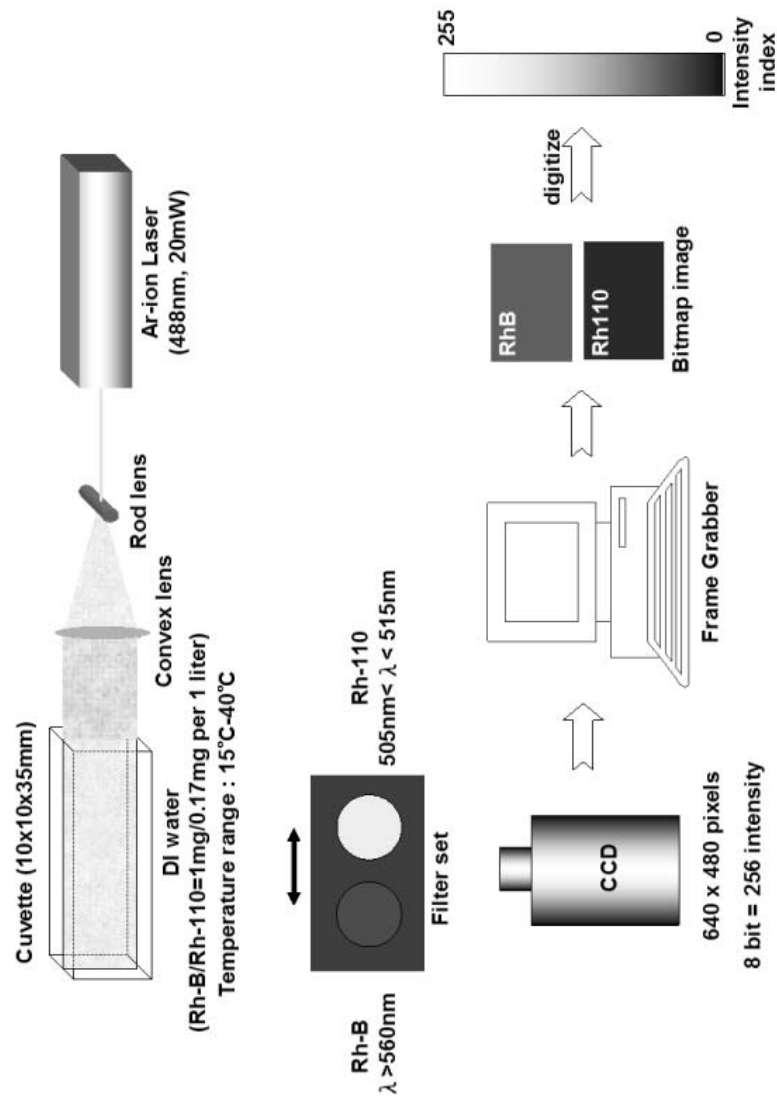


Fig. 4.3. Schematic layout of the experimental set up of calibration for ratiometric LIF technique.

concentration ratio, $[c]_{RhB}/[c]_{Rh110} \approx 6$ was chosen for the present system (Kim, 2001). The spectra of emission and absorption of Rh-B and Rh-110 are overlapping each other. To minimize the signal errors resulting from the overlapping spectra the emission light should be separated effectively using proper filters. The bandpass filter is used to separate the emission light of Rh-110 from 505 nm to 515 nm. The longpass filter is selected to separate the emission light of Rh-B for longer wavelength than 560 nm. Each emission light of Rh-B and Rh-110 is imaged through the filters by the CCD camera while alternating the filters. The video images from the CCD camera were digitized by a frame grabber (Aymetrix Corp.) and transferred to the memory of a PC at 30 frames per second and then the bitmap images of Rh-B and Rh-110 are transferred to digital data of successive grey level ranging from 0 to 255 by converting software. The average of intensities of successive 30 frames is used for obtaining the intensity ratio between Rh-110 and Rh-B. The intensity of 0 represents perfect black and 255 is perfect white.

Calibration curve is obtained in the temperature range of 14 °C to 40 °C. The test channel of a glass cuvette is placed between copper blocks which are soldered onto copper pipes that are connected to water hoses from two thermo-baths as illustrated in Fig. 4.5. The copper block and copper pipe are bonded by thermal glue to increase thermal conductivity. The thermo-baths are controlled to obtain uniform temperature of the solution in the glass cuvette containing fluorescent dyes and the temperatures are monitored by thermocouples embedded in the space between the copper block and a digital multimeter to ensure intended uniform temperature. It is assumed that the convective heat transfer with environment is negligibly small. To make this assumption

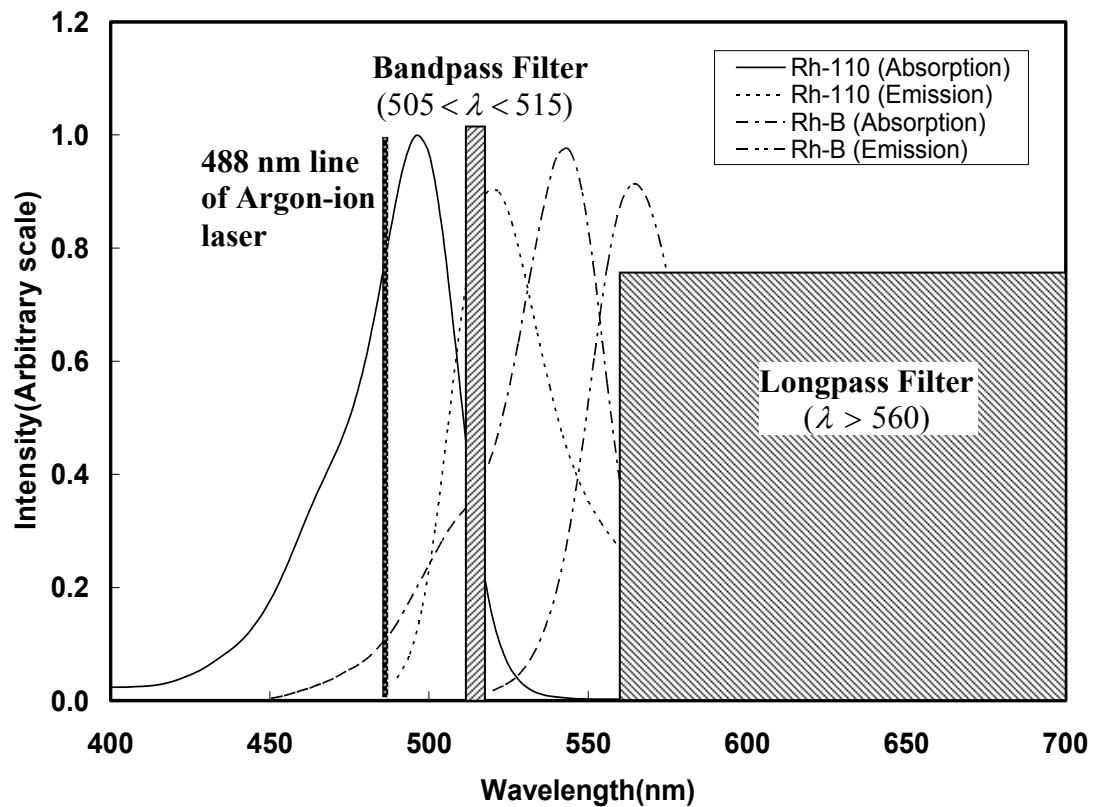


Fig. 4.4. Incident laser light (488 nm) and optical filtering using bandpass filter for emission light of Rh-110 and longpass filter for emission light of Rh-B.

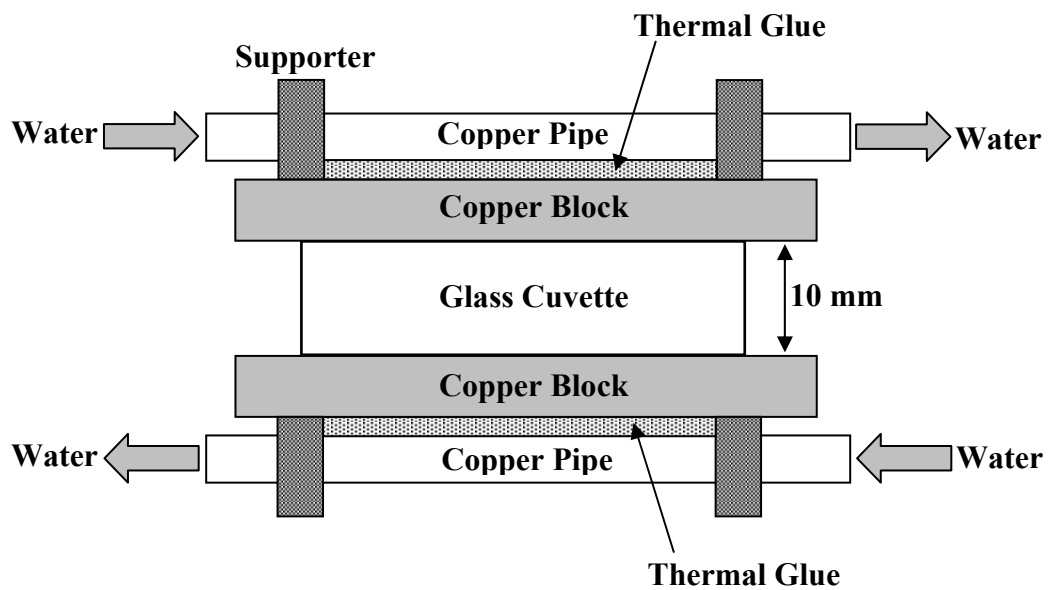


Fig. 4.5. Schematic of the test channel of a glass cuvette hold between copper blocks connected to copper pipes.

reasonable, the midst section of the thermal field is illuminated. This test section is also used to validate obtained calibration curve by making a thermally stratified field, which is established by circulating hot water at top surface and cooled water at bottom surface of the glass cuvette.

4.3.2 Calibration Results

The correlation of fluorescence intensity ratio and temperature are obtained in the calibration experiment. The calibration curve is used to measure temperature field indirectly. The raw images of Rh-B and Rh-110 are shown in Fig. 4.6 for four different temperatures. The column (c) indicates the ratiometric images. The interrogation window dimension is 320 pixels in width by 240 pixels in height and the corresponding field-of-view is 4 mm by 3 mm. The emission intensities of Rh-B decrease with increasing temperature. The brightness of the images decreases as temperature increase, but it is not clear in this figure due to low concentration of the solution. On the other hand, the emission intensities of Rh-110 are nearly invariant. Such tendency of intensity versus temperature is confirmed by intensity values represented on the images which indicates the averaged intensity that was calculated from 30 successive images captured for 1 second. The Rh-B images clearly show the temperature dependence of the intensity. The ratiometric images in column (c) indicates more clear image relatively since the background intensity variations are canceled out by normalizing the Rh-B images with the corresponding Rh-110 images. In general such background intensity variations result from the laser light non-uniformity usually caused by the non-uniform laser beam

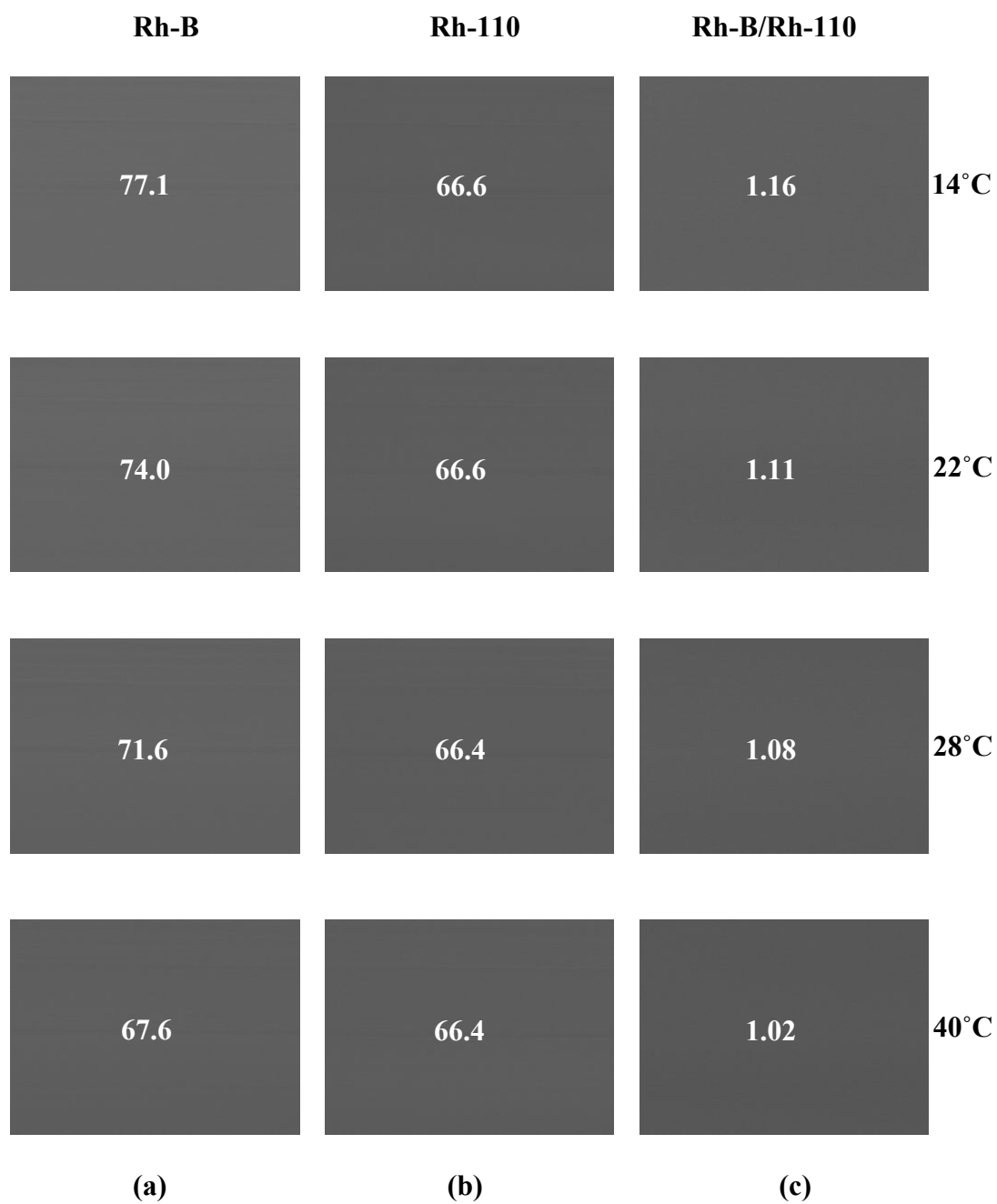


Fig. 4.6. Temperature dependency of fluorescence images of Rh-B (column a), Rh-110 (column b) and the ratiometric images (column c).

characteristics, imperfect lens characteristics, varying refractive index due to thermal variation and suspending impurities in the circulating water. As a result, the resulting ratiometric images show highly homogeneous decrease with increasing temperature and the intensity ratio also indicates linear decrease with temperature which is confirmed in Fig. 4.8. The same trend was more clearly observed in the experiments by Kim (2001) and Lee (2003) because the concentration of the solution was 6 times denser than that in a current dye solution.

Figure 4.7 indicates the intensity variation of Rh-B and Rh-110 with temperature. As explained previously, it is clearly shown that the intensities of Rh-B decrease with increasing temperature while the intensities of Rh-110 are nearly invariant. The vertical bars indicate the standard deviation with 95 % confidential level. Figure 4.8 indicates the calibration curve and vertical bars express standard deviation with 95 % confidential level. It is necessary to ensure the repeatability of the calibration curve, so the intensity ratios were obtained several times at the same temperatures and then the values were averaged. The experimentally obtained data are fitted to various polynomial of order in a least-square sense to achieve a best fitting. The polynomial of best fitting is chosen for the temperature measurement. In this work, 3rd order polynomial is employed as the best fitting. It should be noted that the intensity variations in Figs. 4.7 and 4.8 are based on the smallest spatial resolution of a single pixel that is equivalent to a spatial resolution of $12.5 \mu\text{m} \times 12.5 \mu\text{m}$. Table 4.2 is presented to examine the spatial resolution dependency of the calibration uncertainties of the current system for ratiometric LIF technique. It shows a statistical analysis of calibration data for the interrogation window size from a

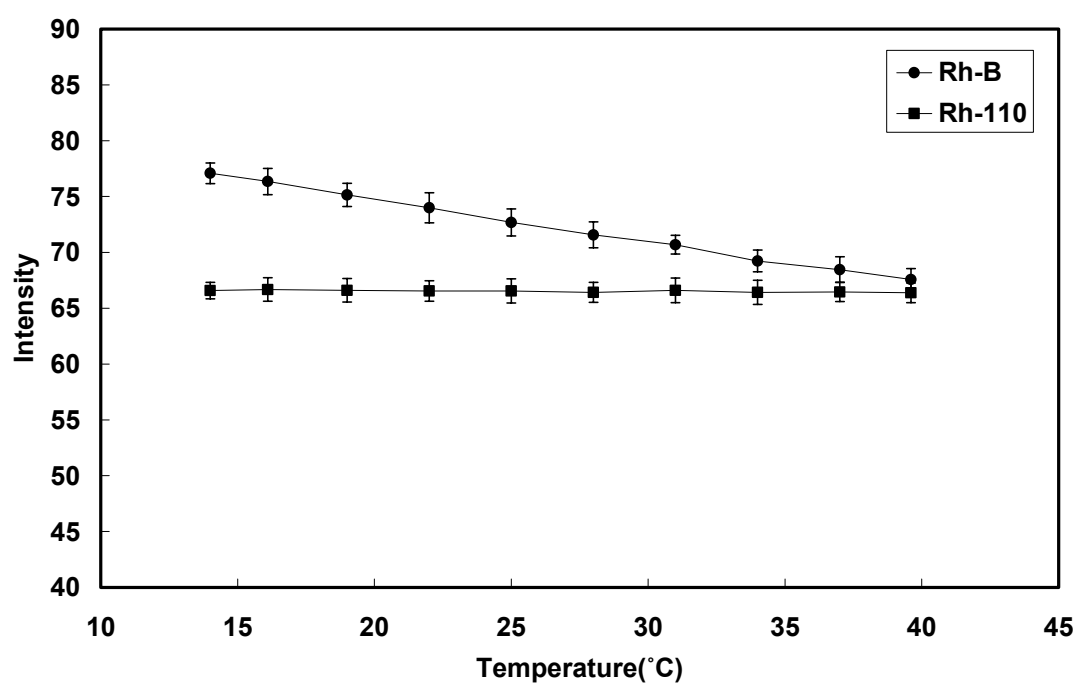


Fig. 4.7 Variation of the fluorescence intensities for Rh-B and Rh-110 against temperature ranging from 14 °C to 40 °C.

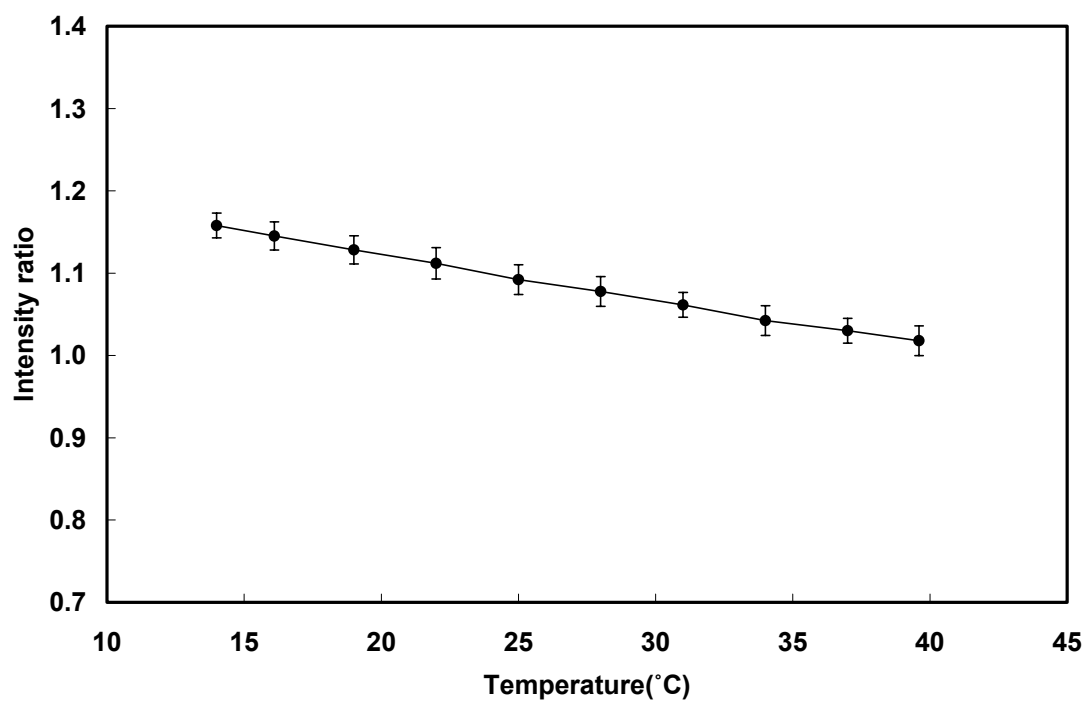


Fig. 4.8 Variation of the fluorescence intensity ratios for Rh-B and Rh-110 against temperature ranging from 14 °C to 40 °C.

Table 4.2
Spatial resolution dependency of calibration curve uncertainty

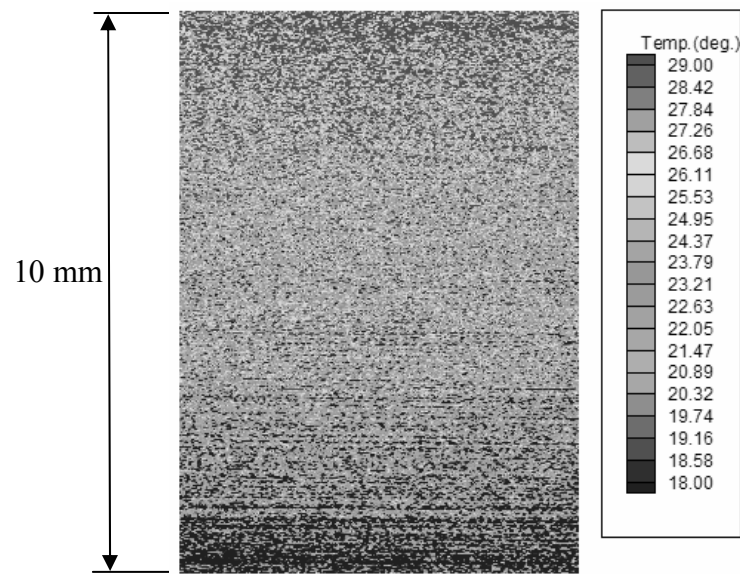
Interrogation window dimension (pixels)	Spatial resolution (μm)	Intensity ratio deviation	Temperature deviation ($^{\circ}\text{C}$)
1 \times 1	12.5 \times 12.5	± 0.0176	± 3.36
4 \times 4	50 \times 50	± 0.0121	± 2.26
8 \times 8	100 \times 100	± 0.0105	± 1.94
64 \times 48	800 \times 600	± 0.0101	± 1.64
160 \times 120	2000 \times 1500	± 0.0043	± 0.71
160 \times 240	2000 \times 3000	± 0.0027	± 0.37
320 \times 240	4000 \times 3000	± 0.0000	± 0.00

single pixel to the whole field-of-view. Standard deviation of the intensity ratio is calculated for each calibration temperature with 95 % confidence level for a given interrogation window. The temperature deviation decreases as interrogation window dimension increases and ultimately the temperature deviation diminishes to zero when the whole field-of-view is considered as a single interrogation window.

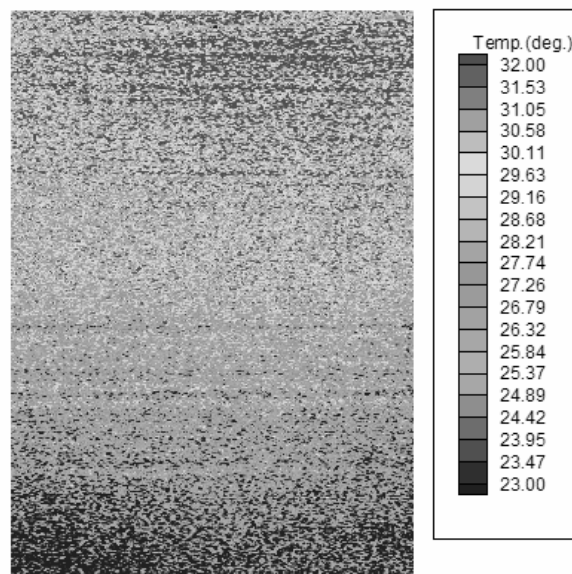
4.3.3 Temperature Measurement of Thermally Stratified Fields

For validation of the calibration curve obtained in the calibration experiment, temperature measurements of thermally stratified fields are conducted. The experimental setup is the same as that of the calibration experiment as shown in Fig. 4.3. The test section also is equivalent to the glass cuvette placed between copper blocks used in the calibration experiment as illustrated in Fig. 4.5. However, in this experiment the solution in the glass cuvette is intentionally made to have thermally stratified fields by circulating water from two thermo-baths maintained at different temperatures. The top surface is maintained to be heated and the bottom surface is maintained to be cooled. For nearly steady state, thermally stratified fields are obtained and linear temperature profiles are expected since there are no buoyancy driven convection flows due to temperature gradients in such thermal conditions.

Fig. 4.9 (a) and (b) show temperature contours of thermally stratified fields for two different temperature conditions. The steady state thermal fields were obtained about 30 minutes after setting the temperatures of thermo-baths. The temperatures were monitored continuously before and after nearly steady state temperature field obtained.

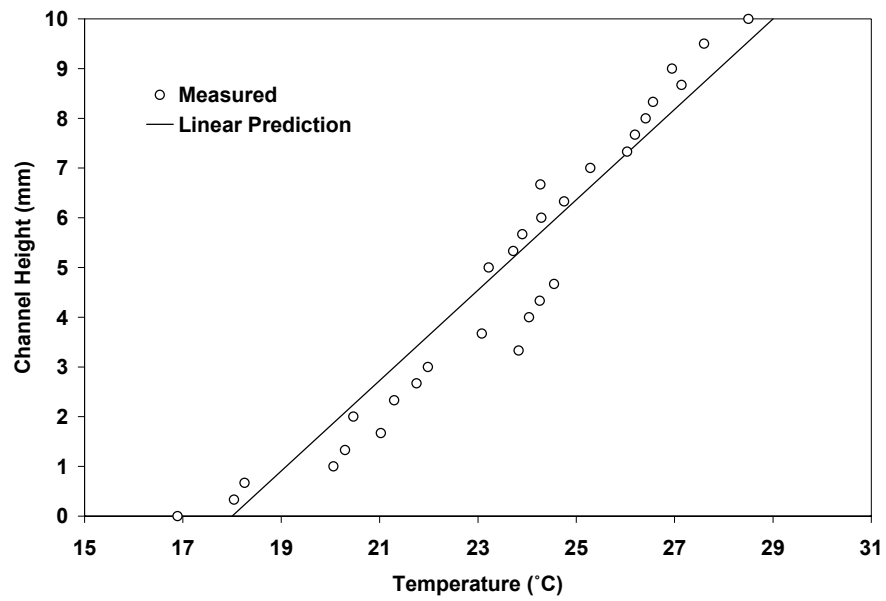


(a) Case 1: $T_{\text{top}}=29^{\circ}\text{C}$, $T_{\text{bottom}}=18^{\circ}\text{C}$

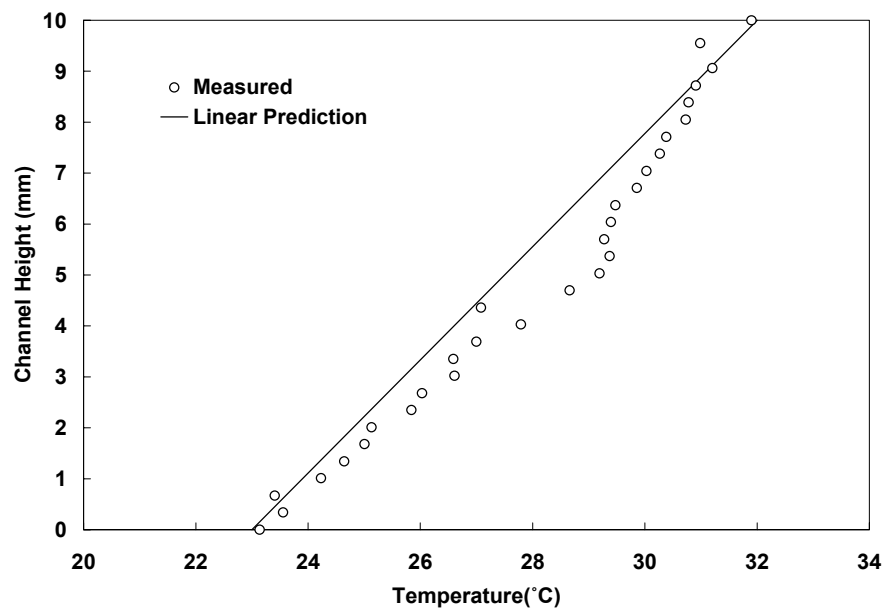


(b) Case 2: $T_{\text{top}}=32^{\circ}\text{C}$, $T_{\text{bottom}}=23^{\circ}\text{C}$

Fig. 4.9. Temperature contours of thermally stratified fields for 10 mm channel.



(a) Case 1: $T_{\text{top}}=29^{\circ}\text{C}$, $T_{\text{bottom}}=18^{\circ}\text{C}$



(b) Case 2: $T_{\text{top}}=32^{\circ}\text{C}$, $T_{\text{bottom}}=23^{\circ}\text{C}$

Fig. 4.10. Comparison of measured results and linear predictions of thermally stratified fields for 10 mm channel.

The temperature information was achieved by converting the measured intensity ratios into temperature values at each pixel position using the calibration curve. Fig. 4.9 (a) and (b) show the temperature contours for temperature difference of 11°C and 9°C, respectively, between top and bottom surfaces. Fig. 4.10 (a) and (b) show the comparison of temperature profile between measured data and linear predictions for the two thermal conditions. The temperature profiles measured show good agreements with ideal profiles of linear prediction. The measured data were obtained by averaging temperatures in interrogation window size of 16 by 16 pixels. In the case (a), the temperature measurement error based on root mean square (RMS) is 0.91 °C and in the case (b), the error is 0.67 °C.

4.4 Temperature Measurement of a Heated Glass Channel

4.4.1 Test Cell

Temperature measurement is performed using the test apparatus as schematically illustrated in Fig. 4.11. The test field is a glass channel (1 mm by 1 mm square cross sectional shape, VitroCom Inc.) containing the fluorescent solution. An aluminum foil heater with 0.1 mm in thickness is attached to the glass channel. The heater is located at 3 mm away from the meniscus forming in the glass channel. The Teflon tube is connected to the glass channel so that the location of the meniscus can be controlled by injecting or removing the solution with a syringe. The Teflon tube is circular shape with 2 mm in diameter. Other equipments such as optics, laser and CCD are equivalent to the setup used in the calibration experiment in Fig. 4.3.

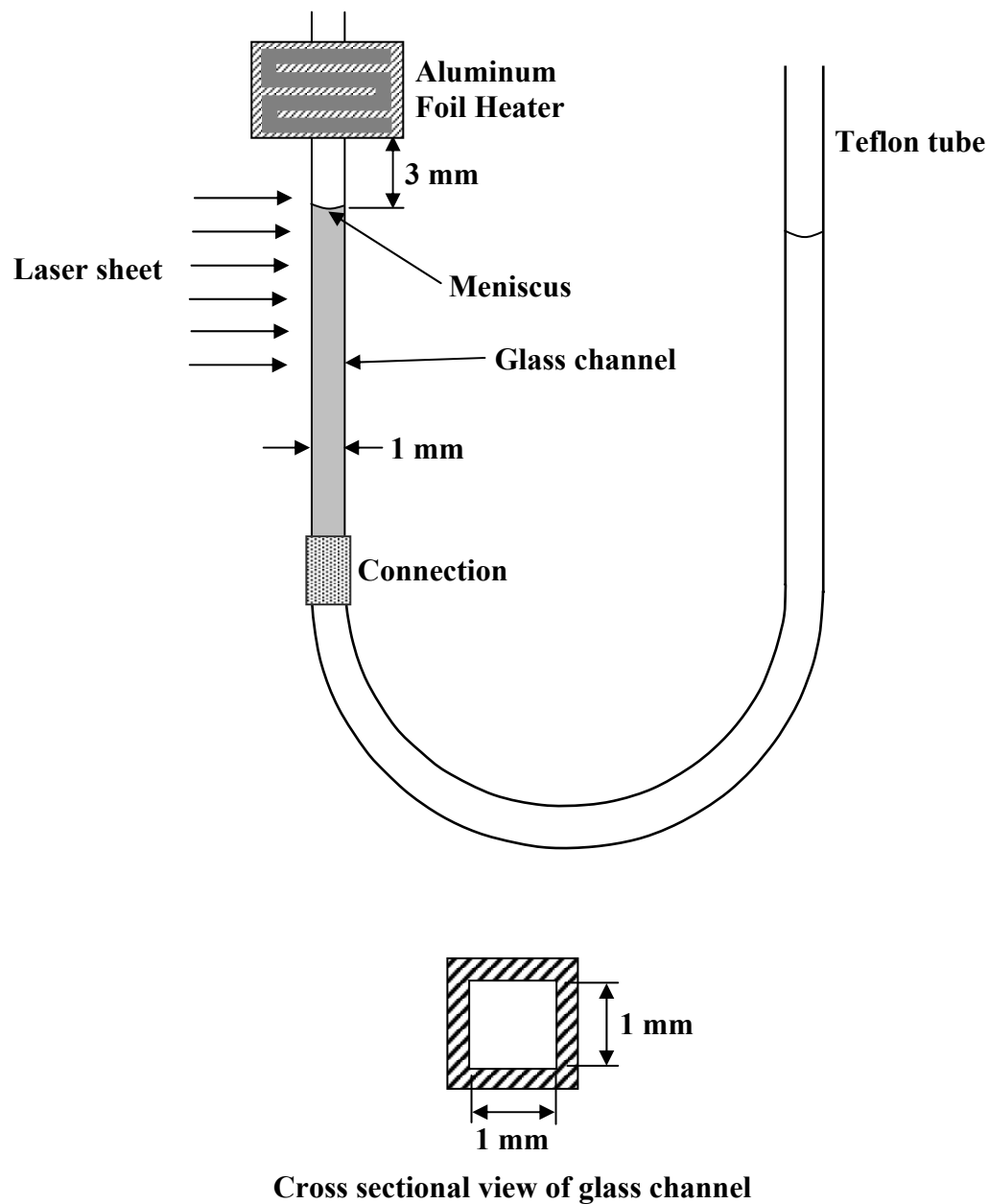


Fig. 4.11. Schematic of test section of capillary tube and the cross sectional view of the glass channel.

4.4.2 Results and Discussion

The temperature fields of three different thermal conditions are measured in this experiment. The temperature from heater can be controlled to be sustained at three different conditions by setting current and voltage from a power supply. The thermal conditions are summarized in Table 4.3.

Table 4.3
Three thermal conditions for the experiment of heated capillary tube

	Heater Temperature	Room Temperature	Input Heat Flow
Case 1	32 °C	21 °C	0.27 W
Case 2	38 °C	21 °C	0.43W
Case 3	44 °C	21 °C	0.62W

The room temperature is 21 °C, so the region inside the Teflon tube far away from the heated portion is expected to be maintained at the room temperature. The input heat flow was calculated by the production of voltage and current applied. Figure 4.12 shows raw images of Rh-B and Rh-110 for Case 1. The original field of view is 480 pixels (width) by 640 pixels (height) equivalent to 6 mm by 8 mm. Herein, however, the images are cropped to get the image around the channel as shown in Fig. 4.12. The field of view is 3.1 mm by 6.6 mm. The bright light reflected from the meniscus is shown that cause the error in temperature measurement. The laser light reflection from the meniscus induces the bias error of temperature measurement associated with reabsorption problem that was identified in the experiment of Lee (2003). The temperature measured around the

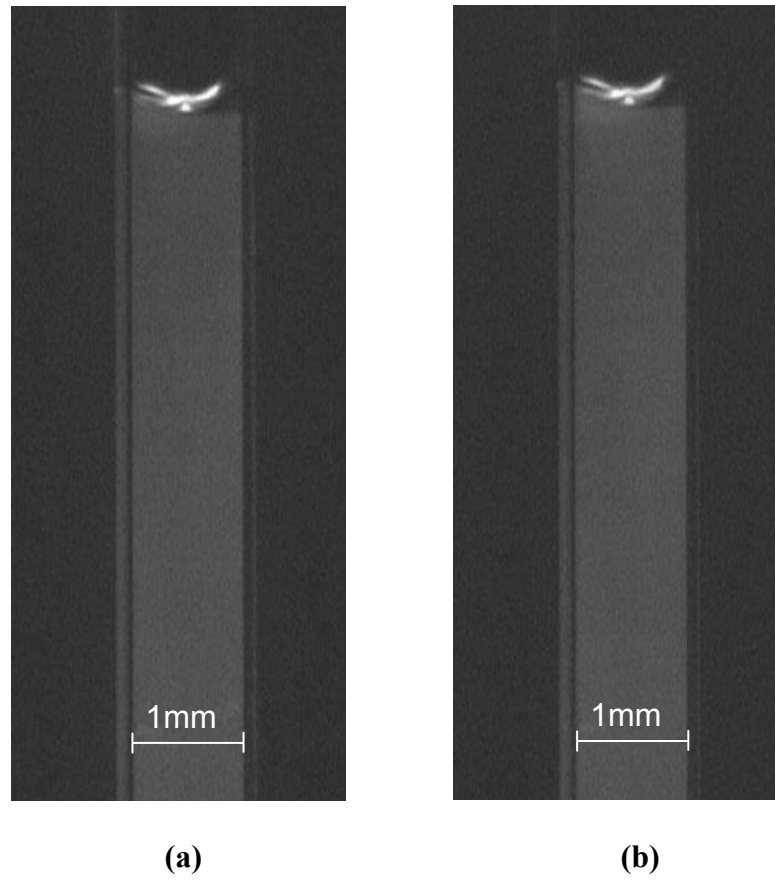


Fig . 4.12. Raw images of (a) Rh-B and (b) Rh-110 for thermal condition case 1.

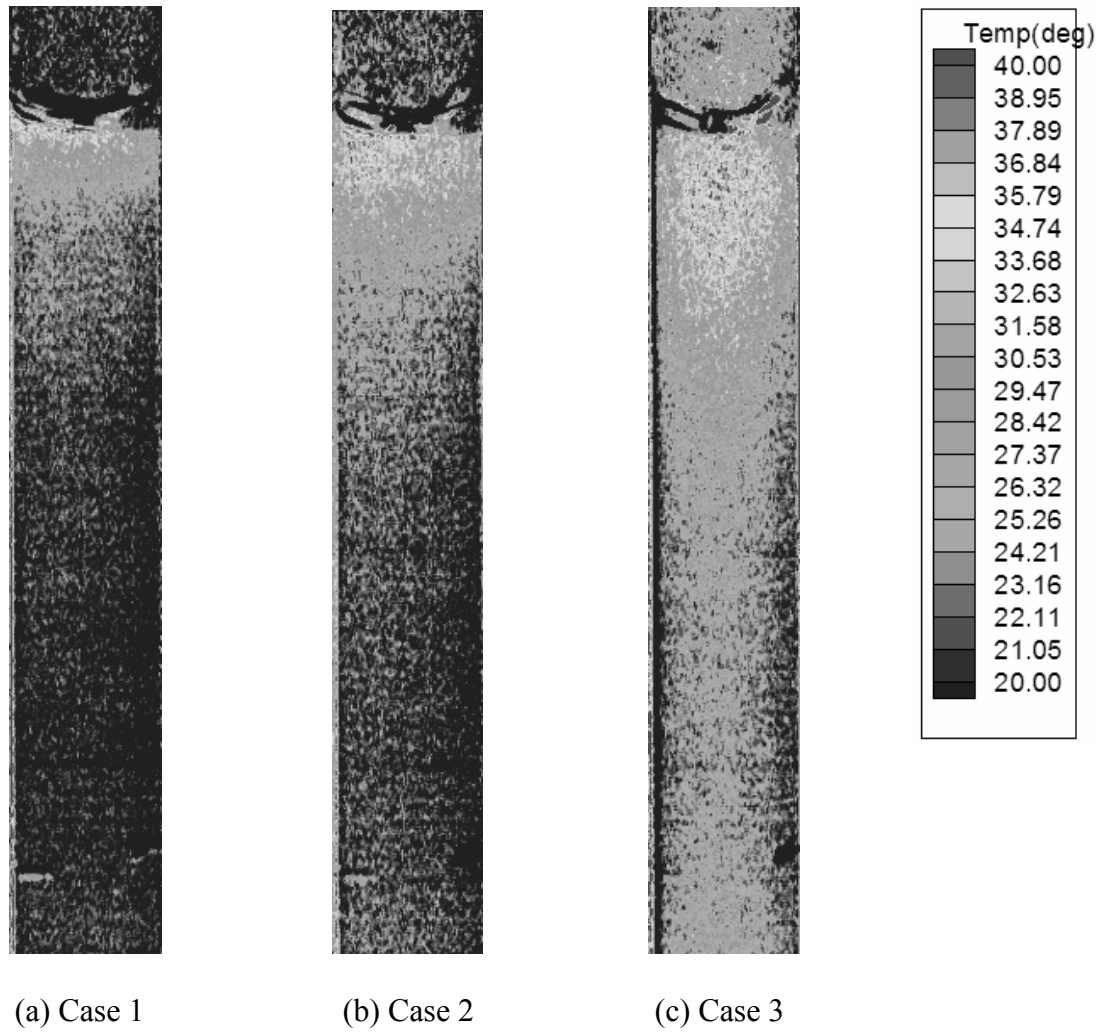


Fig. 4.13. Temperature profiles for different thermal conditions: (a) $Ra = 277.2$, (b) $Ra = 352.8$, (c) $Ra = 403.2$

meniscus region may have significant error. Thus, the temperature fields away from the meniscus without reabsorption problem will be concentrated and discussed. Figure 4.13 shows the temperature profiles developed from the calibration curve using intensity ratios measured in the experiment. Rayleigh numbers are calculated for three thermal conditions. Rayleigh number is defined as,

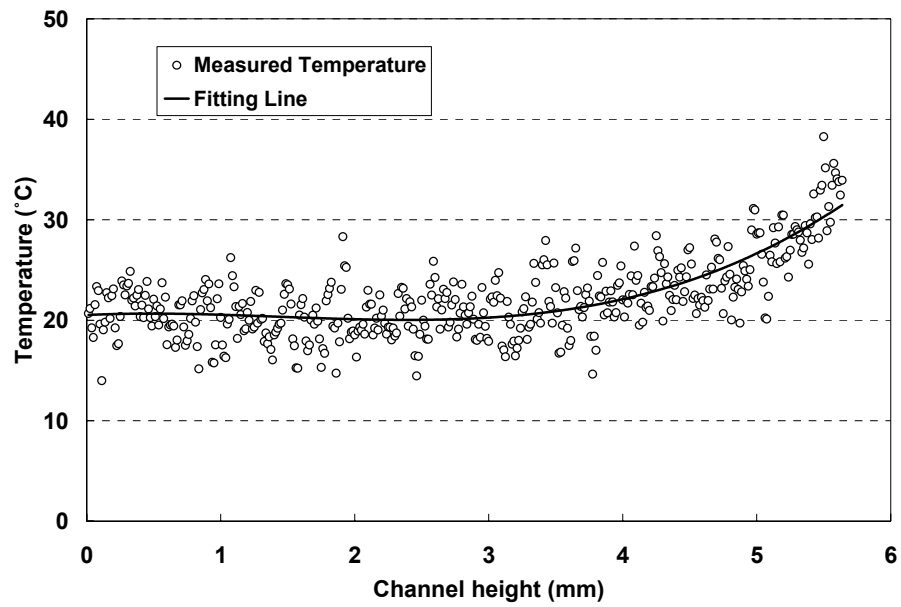
$$Ra = \frac{g\beta_t\Delta Td^3}{\nu\alpha_t} \quad (4.6)$$

where g is the gravitational acceleration, β_t is the thermal expansion coefficient, ΔT is the temperature differential, d is the characteristics length, ν is the kinematic viscosity, and α_t is the thermal diffusivity. Rayleigh number is the indicator to determine the onset of convective flow at the critical value. For the configuration with a fixed top surface, convection occurs when Ra is larger than 1700 and for the top surface free, the critical Ra is about 1100. As indicated in Fig. 4.13, Rayleigh numbers are less than 1100 for three thermal cases and thus there could be no convection inside the channel. However, liquid flow driven by thermocapillary stresses would be made in tiny area around the meniscus. As explained in analytical part, the thermocapillary stresses are induced due to the temperature gradient along the liquid-vapor interface of the heated meniscus.

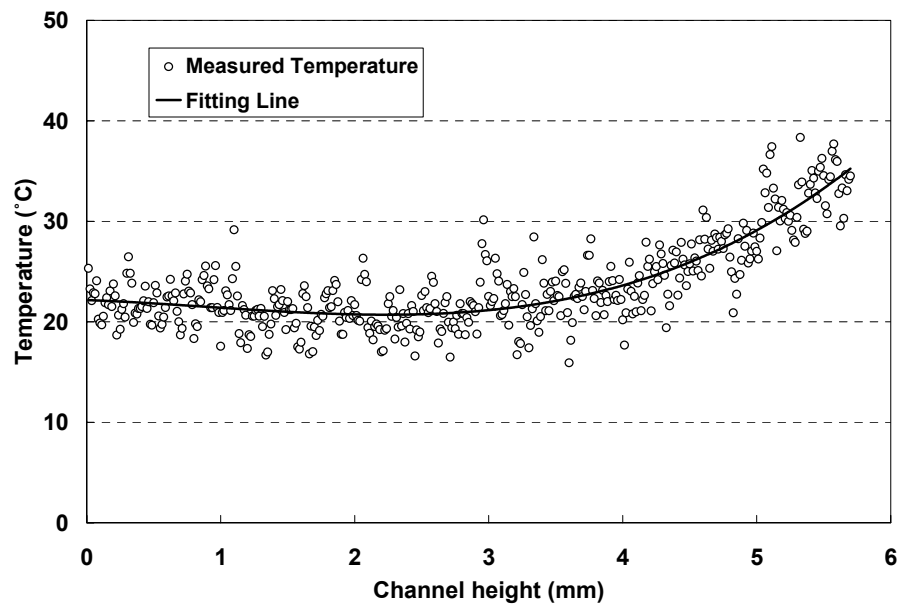
The temperature profiles in Fig. 4.13 clearly demonstrate that the high temperature region at top expands downward the low temperature region at bottom as the heater temperature increases. However, the temperature profiles near the meniscus region would be not correct. The region can be explained by the reabsorption due to the reflected light from the meniscus surface. There is total reflection of laser light from

meniscus surface at larger than critical incident angle. The fluorescent dyes are excited by original laser light and in addition they are excited by the total reflected light once more, which induce the reabsorption problem and then it induce the abnormal temperature measurement in the meniscus region. Such bias was also observed in the experiment of Lee (2003).

Figure 4.14 shows the temperature distribution measured along the channel centerline for three thermal conditions. The channel height indicates the distance from the bottom line of the channel in Fig. 4.13. Each circle represents the measure temperature at each pixel. The fitting line was calculated by a least square fitting through every point. The fitting line clearly demonstrates that the hotter region expand downward the lower temperature region as the heater temperature increases. Under such temperature conditions, there would be nearly no convective flow inside the channel and thus pure conduction alone will transfer the heat downward through the solution.

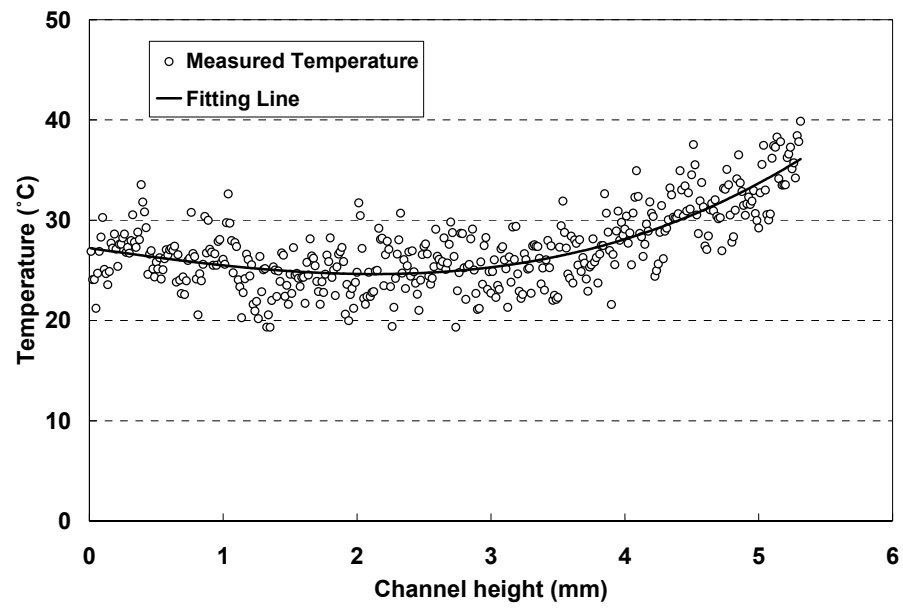


(a) Case 1



(b) Case 2

Fig. 4.14. Temperature distribution along centerline of the glass channel.



(c) Case 3

Fig. 4.14. (Continue)

CHAPTER V

SUMMARY AND CONCLUSIONS

5.1 Summary

The fluid flow and heat/mass transport phenomena within an evaporating extended meniscus, especially thin film region, were extensively studied based on the augmented Lapalce-Young equation, momentum equation, energy equation and mass conservation. The numerical model also incorporates the effect of thermocapillary stresses due to the surface tension gradient caused by the interfacial temperature gradient. Several specific effects such as slip boundary condition, polarity effect of working fluid and binary mixture evaporation were included to examine the heat and mass transport of the evaporating thin film. According to the scaling procedure, a 4th order, nonlinear, ordinary differential equation describing the non-dimensional film profile was developed for an evaporating extended meniscus and then the differential equation was solved by Gear's method. Once the shape was obtained numerically, the other properties such as liquid pressure, interfacial temperature and evaporative mass flux could be obtained by utilizing the information of the profile since all other thermo-physical properties are related to the meniscus shape in the related equations.

The thermocapillary effect was incorporated in the shear stress boundary condition of momentum equation to examine the effect under the non-isothermal interfacial thermal condition. The slip effect was also included in the wall boundary condition of momentum equation. The effect of binary mixture evaporation was

incorporated in the pressure gradient by considering the gradient in concentration of components. The polarity effect of water was included in disjoining pressure to examine the effect on the phase-change heat transfer by considering two different models of disjoining pressure for polar and non-polar liquids.

The temperature measurement with a microscale spatial resolution was carried out using ratiometric laser induced fluorescence (LIF) thermometry. Rhodamine-B was employed for temperature sensitive dye and Rhodamine-110 was non-temperature sensitive dye. The ratio of fluorescent intensity of Rh-B and Rh-110 provided a correlation between temperature and intensity ratio without any bias errors usually encountered in conventional LIF technique. The calibration curve was validated in thermally stratified fields established inside a glass cuvette with known thermal conditions and then the calibration curve was utilized in temperature mapping of thermal fields formed in capillary tube with 1 mm by 1 mm square cross sectional shape. The feasibility and potential use of ratiometric LIF technique for the microscale temperature measurement were discussed.

5.2 Conclusions

It is of critical importance to understand the microscale heat and mass transport phenomena occurring in the evaporating thin film. The insights obtained in the numerical solutions presented in this work could effectively be used in the design of the phase-change heat transport devices to achieve enhanced heat transport performance and effective cooling schemes for modern microelectronic devices.

From the numerical studies on the evaporating thin film, the fundamental conclusions are summarized as follows:

1. As a superheat increases, the thickness of the adsorbed film and the length of the transition film region decrease due to the combined effects of disjoining and capillary pressure to naturally re-supply the liquid into the evaporation region from the bulk meniscus region. At extreme case, the liquid flow cannot re-supply enough liquid to the evaporation region and then this leads to the dry-out or capillary limit of the capillary phase-change devices.
2. Thermocapillary stresses have detrimental effects on the thin film evaporation by degrading the wettability of working fluid. The thermocapillary stress is induced by the gradient in surface shear resulting from the interfacial temperature gradient. The effect influences the stability of thin film evaporation and becomes more severe with increasing superheat associated with heat flux applied.
3. The evaporating extended meniscus was more spread out due to the slip effect and binary mixture evaporation since there is less flow resistance associated with slip effect at the solid wall. As a result of less flow drag, the slip effect enhanced the heat transport effectiveness.
4. The binary mixture evaporation improved the wetting characteristics of working fluid by introducing distillation-driven capillary stresses, which counteract the detrimental effect of thermocapillary stresses.

5. The polarity effect of working fluid elongated the transition region; however, the polarity restrained liquid from evaporation by strong molecular interaction between liquid and solid molecules.

Ratiometric LIF technique showed its potential use for microscale temperature measurement and its feasibility to be applied to the measurement in the evaporating thin film in the future. The well-established calibration data shows the estimated uncertainty was ± 3.36 °C with a 95 % confidential level for interrogation window size of 12.5 μm by 12.5 μm . For thermally stratified field inside a glass channel with width of 10 mm at temperature differential of 11 °C, the temperature measurement error was 0.81 °C for a spatial resolution of 200 μm by 200 μm . In the temperature measurement of a glass channel with 1 mm by 1 mm square cross section, the temperature profiles clearly demonstrated that the hotter region spread downward by pure conduction under different thermal conditions. The fitting line established by means of a least square fitting using pixel by pixel temperatures measured showed a good trend of heat transfer downward through the liquid inside the channel.

5.3 Recommendations

For better understanding of microscale fluid flow and heat/mass transport phenomena, the followings are recommended in numerical part and experimental part:

1. Two-dimensional approach such as finite volume method (FVM) or finite element method (FEM) will be very useful to understand the thermo-physical

process of the evaporation process. Recently highlighted molecular dynamic (MD) simulations also could give a good approach to checking the validity of the traditional continuum assumptions.

2. In order to better understand the deprime mechanism of evaporation section resulting from thermocapillary effect at specific superheat condition, the vapor recoil stress influencing the movement of the liquid-vapor interface should be considered in mathematical model.
3. The vapor pressure variation should be considered to figure out the evaporation mechanism under more realistic condition, although the variation is so small relative to the change in liquid pressure.
4. In ratiometric LIF experiment, the intensity of fluorescence is very sensitive to the environment since convective heat transfer occurs at the interface of the specimen and air in laboratory. In order to avoid the uncertainty resulting from the interaction with environment, therefore, a chamber is required to ensure that.
5. In experiment CCD noise was observed, which was shown like a little brighter band movement on the computer monitor. This CCD noise makes unusual intensity variation on the captured image. Usually this noise came from the thermal problem in CCD. Cooled CCD would provide the solution to prevent such noise. The noise could be caused by the frame grabber. Therefore, it is strongly required to make sure the noise free image obtained since the LIF technique is extremely sensitive to external noise which is hard to be removed in spite of using the ratiometric technique.

6. Laser intensity changes for the time spend after laser turns on. As time flow, the intensity decreases by a little continuously. In order to ensure the captured image was obtained at constant laser intensity for Rh-B and Rh-110, constant time should be kept at capturing two images.
7. Temperature measurement in unsteady temperature field with microscale spatial resolution is strongly recommended. In order to do that, two CCD system and beam splitter are required.

REFERENCES

- Anderson, D.M., Davis, S.H., 1995. The spreading of volatile liquid droplets on heated surfaces. *Physics of Fluids* 7 (2), 248-265.
- Burelbach, J.P., Bankoff, S.G., Davis, S.H., 1988. Nonlinear stability of evaporating /condensing liquid films. *J. of Fluid Mechanics* 195, 463-494.
- Carey, V.P., 1992. *Liquid-Vapor Phase-Change Phenomena: An Introduction to the Thermophysics of Vaporization and Condensation Processes in Heat Transfer Equipment*. Hemisphere Publishing Corporation, Washington, DC.
- Carpi, A., 1998. Atomic Bonding in Introduction to Science in Society. The Natural Science Pages, <http://web.jjay.cuny.edu/~acarpi/NSC/index.htm>
- Chebaro, H.C., Hallinan, K.P., 1993. Boundary conditions for an evaporating thin film for isothermal interfacial conditions. *ASME J. of Heat Transfer* 115, 816-819.
- Chebaro, H.C., Hallinan, K.P., Kim, S.J., Chang, W.S., 1992. Evaporation from a porous wick heat pipe for isothermal interfacial conditions. Winter Annual Meeting of ASME HTD-Vol.221, Heat Pipes and Thermosyphons, pp. 23-28, Anaheim, CA.
- Choi, C.H., Westin, K.J.A., Breuer, K.S., 2002. To slip or not to slip water flows in hydrophilic and hydrophobic microchannels. Proceedings of IMECE 2002, ASME International Mechanical Engineering Congress & Exposition, IMECE 2002-33707, New Orleans, Louisiana.
- Churaev, N.V., 2003. Derjaguin's disjoining pressure in the colloid science and surface phenomena. *Advances in Colloid and Interface Science* 104, xv-xx.
- Cook, R., Tung, C.Y., Wayner, P.C., Jr., 1981. Use of scanning microphotometer to determine the evaporative heat transfer characteristics of the contact line region. *ASME J. of Heat Transfer* 103, 325-330.
- Coolen, M.C.J., Kieft, R.N., Mrindt, C.C., van Steenhoven, A.A., 1999. Application of 2-D LIF temperature measurements in water using a Nd-YAG laser. *Experiments in Fluids* 27, 420-426.
- Coppeta, J., Rogers, C., 1998. Dual emission laser induced fluorescence for direct planar scalar behavior measurements. *Experiments in Fluids* 25, 1-15.
- Cotter, T.P., 1984. Principles and prospects for micro heat pipes. Proceedings of the Fifth International Heat Pipe Conference, Part 1, pp. 328-335, Tsukuba, Japan.

- DasGupta, S., Schonberg, J.A., Wayner, P.C., Jr., 1993a. Investigation of an evaporating extended meniscus based on the augmented Young-Laplace equation. *ASME J. of Heat Transfer* 115, 201-208.
- DasGupta, S., Schonberg, J.A., Kim, I.Y., Wayner, P.C., Jr., 1993b. Use of the augmented Young-Laplace equation to model equilibrium and evaporating extended meniscus. *J. of Colloid and Interface Science* 157, 332-342.
- Derjaguin, B.V., Zorin, Z.M., 1957. Optical study of the adsorption and surface condensation of vapours in the vicinity of saturation on smooth surface. *Proceeding 2nd Int. Conf. Surface Activity*, Vol. 2, pp. 145-152, Butterwoods, London.
- Derjaguin, B.V., Nerpin, S.V., Churaev, N.V., 1965. Effect of film transfer upon evaporation of liquids from capillaries. *Bulletin RILEM* 29, 93-98.
- Dunn, P.D., Reay, D.A., 1994. *Heat Pipe*. 4th Edition, Pergamon, Oxford, UK.
- Faghri, A., 1995. *Heat Pipe Science and Technology*. Taylor & Francis, Washington, DC.
- Gad-el-Hak, M., 2001. Flow physics in MEMS. *Mecanique et Industries* 2, 313-341.
- Gear, C.W., 1971. *Numerical Initial Value Problems in Ordinary Differential Equations*. Prentice-Hall, Englewood Cliffs, New Jersey.
- Hallinan, K.P., 2003. Personal communication, Department of Mechanical and Aerospace Engineering, University of Dayton.
- Hallinan, K.P., Chebaro, H.C., Kim, S.J., Chang, W.S., 1994. Evaporation from an extended meniscus for nonisothermal interfacial conditions. *J. of Thermophysics and Heat Transfer* 8 (4), 709-716.
- Haugland, R.P., 2002. *Handbook of Fluorescent Probes and Research Products*. Web Edition, Molecular Probes, Inc., <http://www.probes.com/handbook/>
- He, Q., Hallinan, K.P., 1994. Thermocapillary effects on the evaporating extended meniscus. *ASME International Mechanical Engineering Congress and Exposition, Heat Transfer in Microgravity Systems*, HTD-Vol. 290, pp. 71-82, Chicago, Illinois.
- Herman, B., 1998, *Florescence Microscopy*. Second Edition, Springer, New York.
- Hidrovo, C.H., Hart, D.P., 2002. 2D thickness and temperature mapping of fluids by means of a two-dye laser induced fluorescence ratiometric scheme. *J. of Flow Visualization & Image Processing* 9, 171-191.

- Holm, F.W., Goplen, S.P., 1979. Heat transfer in the meniscus thin film transition region. ASME J. of Heat Transfer 101, 543-547.
- Israelachvili, J., 1992. Intermolecular & Surface Forces. Academic Press Limited, San Diego, CA.
- Kern, J., Stephan, P., 2003a. Theoretical model for nucleate boiling heat and mass transfer of binary mixtures. ASME J. of Heat Transfer 125, 1106-1115.
- Kern, J., Stephan, P., 2003b. Investigation of decisive mixture effects in nucleate boiling of binary mixtures using a theoretical model. ASME J. of Heat Transfer 125, 1116-1122.
- Kim, H.J., 2001. Temperature and Velocity Field Mapping for Micro-Scale Heat and Mass Transport Phenomena, Ph.D. Dissertation, Texas A&M University.
- Kim, H.J., Kihm, K.D., Allen, J.S., 2003. Examination of ratiometric laser induced fluorescence thermometry for microscale spatial measurement resolution. Int. J. of Heat and Mass Transfer 46, 3967-3974.
- Ku, G., 1993. Overview of capillary pumped loop technology. 29th National Heat Transfer Conference, ASME HTD-Vol. 236, pp. 1-17, Atlanta, Georgia.
- Lee, H.J., 2003, Application of a ratiometric laser induced fluorescence (LIF) thermometry for micro-scale temperature measurement for natural convection flows, Master Thesis, Texas A&M University.
- Logan, R.H., 1997, General Chemistry, <http://members.aol.com/logan20/alkanes.html>
- Ma, H.B., Peterson, G.P., Lu, X.J., 1994. The influence of vapor-liquid interactions on the liquid pressure drop in triangular microgrooves. Int. J. Heat and Mass Transfer 37, 2211-2219.
- Ma, H.B., Peterson, G.P., Pratt, D.M., 1998. Disjoining pressure effect on the wetting characteristics in a capillary tube. Microscale Thermophysical Engineering 2, 283-297.
- Mirzamoghadam, A., Catton, I., 1988. A physical model of the evaporating meniscus. ASME J. of Heat Transfer 110, 201-207.
- Mitrovic, J., 1998. The flow and heat transfer in the wedge-shaped liquid film formed during the growth of a vapour bubble. Int. J. Heat and Mass Transfer 41, 1771-1785.

- Moosman, S., Homsy, G.M., 1980. Evaporating meniscus of wetting fluids. *J. of Colloid Interface Science* 73 (1), 212-223.
- Navier, C.L.M.H., 1823. *Memoirs de l'Academie Royale des Sciences de l'Institut de France* 1, 414-416.
- Neogi, P., Miller, C.A., 1982. Spreading kinetics of a drop on a smooth solid surface. *J. of Colloid Interface Science* 86 (2), 525-538.
- NIST Chemistry WebBook, NIST Standard Reference Database Number 69, March, 2003 Release, <http://webbook.nist.gov/chemistry/>.
- Park, K., Noh, K.J., Lee, K.S., 2003. Transport phenomena in the thin-film region of a micro-channel. *Int. J. Heat and Mass Transfer* 46, 2381-2388.
- Parks, C.J., Wayner, P.C., Jr., 1985. Fluid flow in an evaporating meniscus of a binary mixture in the contact line region: constant vapor pressure boundary condition. *AICHE 77th Annual Meeting*, pp. 1-21, Chicago, Illinois.
- Parks, C.J., Wayner, P.C., Jr., 1987a. Surface shear near the contact line of a binary evaporating curved thin film. *AICHE Journal* 33 (1), 1-10.
- Parks, C.J., Wayner, P.C., Jr., 1987b. A model for the transport phenomena associated with a two-component meniscus evaporation into a multicomponent vapor. *AICHE Symposium Series* 257 (83), 122-127.
- Peles, Y.P., Haber, S., 2000. A steady state, one dimensional, model for boiling two phase flow in triangular micro-channel. *Int. J. of Multiphase Flow* 26, 1095-1115.
- Peterson, G.P., 1992. Overview of micro heat pipe research and development. *Applied Mechanics Reviews* 45 (5), 175-189.
- Peterson, G.P., Ma, H.B., 1999. Temperature response of heat transport in a micro heat pipe. *ASME J. of Heat Transfer* 121, 438-445.
- Potash, M., Jr., Wayner, P.C., Jr., 1972. Evaporative from a two-dimensional extended meniscus. *Int. J. Heat and Mass Transfer* 15, 1851-1863.
- Pratt, D.M., Hallinan, K.P., 1995. An investigation of thermocapillary effects on a heated capillary re-supplied meniscus for low Bond numbers. *Proceedings of the Third Caribbean Congress on Fluid Dynamics* 1, 1-11.
- Pratt, D.M., Hallinan, K.P., 1997. Thermocapillary effects on the wetting characteristics of a heated curved meniscus. *J. of Thermophysics and Heat Transfer* 11 (4), 519-525.

- Pratt, D.M., Kihm, K.D., 2003. Binary fluid mixture and thermocapillary effects on the wetting characteristics of a heated curved meniscus. *ASME J. of Heat Transfer* 125, 867-874.
- Pratt, D.M., Brown, J.R., Hallinan, K.P., 1998. Thermocapillary effects on the stability of a heated curved meniscus. *ASME J. of Heat Transfer* 120, 220-226.
- Pratt, D.M., Hallinan, K.P., Chang, W.S., 1997. Thermocapillary effects on the heat transfer effectiveness of a heated curved meniscus. National Heat Transfer Conference, ASME HTD-Vol. 349, pp. 97-104, Baltimore, Maryland.
- Qu, W., Ma, T., 2002. Effects of the polarity of working fluids on vapor-liquid flow and heat transfer characteristics in a capillary. *Microscale Thermophysical Engineering* 6, 175-190.
- Reid, R.C., Prausnitz, J.M., Sherwood, T.K., 1977. The properties of gases and liquid. 3rd Ed., McGraw-Hill, New York.
- Renk, F.J., Wayner, P.C., Jr., 1979a. An evaporating ethanol meniscus, Part I: Experimental studies. *ASME J. of Heat Transfer* 101, 55-58.
- Renk, F.J., Wayner, P.C., Jr., 1979b. An evaporating ethanol meniscus, Part II: Analytical studies. *ASME J. of Heat Transfer* 101, 59-62.
- Reyes, R., Wayner, P.C., Jr., 1997. Interfacial models for the critical heat flux superheat of a binary mixture. 32nd National Heat Transfer Conference, ASME HTD-Vol. 342, pp. 187-194, Baltimore, Maryland.
- Ruckenstein, E., Dunn, C.S., 1977. Slip velocity during wetting of solids. *J. of Colloid Interface Science* 59 (1), 135-138.
- Ruckenstein, E., Rajora, P., 1983. On the no-slip boundary condition of hydrodynamics. *J. of Colloid Interface Science* 96 (2), 488-491.
- Sakakibara, J., Adrian, R.J., 1999. Whole field measurement of temperature in water using two-color laser induced fluorescence. *Experiments in Fluids* 26, 7-15.
- Schonberg, J.A., Wayner, P.C., Jr., 1992. Analytical solution for the integral contact line evaporative heat sink. *J. of Thermophysics and Heat Transfer* 6 (1), 128-134.
- Schrage, R.W., 1953. A theoretical study of interphase mass transfer. Columbia University Press, New York.
- Scriven, L.E., Sternling, C.V., 1960. The Marangoni effects. *Nature* 187, 186-188.

- Son, G., Ramanujapu, N., Dhir, V.K., 2002. Numerical simulation of bubble merger process on a single nucleation site during pool nucleate boiling. *ASME J. of Heat Transfer* 124, 51-62.
- Stephan, P.C., Busse, C.A., 1992. Analysis of the heat transfer coefficient of grooved heat pipe evaporator walls. *Int. J. Heat and Mass Transfer* 35, 383-391.
- Stephan, R., Hammer, J., 1994. A new model for nucleate boiling heat transfer. *Warme- und Stoffubertragung* 30, 119-125.
- Swanson, L.W., Herdt, G.C., 1992. Model of the evaporating meniscus in a capillary tube. *ASME J. of Heat Transfer* 114, 434-441.
- Thompson, P.A., Troian, S.M., 1997. A general boundary condition for liquid flow at solid surfaces. *Nature* 389, 360-362.
- Thomson, J., 1855. On certain curious motions observable at the surfaces of wine and other alcoholic liquors. *Philosophical Magazine* 10, Series 4, 330-333.
- Tien, C.L., 1970. Two-component heat pipe. *Thermophysics: Applications to Thermal Design of Spacecraft* ed. J.T.Bevans, Academic Press, New York.
- Tien, C.L., 1975. Fluid mechanics of heat pipes. *Annual Reviews of Fluid Mechanics* 7, 167-185.
- Tretheway, D.C., Meinhart, C.D., 2002. Apparent fluid slip at hydrophobic microchannel walls. *Physics of Fluids* 14 (3), L9-L12.
- Tso, C.P., Mahilikar, S.P., 2000. Combined evaporating meniscus-driven convection and radiation in annular microchannels for electronics cooling. *Int. J. of Heat and Mass Transfer* 43, 1007-1023.
- Tung, C.Y., Muralidhar, T., Wayner, P.C., Jr., 1982. Experimental study of evaporation in the contact line region of a mixture of decane and 2% tetradecane. *Proceeding of the 7th International Heat Transfer Conference, Vol. 4, pp. 101-106, Munich.*
- Tung, C.Y., Wayner, P.C., Jr., 1984. Effect of surface shear on fluid flow in an evaporating meniscus of a mixture of alkanes. *5th Int. Heat Pipe Conference, pp. 201-207, Tsukuba, Japan.*
- Volintine, B.G., Wayner, P.C., Jr., 1986. Fluid flow and evaporation in an ultra-thin film of a binary mixture. *AIChE Symposium Series* 82 (252), 157-166.

- Wayner, P.C., Jr., 1991. The effect of interfacial mass transport on flow in thin liquid films. *Colloids and Surfaces* 52, 71-84.
- Wayner, P.C., Jr., 1999. Intermolecular forces in phase-change heat transfer: 1998 Kern Award Review. *AIChE Journal* 45 (10), 2055-2068.
- Wayner, P.C., Jr., Schonberg, J., 1990. Heat transfer and fluid flow in an evaporating extended meniscus. 9th International Heat Transfer Conference, pp. 229-234, Israel.
- Wayner, P.C., Jr., Kao, Y.K., LaCroix, L.V., 1976. The interline heat transfer coefficient of an evaporating wetting film. *Int. J. Heat and Mass Transfer* 19, 487-492.
- Wayner, P.C., Jr., Tung, C.Y., Tirumda, M., Yang, J.H., 1985. Experimental study of evaporation in the contact line region of a thin film of hexane. *ASME J. of Heat Transfer* 107, 182-189.
- Welter, D., 1991. The effect of evaporation on the dynamic capillary pressure in heat pipes. Master Thesis, University of Dayton, Ohio.

VITA

Sang-Kwon Wee

Gukduk APT #1801, Hakjang-Dong, Sangsang-Ku, Pusan, Korea

E-mail: skwee@hanmail.net

Personal Data

Date of Birth: March 7, 1970

Spouse: Kum Sook Jeong

Children: Woo-Ju Wee and Michelle Youn-Ju Wee

Parents: Bokwoong Wee and Soonduk Lee

Education

Ph.D. Mechanical Engineering, Texas A&M University, May 2004

M.S. Aerospace Engineering, Korea Advanced Institute of Science and Technology, Korea, February 1995

B.S. Aerospace Engineering, Pusan National University, Korea, February 1993

Professional Experience

01/2001-01/2004 Research/Teaching Assistant in the Department of Mechanical Engineering, Texas A&M University

02/1995-05/2000 Research Engineer in Engine Research Center, SAMSUNG Aerospace Industries, Korea